Chapter 4: Evidence of tidal modulation at seafloor hydrothermal systems

4.1 Introduction

Over the last twenty years, many attempts have been made to acquire time-series measurements at seafloor hydrothermal systems. The aims and techniques of these studies are diverse, as are the locations at which the data were collected. There is no reason to suppose - *a priori* - that the same physical process causes the tidal modulation in all of these data. Nonetheless, in order to obtain an overview of tidal modulation in hydrothermal systems, it is useful to collate all of the published seafloor time-series which have been examined with tidal effects in mind. Consequently this chapter is devoted to an examination of the current evidence concerning tidal modulation of seafloor hydrothermal systems

The data which have been collected on the seafloor cover a wide range of hydrothermal sites. Accordingly, the time-series discussed in this chapter are classified into sections according to seafloor location. There are several further ways in which the datasets can be distinguished. Measurements have been made (1) above the seafloor, (2) on the seafloor and (3) below the seafloor. Furthermore, the settings for the measurements cover (1) high temperature vents (350°C - 400°C), (2) areas of warm diffuse flow (typically <50°C), and (3) cooler regions on the ridge flanks. At the most fundamental level, the various time-series can be classified according to the physical quantity which they record. Broadly, the four physical quantities which have been measured with tidal influence in mind are – (1) pressure, (2) temperature, (3) effluent velocity, and (4) fluid composition.

Pressure measurements at the seafloor have been made by Sato *et al.* (1995) and Fujioka *et al.* (1997) who used a hydrophone to measure pressure pulses. The pressure pulses are taken to be indicators of hydrothermal activity and their frequency of occurrence is correlated with the ocean tides. The other pressure data discussed below were made in sealed boreholes (Davis & Becker, 1994; Davis *et al.,* 1995; Davis & Becker, 1999) and are a measure of the fluid pressure in igneous rock lying below a layer of comparatively impermeable sediment. Although it is desirable to have direct time-series measurements of the ambient pressure on the seafloor, this information is rarely collected at hydrothermal sites. Consequently the

seafloor pressure in the open oceans is often estimated by an ocean tide model such as the CSR code (Schrama & Ray, 1994).

The measurements of temperature discussed below were obtained in a wide variety of settings. Firstly, below the seafloor, time-series of temperature have been collected at depths of up to 400 m within boreholes (Davis & Becker, 1994; Davis *et al.,* 1995; Davis & Becker, 1999). Temperatures have also been measured within 1 m of the seafloor using geothermal probes (Kinoshita *et al.,* 1996, 1998). Secondly, on the seafloor, there have been measurements of the temperature of diffuse effluent (Schultz *et al.,* 1992; Schultz *et al.,* 1996), the temperature of mussel beds around hydrothermal vents (Johnson *et al.,* 1994; Chevaldonné *et al.,* 1991), and the temperature of the hydrothermal vents themselves (Fornari *et al.,* 1998). Thirdly, above the seafloor, time-series of temperature have been collected in the water column at hydrothermal vent sites. The location of these measurements ranges from 3 cm above diffuse flow (Little *et al.,* 1988, 1989), to over 100 m above sites of focussed discharge (Wetzler *et al.,* 1998; Rudnicki *et al.,* 1994). Measurements have also been made at a lateral distance of a few metres from black smokers, at a height of 2 m above the seafloor (Fujioka *et al.,* 1997).

The measurements of the velocity of hydrothermal effluent discussed below were made using the Medusa hydrothermal effluent monitoring system (Schultz *et al.,* 1992; Schultz *et al.,* 1996) on areas of diffuse hydrothermal flow (<100°C).

Time-series measurements of the composition of hydrothermal effluent can take several forms. Firstly, the optical transmissivity of the water can be measured in order to estimate the turbidity or quantity of suspended particulate matter (Johnson & Tunnicliffe, 1985; Fujioka *et al.,* 1997). Secondly, chemical samples of effluent fluid can be collected at successive times for later analysis in the laboratory (Kadko, 1994; Cooper, 1999; Cooper *et al.,* 2000).

The aim of this chapter is to quantify the tidal signals observed in datasets obtained at seafloor hydrothermal systems. The observable signals (pressure, temperature, effluent velocity and effluent composition) are considered to be the output signals from a physical process whose inputs are the solid tide, the ocean tide and tidal streams. Where sufficient data are available the analysis of each output signal follows a strict sequence. Firstly, the

time-series is plotted alongside an estimate of the local ocean tide. For clean data, the tidal modulation of the output signal is sometimes immediately apparent in the time-domain. Secondly, a non-parametric estimate of the power spectrum of the time-series is made using the MWPS code. This procedure contains a statistical test for the presence of significant line components in the spectrum. Evidence for tidal modulation of the time-series is provided by the presence of line components at the known tidal frequencies (Table 2.1, Figure 2.7). For a tidally modulated time-series, the strongest line component is expected to occur at the *M2* frequency (1.932 cpd). Thirdly, if the time-series displays evidence of tidal modulation, a parametric estimate of the tidal component of the time-series can be made. The HYBRID code (Section 3.3.4) is used to estimate the Admiralty Method harmonic constants which describe the tidal component of the signal.

One of the objectives of this chapter is to establish which of the input signals (ocean tide, solid tide, tidal streams) causes the tidal modulation observed in the output signals (pressure, temperature, effluent velocity, composition). To this end, the estimated Admiralty Method harmonic constants for the output signal are compared with those for the solid and ocean tides. It should be noted that the Admiralty Method harmonic constants for the ocean and solid tides are obtained with negligible error. Synthetic time-series for the ocean tide can be generated by the CSR code, while time-series for the tidal potential are generated by the ETGTAB code. The solid tide is simply a scaled version of the tidal potential, by equation (2.18). The Admiralty Method harmonic constants for the input signals are then obtained by analysing the synthetic time-series with the HYBRID code. In contrast, the harmonic constants for the output time-series are known to much lower precision because the time-series are contaminated by noise.

In summary, this chapter contains a detailed and critical study of all reported tidally modulated time-series observed at seafloor hydrothermal systems. The separate data sets are compared with the tidal potential and the ocean tide in an attempt to uncover a coherent picture of tidal modulation in hydrothermal systems. It should be stressed that not all hydrothermal time-series display evidence of tidal modulation (Fornari *et al.,* 1998). However, there is no doubt that tidal modulation of hydrothermal systems does occur in many cases, and there is considerable interest in discovering the mechanism (or mechanisms) which causes this modulation.

4.2 Juan de Fuca Ridge

Several time-series measurements have been made at hydrothermal sites on the Juan de Fuca Ridge off the northwestern coast of the USA where the ocean tides have a significant diurnal component. The Admiralty Method harmonic constants at the Endeavour Segment (47.8°N, 129.0°W) are typical; those for the tidal potential and ocean tide are listed in Table 4.1 and graphed in Figure 4.1.

Endeavour	H_1 (*M2A*)	g_1 (*M2A*)	H_2 (*S2A*)	g_2 (*S2A*)	H_3 (*K1A*)	g_3 (*K1A*)	H_4 (*O1A*)	g_4 (*O1A*)
potential ($m^2.s^{-2}$)	1.28	257°	0.60	257°	1.60	129°	1.13	129°
ocean (m)	0.89	240°	0.26	272°	0.42	243°	0.26	226°

Endeavour	$(H_1+H_2)/(H_3+H_4)$	H_1/H_2	g_2-g_1	H_3/H_4	g_4-g_3
potential ($m^2.s^{-2}$)	0.687	2.14	< 1°	1.41	< 1°
ocean (m)	1.69	3.42	32°	1.62	-17°

Table 4.1: The Admiralty Method harmonic constants for the tidal potential and the ocean tide at the Endeavour Segment (47.8°N, 129.0°W). Estimates made using the HYBRID code.

4.2.1 Endeavour Segment (1)

The first seafloor time-series from a seafloor hydrothermal system to exhibit tidal modulation were obtained at a low temperature (56°C) vent on the Endeavour Segment (47.8°N, 129.0°W) of the Juan de Fuca Ridge (Johnson & Tunnicliffe, 1985). A camera was placed next to the vent and still photographs were obtained at a sampling interval of Δt = 42 min over a period $N\Delta t$ = 5 days. The photographs were analysed to produce estimated time-series of lateral water motions and the suspended particulate load or turbidity. The time-series of seafloor current was inferred from the deflection of vestimentiferan worms in the photographs. Johnson & Tunnicliffe (1985) report that this current is semi-diurnal and 'nearly in phase' with the semi-diurnal component of the ocean tide. Their spectral analysis of this inferred current data reveals a large semi-diurnal peak at about 1.90 cpd, but no evidence of a diurnal peak. Two further time-series - of suspended particulate load - were estimated by measuring the transmittance of light through the photographic slides. These two turbidity time-series - labelled *A* and *B* - were obtained from different regions of the photographs. Johnson & Tunnicliffe's (1985) spectral analysis of the first turbidity time-series (*A*) suggests that it was predominantly diurnal. Consequently, they infer a spectral

contrast between the *diurnal* variations in turbidity and the *semi-diurnal* variations in current, concluding that there is no causal link between turbidity and seafloor current.

It is instructive to re-examine this conclusion in the light of the theory discussed previously (Chapters 2 and 3). The first step is to consider the nature of the ocean tide at the vent site. The Admiralty Method harmonic constants for this site are given in Table 4.1, and graphed in Figure 4.1.

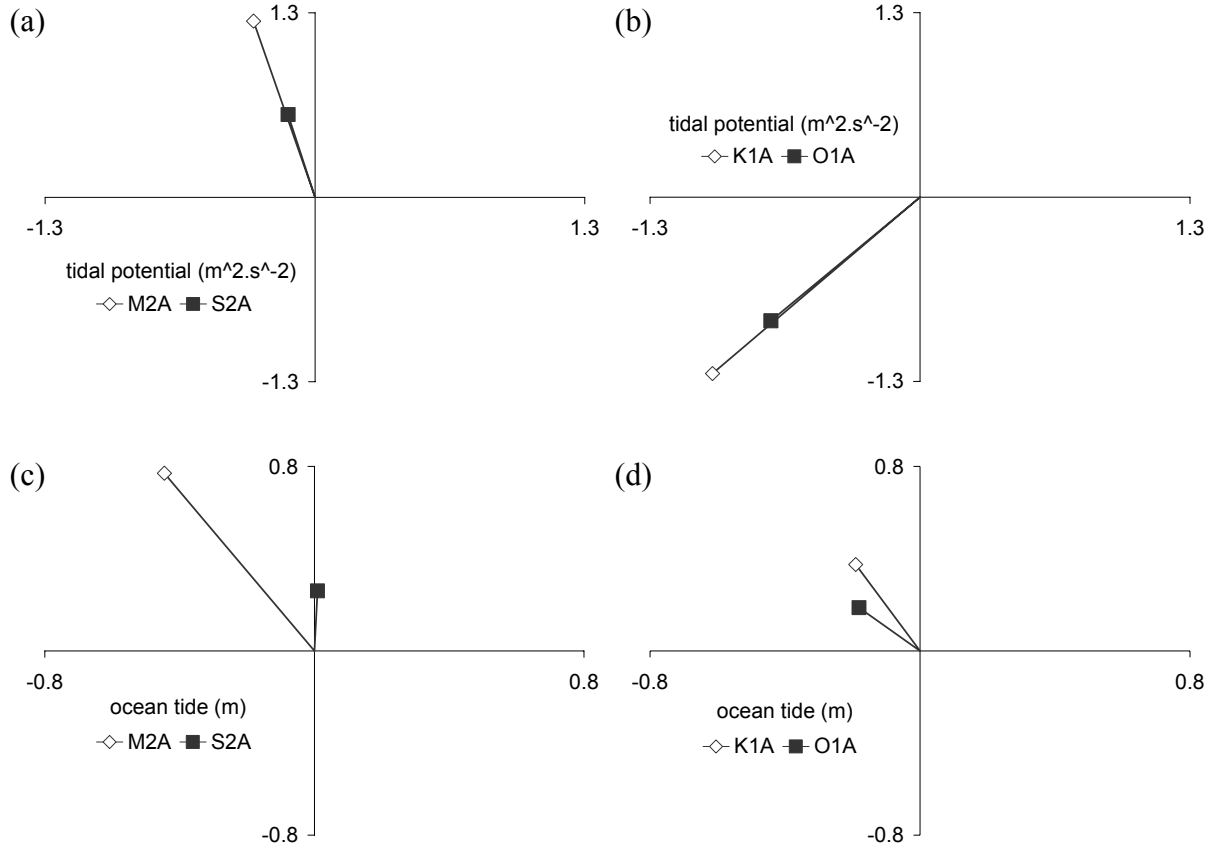

Figure 4.1: The (complex) Admiralty Method harmonic constants of the tidal potential and ocean tide at the Endeavour Segment (47.8°N, 129.0°W) extracted using the HYBRID code.

The harmonic constants show that the ocean tide at the Endeavour Segment has a significant diurnal component. The next step is to consider the nature of the tide over the observation period (from 1984/9/1 to 1984/9/6). Figure 4.2b shows that the lunar declination was relatively large at this time, and so the tide would have been *particularly* diurnal in character. This is confirmed in the time-domain view of the ocean tide at the time the observations were made (Figure 4.2a).

The two particulate load signals (*A*, *B*) are reproduced in Figure 4.2a together with a prediction of the ocean tide. Johnson and Tunnicliffe (1985) do not publish a prediction of the ocean tide for the observation period, but claim that the 'turbidity maxima are in phase

with the relevant component of the ocean surface elevation'. It is hard to discern strong evidence of this claim in Figure 4.2a.

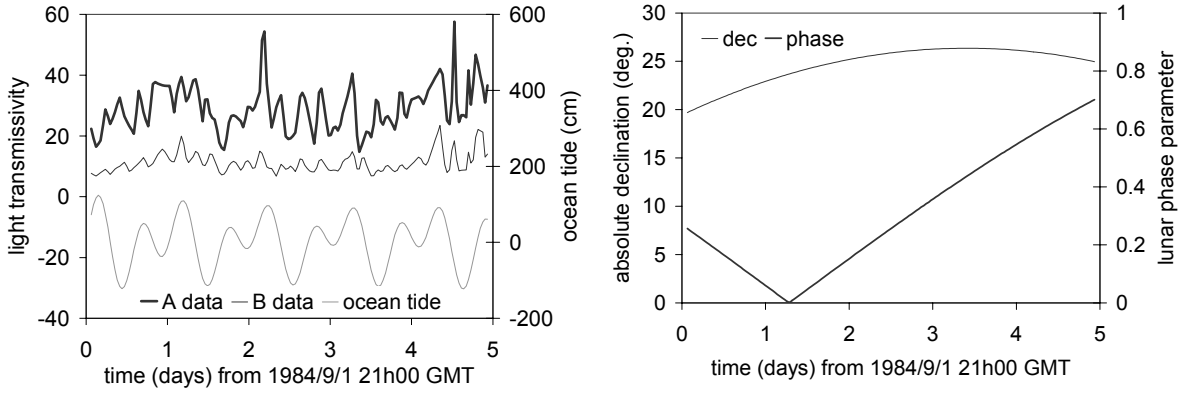

Figure 4.2: (a) Light transmissivity data (*A*, *B*) collected at the Endeavour Segment (47.8°N, 129.0°W) by Johnson & Tunnicliffe (1985). The local ocean tide is shown for comparison. (b) The lunar phase parameter, and absolute lunar declination for the same period, calculated using the CSR code.

A power spectrum estimate for the first turbidity time-series (*A*) is given by Johnson & Tunnicliffe (1985) but there is no discussion of the method by which it was obtained. The power spectra shown in Figure 4.3 were obtained from the turbidity time-series using two different methods and illustrate how the choice of spectral estimator influences the estimated spectrum (Section 3.2). The upper spectrum in Figure 4.3 is an unwindowed periodogram of the data following subtraction of the mean (Equation 3.1). The lower spectrum in Figure 4.3 was obtained using the MWPS code with a time-bandwidth product of 1 and 2 eigenspectra. An autoregressive pre-whitening filter of length 36 points (25.2 hours) was applied, and lines significant above the 95% level were removed. A significant line was found for the frequency bin at 1.948 ± 0.130 cpd. This frequency range encompasses the *M2* tidal component at 1.932 cpd. No significant lines were found in the diurnal band.

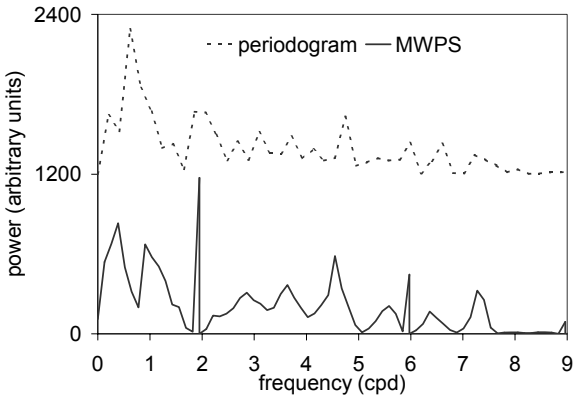

Figure 4.3: Power spectra for the turbidity time-series (*A*) (Johnson & Tunnicliffe, 1985) obtained using an unwindowed periodogram, and the MWPS code. For clarity, the periodogram estimate is offset by 1200 units on the vertical axis.

Figure 4.3 shows that the choice of spectral estimator has a profound effect on the estimated spectrum. The unwindowed periodogram estimate appears to have a greater concentration of power in the diurnal frequency band in agreement with the conclusions of Johnson & Tunnicliffe (1985). In constrast, the MWPS estimate has a statistically significant line component in the semi-diurnal band, but no significant line components in the diurnal band. The assertion that the turbidity time-series is predominantly diurnal can therefore be challenged. Figure 4.2a shows that the turbidity time-series (*A*) exhibits strong semi-diurnal oscillations in the time-domain, while the high lunar declination (Figure 4.2b) suggests that diurnal signals were at their strongest during the observation period. It is therefore likely that the time-series would appear even more strongly semi-diurnal at times of smaller lunar declination.

In summary, a re-examination of the data using the multiple window method casts doubt on the assertion that the turbidity signal is predominantly diurnal (Johnson & Tunnicliffe, 1985), and the subsequent conclusion that the turbidity and lateral currents are unconnected. It may simply be that the observed changes in turbidity are due to lateral current motions.

4.2.2 Endeavour Segment (2)

Time-series measurements of effluent temperature and velocity were obtained on the Endeavour Segment (47.95°N, 129.10°W) between 1988/7/15 and 1988/9/2 by Schultz *et al.* (1992). The measurements were made on an area of warm (7°C to 13°C) diffuse flow, where

the vertical effluent velocities ranged from 0.07 to 0.15 $m.s^{-1}$. Schultz *et al.* (1992) used a robust section-averaging method (Chave *et al.,* 1987) to estimate power spectra for the temperature and velocity signals. The spectra reveal a significant semi-diurnal peak for the temperature time-series. In contrast, the power spectrum of the velocity time-series appears 'white' with no obvious spectral peaks. It is suggested here that the choice of a section-averaged periodogram as the non-parametric spectral estimator (Section 3.2.1.6) may have a significant bearing on the spectra obtained. The data were collected at a sampling interval Δt=5 min, and a total of N=12,107 data points were used in the spectral analysis. Thus, the total length of the analysed time-series is about 42 days. However, in order to use a section-averaging approach, Schultz *et al.* (1992) were forced to divide the time-series into shorter subsections. They decomposed the series into five overlapping sections of 3,766 points, each of which spans a time interval of about 13 days. The disadvantage of this approach is that these short data subsections lead to decreased resolution in the frequency domain (Section 3.2).

It is therefore suggested that a higher resolution estimate of the power spectra would be obtained by applying the MWPS method of Section 3.2.2 to the data of Schultz *et al.* (1992).

4.2.3 Middle Valley

The boreholes of the Ocean Drilling Program (ODP) provide a number of tidally modulated time-series at seafloor hydrothermal systems (Davis & Becker, 1999). These boreholes have a diameter of 30 cm and are typically drilled to extend several hundred metres below the seafloor. The boreholes considered here are drilled in sedimented ridge-crest and ridge-flank environments. Consequently, the upper sections of the boreholes (corresponding to the sediment layer) are lined with cement to prevent hydraulic communication between the borehole and the sediment. The lower sections of the boreholes (corresponding to the igneous basement layer) are left open. Vertical arrays of thermistors are lowered into the boreholes to measure the temperature at selected depths, and a pressure sensor is placed near the top of each borehole. The tops of the boreholes are sealed to prevent hydraulic communication with the ocean, and time-series of pressure and temperature are collected. For each borehole, the pressure time-series is a measure of the pressure in the basement rock, since the cement lining isolates the borehole from the ocean and the sediment layer. Davis & Becker (1999) note that it can take more than a year for the pressure and temperature in a borehole to reach steady state. However, in addition to such long period trends in the time-series, there are also clear tidal signals.

Time-series of pressure and temperature were collected at ODP holes 857D and 858G (48.45°N, 128.72°W) in the Middle Valley of the Juan de Fuca ridge (Davis & Becker, 1994). Three weeks of data were collected at 857D in September 1991. No tidal modulation of temperature was observed, but the pressure variations were seen to be in phase with the local ocean tide and attenuated by a factor of 0.15. Davis & Becker (1994) explain this pressure data by appealing to the theory of poroelasticity, which is discussed in detail in Chapter 6. Hole 858G yielded 10 months of data beginning at September 1991. Again, there was a clear tidal modulation of the pressure signal, which was observed to be in phase with the local ocean tide. However, in this case, the pressure signal was attenuated by a factor which varied between 0.18 and 0.70 over the observation interval. All of the thermistor time-series displayed evidence of tidal modulation with a typical magnitude of 1°C. For all thermistors (i.e. all depths within the borehole) except one, the lowest temperatures occurred when the seafloor pressure was high. In contrast, the 'anomalous' thermistor recorded high temperatures when the seafloor pressure was high. In other words, for all thermistors except one the subseafloor temperature lags the ocean tide by 180°. One of the explanations proposed by Davis & Becker (1994) is that water is driven up the borehole when the seafloor pressure is high. Normally, the temperature can be expected to increase with depth below the seafloor and so it is argued that peak upflow will generally be associated with high temperatures. Davis & Becker (1994) suggest that the 'anomalous' thermistor lies in a region of inverse thermal gradient. The suggestion that high temperatures should coincide exactly with peak upflow is challenged in Chapter 6. In Section 6.3.1.3 an analytical poroelastic model is used to suggest that high temperatures lag the vertical velocity by a phase angle in the range [45°, 90°]. However this model also predicts that seafloor temperatures lag the ocean tide by an angle in the range [135°, 225°] which is consistent with the observations of Davis & Becker (1994).

Johnson (1998) reports measurements showing tidal modulation in the conductive heat flow through the seafloor at the Baby Bare Seamount (47.7°N, 127.8°W) which lies on the flank of the Juan de Fuca Ridge. The mean heat flow measured with a thermal blanket was found to be 7 $W.m^{-2}$, and bottom water temperatures were found to vary with a quarter-diurnal period. (This variation may be due to quarter-diurnal variations in the magnitude of the tidal stream as discussed in Section 2.6). The time-series of seafloor heat flow also displays tidal modulation. After the effect of the quarter-diurnal variations in bottom water temperature are

removed, there still remains a semi-diurnal heat flow variation of ±0.1 $W.m^{-2}$ which is attributed to the tidal modulation of the flow beneath the seafloor.

4.2.4 Cascadia Accretionary Prism

Borehole data have been collected on the Cascadia accretionary prism, at ODP hole 892B (44.68°N, 125.12°W) (Davis *et al.,* 1995). Pressure and temperature time-series were obtained for the first 10 months of 1993. The temperature time-series show no evidence of tidal modulation, but the pressure within the sealed hole exhibits distinct tidal periodicity. The pressure signal leads the local ocean tide by 0.3 hours, and is attenuated by a factor of 0.5. Davis *et al.* (1995) show that these observations are consistent with the presence of a layer containing 2% free gas lying above the open section of the borehole. The presence of gas alters the elastic response of the layer and leads to the phase shift, according to the theory of poroelasticity (Van der Kamp & Gale, 1983; Wang & Davis, 1996; Wang *et al.,* 1998). In Chapter 6, a similar investigation of the effect of spatially varying elastic parameters below the seafloor is presented, but with the difference that the spatial variation in elastic properties is caused by the temperature structure of a subseafloor convection cell (Chapter 5), rather than the presence of gas-bearing layers.

A feature of the time-series obtained below the seafloor in boreholes is the purity of the tidal modulation. In contrast, temperature time-series obtained above the seafloor tend to contain a lot of high-frequency noise in addition to any tidal modulation. It is possible that turbulent water motions just above the seafloor lead to this high frequency 'hiss' which often frustrates attempts to make reliable parametric estimates of the tidal modulation. However, the remarkable lack of noise in some of the subseafloor temperature measurements (Davis & Becker, 1994; Davis & Becker, 1999) means that these data would be very well suited to analysis by the Admiralty Method and the HYBRID code (Chapter 3).

4.2.5 The Pipe Organ Site and the Kolmogorov Hypothesis

Temperature measurements in the water column were made by Wetzler *et al.* (1998) at a location 100 m south of the Pipe Organ vent site on the Juan de Fuca Ridge (44.97ºN, 130.21ºW). The data were collected from a vertical instrument array tethered to a seafloor mooring. Water temperature was recorded at heights of 135 m, 165 m and 195 m above the seafloor, and lateral ocean currents were recorded by a sensor 164.5 m above the seafloor. The data span a period of 111 hours between 1997/9/24 and 1997/9/29. Wetzler *et al.* (1998) explain their observations with an advection-diffusion model suggesting that the plume from

the Pipe Organ vent is carried across their instrument array by the ocean currents. From the point of view of this dissertation, it is the possible presence of tidal signals in the time-series which is of interest. When viewed in the time-domain, the current and temperature time-series seem to exhibit a semi-diurnal periodicity. However, when Wetzler *et al.* (1998) calculated windowed periodograms of their time-series they discovered 'no indication of distinct spectral peaks'. It is suggested that use of the superior MWPS spectral estimator might reveal significant spectral lines at the principal tidal frequencies.

An interesting feature of the power spectra obtained by Wetzler *et al.* (1998) is their overall shape, or slope. The spectra lack any obvious peaks, but take the approximate form:

$$\hat{S}(f) = Af^{B} \quad \Leftrightarrow \quad \log\left(\hat{S}\right) = \log(A) + B\log(f) \tag{4.1}$$

for suitable constants A and B. (The value of B represents the slope of the spectrum when viewed on a log-log plot). The three temperature time-series collected at Pipe Organ yielded the values –1.53, –1.72, –1.76 for B. Wetzler *et al.* (1998) note that these values are close to the value of –5/3 suggested by the 'Kolmogorov hypothesis' (Phillips, 1966; Turner, 1973; Phillips 1991a). This hypothesis concerns the power spectrum of the velocity field of a turbulent fluid. If the turbulence is isotropic, dimensional analysis suggests that there is a frequency range over which the power spectrum of the velocity decays as $f^{-5/3}$. Data consistent with the Kolmogorov hypothesis have been found by measuring seawater temperature with a sensor towed behind a ship (Grant *et al.,* 1962). Similar isotropic turbulence might be expected to occur near a seafloor vent in the presence of oceanic currents. A temperature sensor near a hydrothermal vent experiences a relative flow of turbulent water in a manner analogous to the ship-towed sensors of Grant *et al.* (1962). For this reason, the overall shape of estimated power spectra is compared with the predictions of the Kolmogorov hypothesis in the following sections. Consequently, both the low- and high-frequency parts of power spectra obtained from seafloor data are of interest. The low-frequency section is examined for evidence of line components at the tidal frequencies while the high-frequency tail is compared with the predictions of the Kolmogorov hypothesis.

4.3 Gulf of California

4.3.1 Introduction

The hydrothermal activity in the Gulf of California is unique among the sites considered here because it occurs in a gulf rather than an open ocean. In the context of processes linked to the

ocean tides, this is significant because the ocean tide in a gulf may consist of standing waves, while the tide in the open oceans is always composed of travelling waves (Section 2.6). The phase relationship between the ocean tide and the associated tidal streams is therefore different for gulfs than for the open oceans, and care must be exercised when estimating tidal streams from an estimate of the ocean tide.

In Section 4.3.2, a seafloor temperature time-series collected by Little *et al.* (1988) is re-examined in the light of this observation. Little *et al.* (1988) correlated this time-series with a simplistic prediction of the seafloor currents. By making use of the theory of tidal streams (Section 2.6), a more sophisticated estimate of the likely seafloor currents is made.

4.3.2 Guaymas Basin

Little *et al.* (1988, 1989) collected a seafloor temperature time-series in the Guaymas Basin, Gulf of California (27°00'N, 111°24'W), using a thermistor placed 3 cm above an area of diffuse hydrothermal flow. The authors note that the local ocean tide is predominantly diurnal, but that the temperature time-series exhibits semi-diurnal periodicity. The tidal modulations in temperature are therefore unusual in demonstrating a frequency-doubling compared with the local ocean tide. (Other temperature time-series displaying semi-diurnal periodicity tend to occur in areas where the ocean tide is itself predominantly semi-diurnal.) Little at al. (1988) present a model to explain these data in which the thickness of the thermal boundary layer on the seafloor varies according to the magnitude of the tidal stream. The tidal stream is assumed to be proportional to the time derivative of the ocean tide at the town of Guaymas, located 100 km from the hydrothermal site. It is important to note the two assumptions inherent in this model – (1) that the ocean tide at the hydrothermal site is assumed to be the same as that on the coast, and (2) that the tidal streams are assumed to be given by the time derivative of the ocean tide. Both of these assumptions are open to question. The validity of the first assumption is examined in Table 4.3 and Figure 4.4.

The ocean tide at the town of Guaymas (27°55'N, 110°54'W) is predicted using Admiralty Method harmonic constants (Admiralty Tide Tables, Vol. 4). The harmonic constants published by the Admiralty refer to local time at Guaymas, which is 7 hours behind GMT. The waves of the tidal potential travel westwards around the Earth at an angular speed of ~15º per hour (diurnal components) and ~30º per hour (semi-diurnal components). Consequently, the published harmonic constants are here normalised to GMT by adding 105º to the phase-lags of the diurnal components and 210º to the phase-lags of the semi-diurnal components (Figure 4.4a,b).

The harmonic constants for the hydrothermal site itself (27°00'N, 111°24'W) are derived from a synthetic time-series created by the CSR code. Table 4.3 and Figure 4.4 show that the diurnal components of the tide vary little between the town of Guaymas and the hydrothermal site, but there is a slight difference in the phase of the semi-diurnal components. The time-domain graph gives a direct comparison of the two ocean tides over the period of the measurements (Figure 4.4e). The two tides are broadly similar, but the tide at the hydrothermal site has more pronounced double high waters in the first half of the time period.

Gulf of California	H_1 (*M2A*)	g_1 (*M2A*)	H_2 (*S2A*)	g_2 (*S2A*)	H_3 (*K1A*)	g_3 (*K1A*)	H_4 (*O1A*)	g_4 (*O1A*)
Ocean tide (m) at town of Guaymas	0.14	165°	0.11	137°	0.28	179°	0.19	176°
Ocean tide (m) at hydrothermal site	0.215	115°	0.153	120°	0.277	179°	0.178	167°

Gulf of California	$(H_1+H_2)/(H_3+H_4)$	H_1/H_2	g_2-g_1	H_3/H_4	g_4-g_3
Ocean tide (m) at town of Guaymas	0.532	1.273	-28°	1.474	-3°
Ocean tide (m) at hydrothermal site	0.809	1.405	5°	1.556	-12°

Table 4.2: Admiralty Method harmonic constants for the ocean tide at the town of Guaymas (27°55'N, 110°54'W) and at the Guaymas Basin hydrothermal site (27°00'N, 111°24'W).

The second assumption of Little *et al.* (1988, 1989) - that tidal streams are proportional to the time derivative of sea surface height - is examined below. The ocean tide $\zeta(t)$ can be written in terms of Admiralty Method harmonic constants $\{H_1,\ldots,H_4, g_1,\ldots,g_4\}$ as follows:

$$\zeta(t) = \sum_{j=1}^{4} H_j F_j(t) \cos\left(\phi_j(t) - g_j\right) \tag{4.2}$$

On a timescale of a few days, the factors $\{F_j(t)\}$ are approximately constant as functions of time, while the phases $\{\varphi_j(t)\}$ are approximately linear functions of time: $\varphi_j(t) \approx \omega_j t$. Thus:

$$\zeta(t) \approx \sum_{j=1}^{4} H_j F_j \cos\left(\omega_j t - g_j\right) \tag{4.3}$$

and so:

$$\frac{d\zeta}{dt} \approx \sum_{j=1}^{4} -\omega_j H_j F_j \sin\left(\omega_j t - g_j\right) = \sum_{j=1}^{4} \omega_j H_j F_j \cos\left(\omega_j t - \left(g_j - \frac{\pi}{2}\right)\right) \tag{4.4}$$

Equation (4.4) shows that if the ocean tide $\zeta(t)$ has harmonic constants $\{H_j, g_j\}$, then its time derivative has harmonic constants $\{\omega_j H_j, g_j - \pi/2\}$.

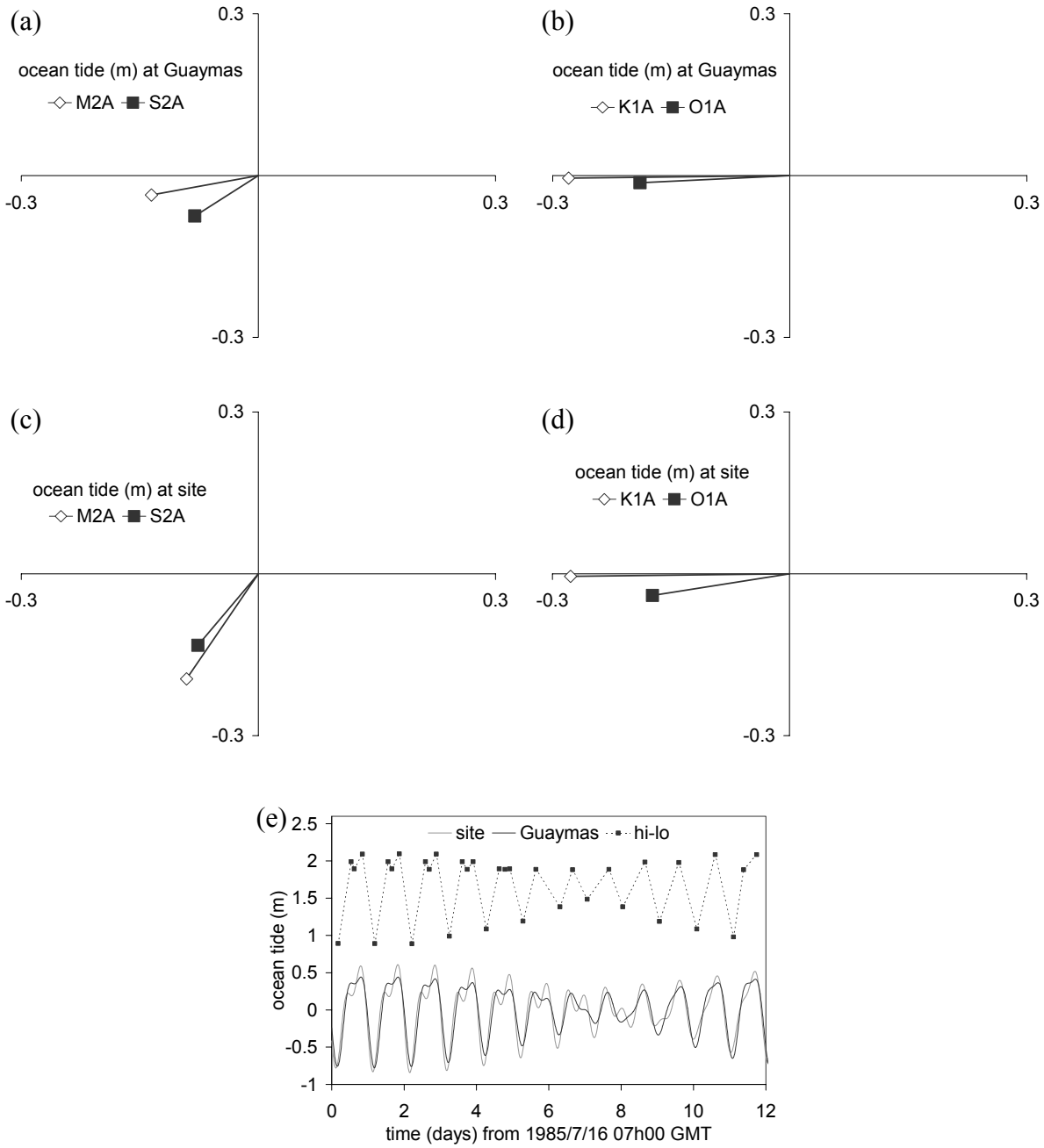

Figure 4.4: The ocean tide at the Guaymas Basin hydrothermal site (27.00°N, 111.40°W), and the town of Guaymas (27.92°N, 110.90°W). (a) – (d) Admiralty Method harmonic constants. (e) Time-domain representation *site* - ocean tide at the hydrothermal site predicted by the CSR code. *Guaymas* – ocean tide at the port of Guaymas from harmonic constants published in tide tables. *hi-lo* – the high and low water points for the port of Guaymas quoted by Little *et al.* (1988, 1989).

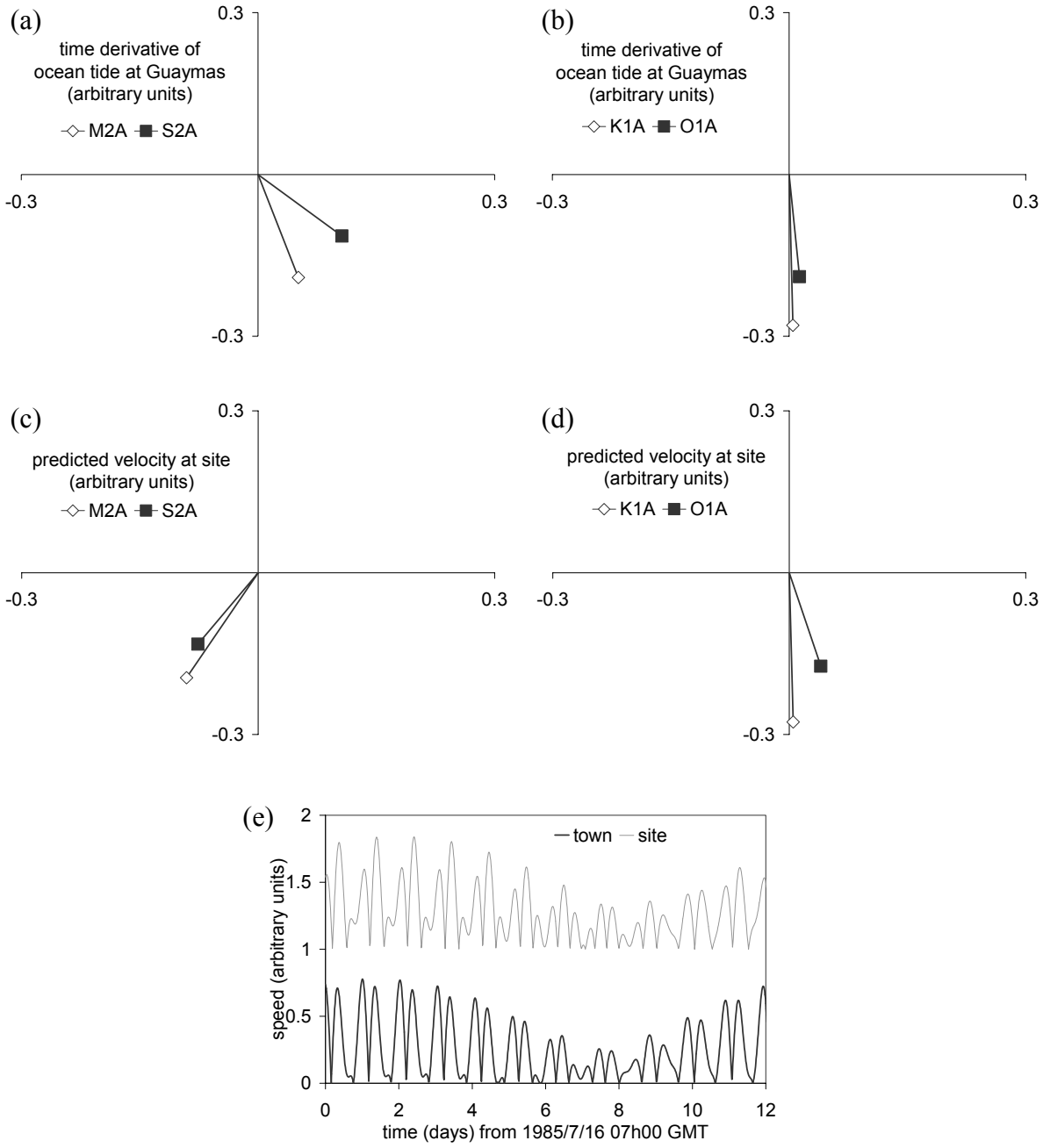

Figure 4.5: Predicted tidal streams at the Guaymas Basin hydrothermal site (27.00°N, 111.40°W), calculated according to the theory of Chapter 2, and at the town of Guaymas (27.92°N, 110.90°W), calculated according to the theory used by Little *et al.* (1988). (a) – (d) Admiralty Method harmonic constants. (e) Time-domain representation. For clarity, the speed for the hydrothermal site is offset by 1 unit on the vertical axis.

In other words, taking a time derivative reduces the phase lag of each component by $\pi/2$ radians (or 90º), and scales the magnitude of each component by its approximate angular frequency ω_j. Therefore the process of differentiation acts as a *high-pass filter*, in which the magnitudes of the semi-diurnal components are doubled relative to the magnitudes of the diurnal components. Figure 4.5 shows harmonic constants for the time derivative of the tidal height at the town of Guaymas, calculated in this way, and expressed in arbitrary units. In other words, the harmonic constants in Figure 4.5a,b were derived from the harmonic constants of the ocean tide at the town of Guaymas (Figure 4.4a,b; Table 4.3) by subtracting 90º from all phase-lags and the doubling the magnitudes of the semi-diurnal components to account for the high-pass filtering. The resulting harmonic constants constitute an Admiralty Method parametric description (in arbitrary units) of the tidal streams as assumed by Little *et al.* (1988). The tidal streams predicted by this model can now be compared with the predictions of a more sophisticated model based on the theory of Section 2.6.

The ocean tide in the Gulf of California has been discussed in some detail by several authors (Filloux, 1973; Quirós *et al.,* 1992; Carbajal & Backhaus, 1998), and a consistent picture emerges from their work. The ocean tide is due to the combination of *standing* diurnal waves and *travelling* semi-diurnal waves, and the associated tidal streams are rectilinear along the gulf. The semi-diurnal waves travel northwestwards (i.e. into the gulf) and are dissipated at the closed northern end. Consequently, the maximum northwestwards semi-diurnal tidal stream coincides with maximum positive semi-diurnal sea surface displacement, and is therefore in phase with the ocean tide (Chapter 2; Doodson & Warburg, 1941). For the diurnal components, which are standing waves, the maximum northwestwards stream coincides with the rising half-tide, and so it leads the ocean tide by 90º. It is therefore possible to derive the harmonic constants of the tidal stream (in arbitrary units) from the harmonic constants of the ocean tide at the hydrothermal site according to this theory (Figure 4.5c,d). There is no high-pass filtering, so the relative magnitudes of the components are the same as for the ocean tide (Figure 4.4c,d). The phase-lags of the travelling semi-diurnal components are unchanged, but the phase-lags of the standing diurnal components must be reduced by 90º. A time-series for the predicted tidal stream magnitude according to this theory is shown in Figure 4.5e alongside a time-series predicted by the simpler theory of Little *et al.* (1988).

It should be noted that the tidal streams predicted by this model differ from those predicted by Little *et al.* (1988) for two reasons. Firstly, the tidal stream has been derived from the ocean tide at the hydrothermal site itself rather than the ocean tide at the town of Guaymas. Secondly, the tidal stream is derived from a rigorous expression taking account of standing and travelling waves, rather than the simple time-derivative of ocean tide height assumed by Little *et al.* (1988).

In summary, it is suggested that the boundary-layer model of Little *et al.* (1988) should be modified to incorporate a more realistic estimate of the tidal streams in the Gulf of California. It would also be desirable to obtain an estimate of the power spectrum of this data using the multiple window method of Section 3.2.2.

4.4 Equatorial East Pacific Rise

4.4.1 Rose Garden Site

Johnson *et al.* (1994) discuss two time-series temperature measurements made at the Rose Garden hydrothermal site at the Galapagos Spreading Centre (0.804167°N, 86.224633°W). Both time-series begin at 1988/4/16 15h00 GMT and are of 18 days duration. The first time-series (Thermistor 2) was obtained from a probe laid on top of a bed of mussels. It reveals semi-diurnal variations of ±1ºC about a mean value of ~3ºC. The second time-series (Thermistor 3) was obtained from a probe which was inserted into a mass of mussels and vestimentiferan worms. Thermistor 3 displayed high temperature peaks at semi-diurnal intervals, although their magnitude varied significantly. For the first 4 days, the high temperature peaks were as much as 12ºC above the baseline temperature of ~4ºC. The magnitude of the peaks dropped to ~1ºC between days 4 and 16, and then increased to ~4ºC. Johnson *et al.* (1994) suggest that this variation in the magnitude of the peaks may be caused by the animals moving the probe, and show that the high temperature peaks from both thermistors occur near the times of low water at the port of Guayaquil (2.20ºN, 79.87ºW). Consequently, Johnson *et al.* (1994) speculate that increased flow of vent fluids occurs when the ocean tide at the Rose Garden site is low.

This conclusion presupposes, however, that the ocean tide at the Rose Garden site is in phase with the ocean tide at the port of Guayaquil. There are at least two reasons why this is unlikely to be the case.

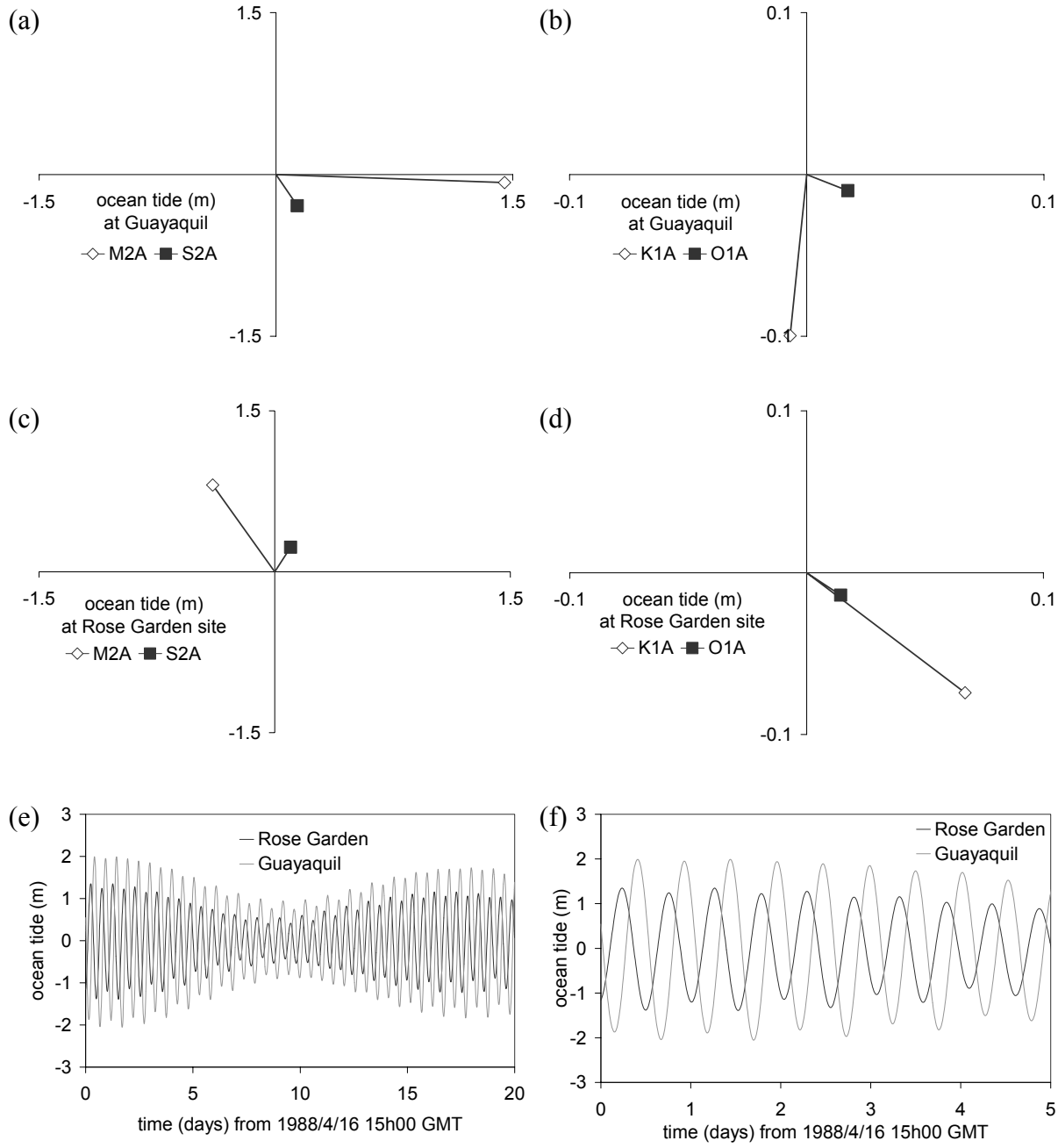

Figure 4.6: Admiralty Method harmonic constants of the ocean tide at the town of Guayaquil (2.20ºN, 79.87ºW), and at the Rose Garden hydrothermal site (0.80°N, 86.22°W). (a) – (d) Admiralty Method harmonic constants. (e),(f) Time-domain representation.

Firstly, the two locations are separated by over 600 km, and secondly the port of Guayaquil lies at the head of a gulf - the Gulf of Guayaquil - where the tide is likely to be very different to that found in the open ocean (Doodson & Warburg, 1941).

The Admiralty Method harmonic constants for the port of Guayaquil (Admiralty Tide Tables, Vol. 4) are compared with those for the Rose Garden Site, which were derived by the HYBRID code from a synthetic time-series created by the CSR code (Table 4.3, Figure 4.6). Table 4.3 shows that semi-diurnal components dominate the ocean tide at both locations, but that the *M2A* and *S2A* components at the Rose Garden site lead those at Guayaquil by 125º.

Rose Garden ocean tides	H_1 (*M2A*)	g_1 (*M2A*)	H_2 (*S2A*)	g_2 (*S2A*)	H_3 (*K1A*)	g_3 (*K1A*)	H_4 (*O1A*)	g_4 (*O1A*)
Guayaquil (m)	1.45	3°	0.32	65°	0.10	94°	0.02	30°
RG site (m)	0.90	244°	0.25	294°	0.10	48°	0.02	44°

Rose Garden ocean tides	$(H_1+H_2)/(H_3+H_4)$	H_1/H_2	g_2-g_1	H_3/H_4	g_4-g_3
Guayaquil	14.8	4.5	62°	5	-64°
RG site	9.6	3.6	50°	5	-4°

Table 4.3: The Admiralty Method harmonic constants for the ocean tide at the port of Guayaquil and at the Rose Garden hydrothermal site.

There are also differences in the diurnal components, but they are of less significance because of their lesser magnitude. The conclusions of Johnson *et al.* (1994) can now be re-examined. They report that high temperature peaks at the Rose Garden site coincide with low tide at the port of Guayaquil. In other words, the temperature signal at the Rose Garden site lags the ocean tide at Guayaquil by ~180°. It follows that the temperature signal at the Rose Garden site lags the *local* ocean tide by a phase angle of ~305°. Thus, the use of the ocean tide at the port of Guayaquil instead of the ocean tide at the Rose Garden site leads to a phase error of 125° (Figure 4.6e,f).

4.4.2 Bio9 Vent Site

Fornari *et al.* (1998) report time-series measurements made at a high-temperature (340ºC) vent at the Bio9 site on the East Pacific Rise (9.83°N, 104.29°W). Their time-series cover periods of between two weeks and ten months, but they find no evidence for tidal influence in their spectral analysis of the data. Unfortunately, they do not report which method of spectral analysis was used. It is possible that the multiple window method might reveal tidal frequencies in their data when other spectral estimators do not. Ocean tide time-series generated by the CSR code show that the ocean tide at the Bio9 site is relatively small, with

a peak amplitude less than 0.4m. It might therefore be speculated that the lack of an obvious tidal signal at the Bio9 vent is a consequence of the fact there is relatively little tidal loading. On the other hand, Shank *et al.* (1995) report that spectral analysis reveals a 'weak ~12.5 h signature' in time-series from temperature probes at the same location.

4.5 Southern East Pacific Rise

4.5.1 The RM24 Site

In 1997, time-series measurements of effluent temperature and velocity were made at the RM24 hydrothermal site on the Southern East Pacific Rise (17.4292ºS, 113.2056ºW) (A. Schultz, *pers. comm.*, 2000). The measurements were made using the Medusa hydrothermal effluent monitoring system developed at the University of Cambridge (Schultz *et al.,* 1996; Dickson, 1997). In the following sections, several references are made to datasets acquired by Medusa systems, and so it is appropriate to review the features of the instrument which are relevant to this dissertation.

4.5.1.1 Overview of the Medusa instrument

The Medusa instrument is essentially a vertical cylinder (~60 cm high, ~10 cm in diameter) which is placed on the seafloor over an area of hydrothermal activity. A gasket system ensures a good seal to the seafloor, and hydrothermal effluent is channeled up the cylinder, where its temperature and velocity are measured. The instrument is also fitted with six 170 ml sample bottles which can draw samples of the effluent at pre-determined times for later chemical analysis. The temperature and velocity sensors are connected to a datalogger which can record time-series of up to one year's duration. The effluent velocity is measured by a propeller mounted inside the instrument. The number of revolutions in a pre-arranged time interval is measured optically and recorded, giving the angular velocity of the propeller. The velocity of the effluent can then be calculated once the system has been calibrated in the laboratory. In this chapter, the symbol v is used to denote an effluent velocity time-series recorded by Medusa.

The Medusa temperature measurements are made as follows. Firstly, a thermistor measures the ambient temperature of the water outside the instrument. The symbol *Th* is used to denote this measurement. Secondly, the temperature of the effluent inside the instrument is measured by two separate thermocouples – a type-K and a type-T. These thermocouples provide two independent measurements of the difference in temperature between the ambient

water outside the instrument and the effluent water inside the instrument. The measurements yielded by the two thermocouples are labelled *Tk* and *Tt*, respectively. It should be noted that the time-series are recorded initially in uncalibrated form, and can only be expressed in dimensional form (i.e. $mm.s^{-1}$ and ºC) after the sensors have been calibrated. Currently, some Medusa time-series remain uncalibrated, but it is still possible to look for tidal signals in the raw, uncalibrated data. In the cases where the thermistor and thermocouple readings have been calibrated to degrees Celsius, the actual temperature of the effluent can be calculated. It is the sum of the thermistor temperature and the temperature difference across either of the thermocouples. There are therefore two measures of effluent temperature, which are labelled *Tefftk* (= *Th* + *Tk*), and *Tefft* (= *Th* + *Tt*).

4.5.1.2 Medusa measurements – time-domain

The data collected by Medusa at the RM24 site span a period of 240 days from 1997/8/5 and are shown in the time-domain in Figure 4.7. The original time-series (sampling interval 15 s) have been low-pass filtered with a moving median filter of length 60 to produce time-series with a sampling interval of 15 min (Schultz *et al.,* 1992). In this dissertation, all Medusa time-series data have been low-pass filtered in this way prior to analysis.

The overview of the *Th*-signal in Figure 4.7a shows that the ambient temperature oscillated around a reasonably constant mean value over the observation period. For the time period between 80 and 120 days there is clear evidence of variation in the magnitude of the oscillations. This is consistent with a springs/neaps tidal cycle. The close-up view in Figure 4.7e shows that there is an underlying semi-diurnal periodicity to the *Th*-signal. The overview of the *Tk*- and *Tt*-signals in Figure 4.7b displays no obvious long-term trend, but shows that the *Tk*- and *Tt*-signals remained proportional to each other throughout the observation period. This proportionality is not surprising since the two signals are independent, uncalibrated measurements of the same physical quantity. Nonetheless, the observation is worthwhile since it provides evidence that neither sensor failed during deployment (cf. Section 4.7). The close-up view of the *Tk*-signal in Figure 4.7f does not reveal any clear tidal periodicity.

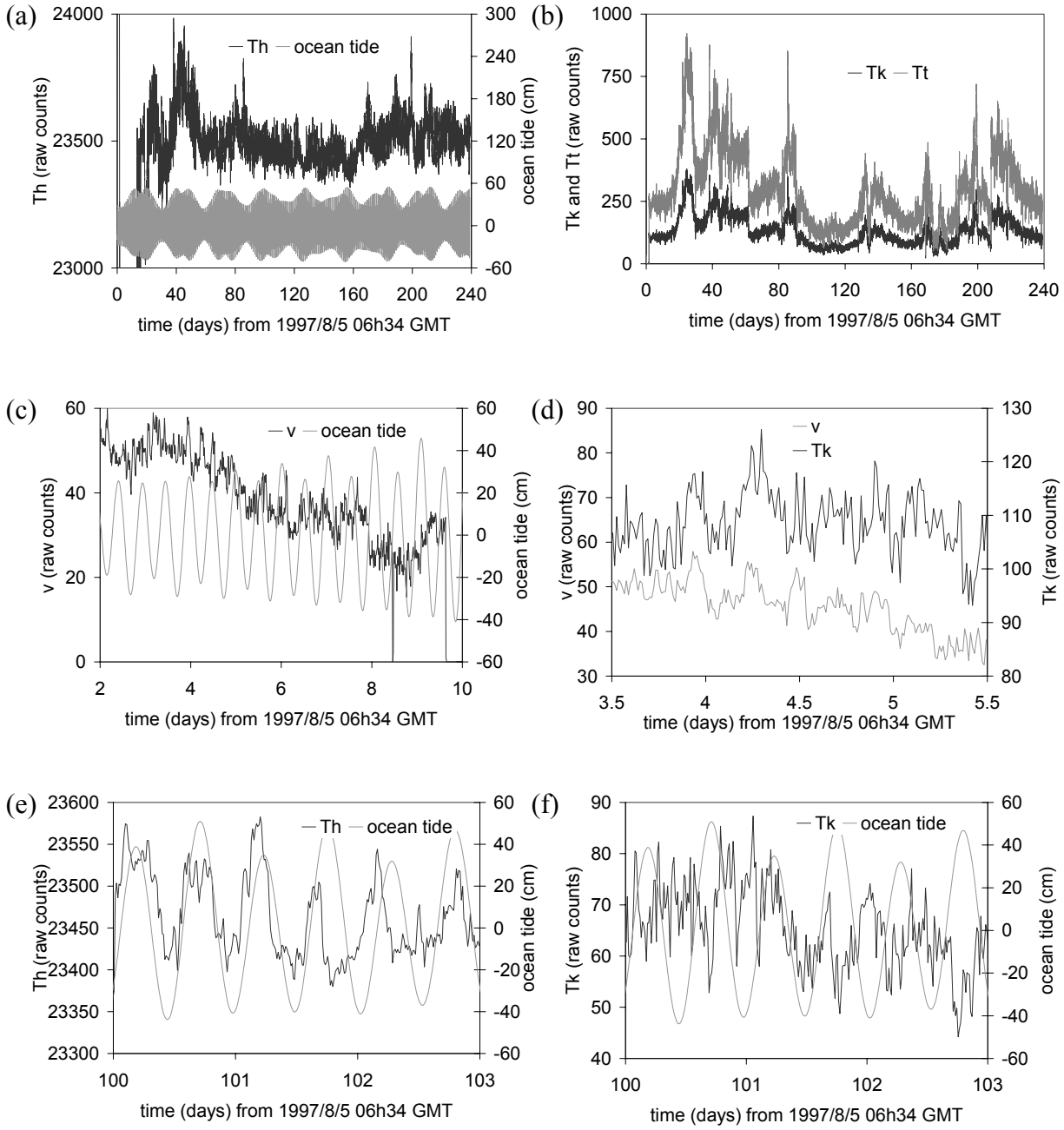

Figure 4.7: Uncalibrated data collected by Medusa at the RM24 site (17.4292ºS, 113.2056ºW) on the Southern East Pacific Rise. *Th* – ambient (thermistor) temperature, *Tk* – temperature difference across thermocouple, *v* – effluent velocity.

The effluent velocity time-series (*v*) is shown in Figure 4.7c. These data cover a much shorter time period (8 days) than the temperature data (240 days) and display a linear downward trend until day 10 when the record stops. It may be that this was caused by a steady increase in the frictional resistance of the propeller of the velocity sensor. Possible

explanations for this friction include thermal expansion in the bearings and/or the precipitation of mineral deposits. There is no obvious diurnal or semi-diurnal periodicity in the record, but there is a short period (between day 4 and day 5) where peaks in the *v*-signal seem to occur at quarter-diurnal intervals, so that they coincide with both high tide and low tide in the ocean. Since the RM24 site is in the open ocean it is expected that peak tidal streams occur at low and high tide (Chapter 2). Consequently, this small section of the record is consistent with a Bernoulli effect explanation of variations in effluent velocity (Schultz & Elderfield, 1997). At low and high tide, when the magnitude of tidal streams is large, the lateral flow of ocean currents across the top of the Medusa might lead to reduced pressure at the top of the instrument and draw fluid upwards. Figure 4.7d shows that increased effluent velocity correlates with an increased temperature difference across the thermocouples. Thus, a highly speculative explanation for this section of the dataset is that warm fluid is drawn upwards through the instrument at high and low tide, driven by tidal streams causing reduced pressure at the top of the Medusa.

4.5.1.3 Medusa measurements – non-parametric analysis

Power spectra for the *Th*-, *Tk*- and *v*-signals are shown in Figure 4.8. All power spectra were obtained from the low-pass filtered (15 min sampling interval) time-series using the MWPS code. The *Th*- and *Tk*-signals each consisted of N=22,937 datapoints (239 days), and the shorter *v*-signal had N=775 datapoints (8 days). Accordingly, the power spectra for the *Th*- and *Tk*-signals were calculated using a time-bandwidth product of 10, with 20 eigenspectra and a 96-point (= 24 h) autoregressive prewhitening filter. The power spectrum for the *v*-signal was calculated using a time-bandwidth product of 1, with 2 eigenspectra and a 96-point autoregressive filter. The low time-bandwidth product was required in order to get reasonable frequency resolution, but means that the variance of the estimated power spectrum is relatively large.

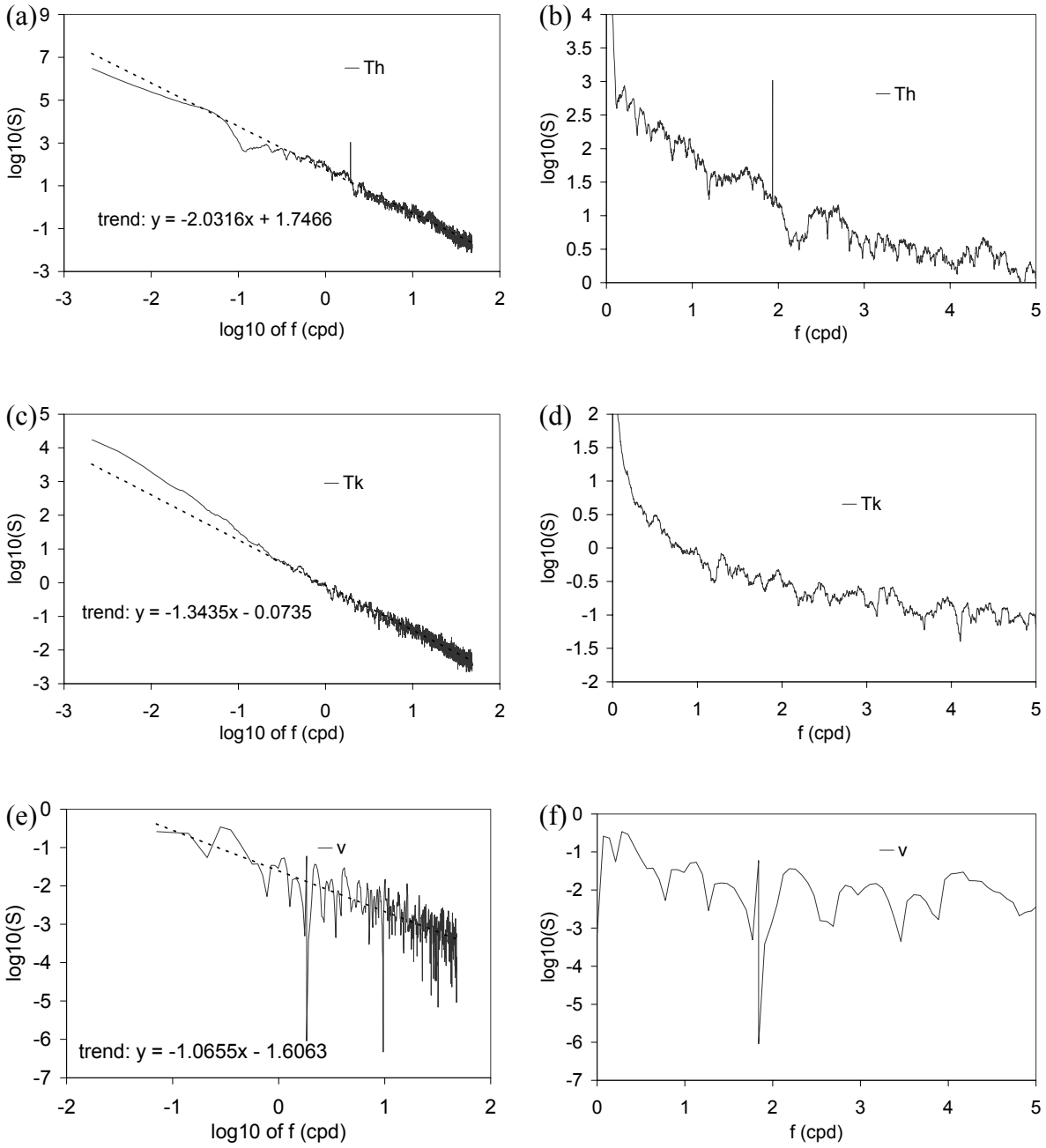

Figure 4.8: Spectral estimates for the data collected by Medusa at the RM24 site (17.4292ºS, 113.2056ºW), calculated using the MWPS code. *Th* – ambient (thermistor) temperature, *Tk* – temperature difference across thermocouple, *v* – effluent velocity.

Figures 4.8a and 4.8b show the estimated power spectrum of the *Th*-signal. The general trend of the spectrum (Figure 4.8a) is of the form $\hat{S}(f) \sim f^{-2}$, which is inconsistent with the $f^{-5/3}$ prediction of the Kolmogorov hypothesis (Section 4.2.5). A close up view of the spectrum (Figure 4.8b) shows that a single significant line component was found at 1.933 ± 0.002 cpd.

(The uncertainty in the location of the line component is equal to the spacing of the frequency bins $1/(N\Delta t)$).This line component can be identified with the *M2* tidal component (1.932 cpd) and provides strong evidence that the *Th*-signal is tidally modulated. There is no evidence of significant power in the diurnal frequency band (Figure 4.8b).

The power spectrum of the *Tk*-signal shows that no significant line components were identified and that it has a general trend $\hat{S}(f) \sim f^{-1.34}$ (Figures 4.8c,d). Since the *Tt*-signal is proportional to the *Tk*-signal in the time-domain (Figure 4.4b), its power spectrum can be expected to exhibit the same features and is not shown here.

The power spectrum of the *v*-signal (Figures 4.8e,f) is of limited use because of the short length of the original time-series. Nonetheless, it is interesting that a single significant line component was identified at 1.84 ± 0.07 cpd. This range includes the *N2* tidal component (1.90 cpd), but not the *M2* component (1.93 cpd) which is usually dominant. Given the shape of the spectrum, the safest conclusion is to say that no positive evidence of tidal modulation is provided by this spectral estimate. On the other hand, the short time-series means that the existence of tidal modulation cannot be ruled out. The general trend of the spectrum, $\hat{S}(f) \sim f^{-1.07}$ is not consistent with the 'five-thirds' law. No strong inferences can be made because of the limited length of the original time-series.

In summary, the non-parametric spectral estimates provide strong evidence for tidal modulation of the *Th*-signal, but no strong evidence for tidal modulation of the *Tk*-, *Tt*- or *v*-signals.

4.5.1.4 Medusa measurements – parametric analysis

Of the time-series collected by Medusa at RM24, only the *Th*-signal shows strong evidence of tidal modulation. Accordingly, it is only for this *Th*-signal that the Admiralty Method harmonic constants are estimated. These estimates are compared with the harmonic constants for the local tidal potential and ocean tide in Table 4.4. The harmonic constants are also shown graphically in the complex plane in Figure 4.9.

An attempt was made to decompose the whole of the *Th*-signal using the Bayesian drift technique (Section 3.3.3) but it was unsuccessful. The algorithm placed a large proportion of the power at semi-diurnal frequencies into the drift component rather than the parametrised tidal component. Consequently, the harmonic constants reported here were estimated by

Huber-weighted section averaging with mean removal using the HYBRID code (Section 3.3.4).

RM24	H_1 (*M2A*)	g_1 (*M2A*)	H_2 (*S2A*)	g_2 (*S2A*)	H_3 (*K1A*)	g_3 (*K1A*)	H_4 (*O1A*)	g_4 (*O1A*)
potential ($m^2.s^{-2}$)	2.57	225°	1.2	226°	0.914	293°	0.647	294°
ocean (m)	0.34	21°	0.06	246°	0.06	358°	0.02	341°
Th (raw counts)	15.98	346°	5.54	357°	16.33	175°	16.95	130°

RM24	$(H_1+ H_2) / (H_3 + H_4)$	H_1 / H_2	$g_2 – g_1$	H_3 / H_4	$g_4 – g_3$
tidal potential	2.42	2.14	< 1°	1.41	< 1°
ocean tide	5	5.67	-135°	3	-17°
Th	0.65	2.88	10.65°	0.96	-44°

Table 4.4 The Admiralty Method harmonic constants of the tidal potential, ocean tide, and those estimated for the Medusa *Th*-signal, at the RM24 site.

The original time-series (of N=22,937 points) was split into 112 overlapping sections of 672 points (= 7 days), giving a 30% offset between sections. Harmonic constants were estimated for each section, following subtraction of the mean value for the section. The final estimates of the harmonic constants are Huber-weighted averages taken over the sections. The error bars represent 95% confidence intervals, assuming that the real and imaginary parts of each harmonic constant are independently normally distributed over the sections (Section 3.3.4).

Using Table 4.4 and Figure 4.9, the harmonic constants of the output signal (*Th*) can be compared with those of the two postulated input signals (the tidal potential and the ocean tide). Within the semi-diurnal band, the *M2A* component dominates the *Th*-signal and is roughly in phase with the *M2A* component of the ocean tide. (For this *M2A* component, the *Th*-signal leads the ocean tide by ~35°). However, this is the only significant point of similarity between the *Th*-signal and the ocean tide. When compared according to the diagnostic measurements listed in Table 4.4, the *Th*-signal seems to bear more similarity to the tidal potential than to the ocean tide. For example, the relative magnitude of semi-diurnal and diurnal components - defined as $(H_1+ H_2)/(H_3 + H_4)$ - is 0.65 for the *Th*-signal, which is indicative of a mixed tide, containing similar proportions of the total power in the diurnal and semi-diurnal bands. The value of 2.42 for the tidal potential is also indicative of a mixed tide, albeit with much more power in the semi-diurnal band. In contrast, the value of 5 for the ocean tide is characteristic of a strongly semi-diurnal signal.

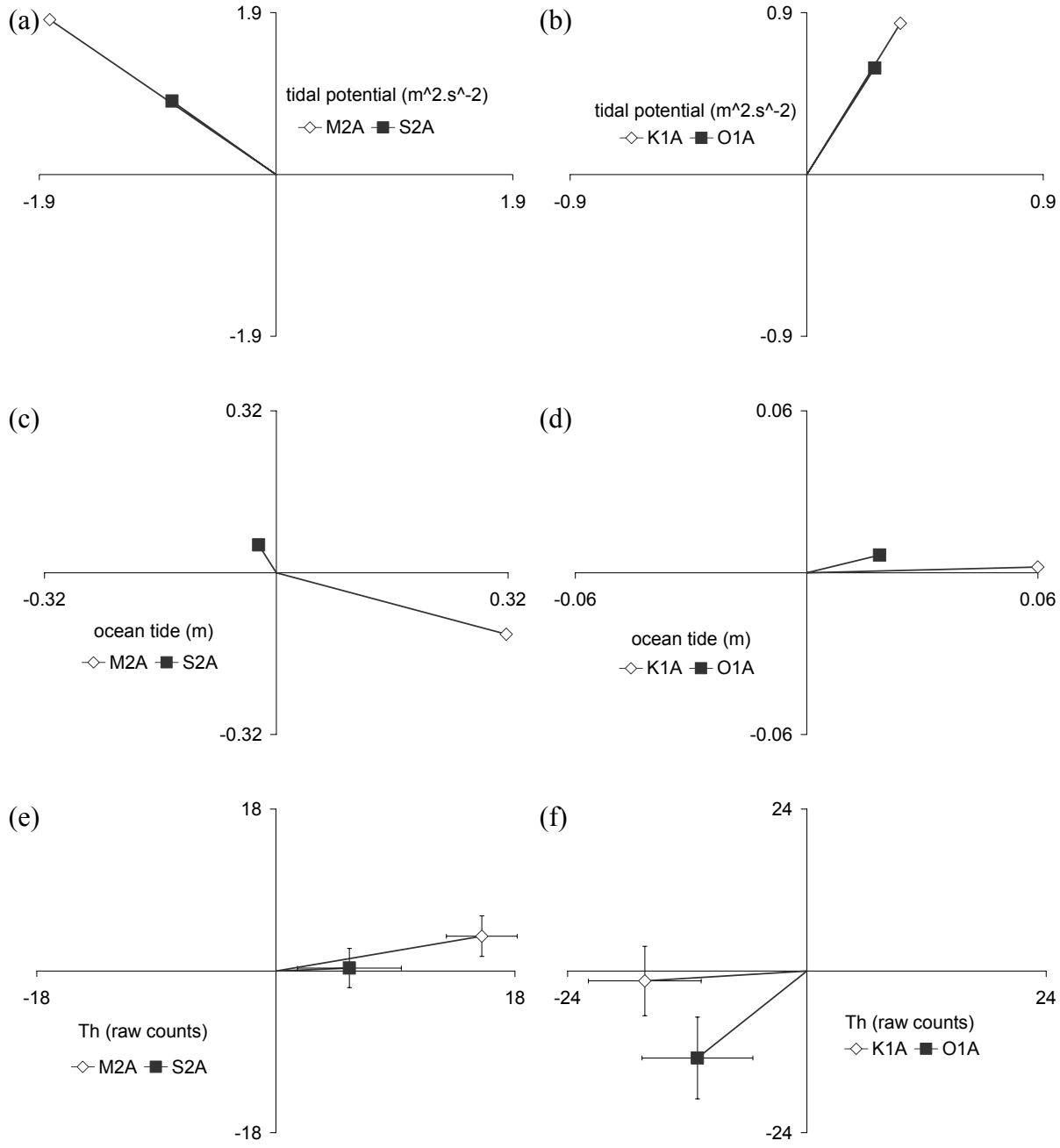

Figure 4.9: Admiralty Method harmonic constants for the RM24 site (17.4292ºS, 113.2056ºW) estimated using the HYBRID code. *Th* – ambient (thermistor) temperature, *Tk* – temperature difference across thermocouple, *v* – effluent velocity.

The relative magnitudes of the semi-diurnal components - defined as the ratio H_1/H_2 - also suggest that the *Th*-signal ((H_1/H_2)=2.88) is more similar to the tidal potential ((H_1/H_2)=2.14) than the ocean tide ((H_1/H_2)=5.67). The difference in phase lag between the semi-diurnal components reinforces this observation. The value obtained for the *Th*-signal ($g_2–g_1$=10.65°) is nearer to that of the tidal potential ($g_2–g_1$<1°) than that of the ocean tide ($g_2–g_1$=-135°).

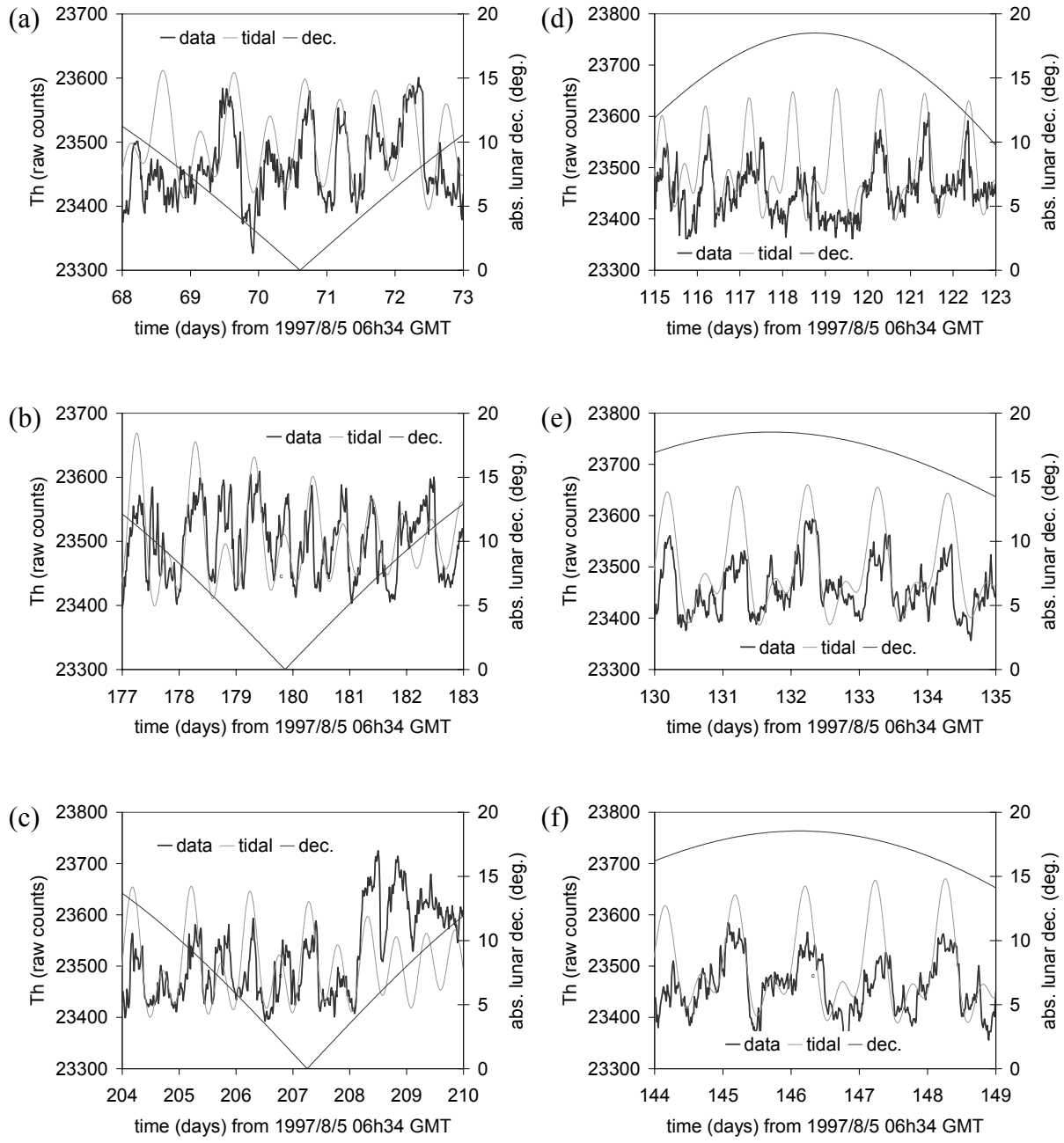

Figure 4.10: The *Th*-signal collected by Medusa at the RM24 site (17.4292ºS, 113.2056ºW). *data* – raw data. *tidal* – the best-fit tidal signal, generated by the harmonic constants of Table 4.4. (For display, this 'tidal' signal has been stretched by a factor of 3 and offset by 23,500.) *dec.* – absolute value of the lunar declination.

Similar observations can be made regarding the relative magnitudes and phases of the diurnal components, but it must be borne in mind that the relative uncertainty in these estimates is much greater, as illustrated by the error bars in Figure 4.9f.

The Admiralty Method harmonic constants derived from the *Th*-signal (Table 4.4) define a tidal signal in the time-domain according to equation (3.15). Figure 4.10 illustrates how well this synthetic tidal signal reflects the original time-series from which the harmonic constants were extracted. The original *Th*-signal (labelled 'data') is plotted alongside the time-series generated by the harmonic constants (labelled 'best fit'). (For display purposes, the 'best fit' signal has been stretched by a factor of 3 and offset by 23,500). The short time periods shown in Figure 4.10 were chosen for display as being those where tidal frequencies were most apparent in the *Th*-signal. It is clear that the data time-series is sometimes predominantly semi-diurnal (Figure 4.10a,b,c) and sometimes predominantly diurnal (Figure 4.10d,e,f). This non-stationary behaviour is closely reflected in the 'best fit' time-series, and can be correlated with the absolute value of the lunar declination which is also shown in Figure 4.10. The 'data' time-series appears to be more strongly semi-diurnal when the lunar declination is small, and more diurnal when the lunar declination is large. This behaviour is predicted by astronomical theory of Section 2.3.2, and provides further evidence that the *Th*-signal is tidally modulated. The existence of time periods where the *Th*-signal exhibits clear diurnal periodicity (Figure 4.10d,e,f) is another illustration of the difference between the *Th*-signal and the local ocean tide. The ocean tide at this site is so strongly semi-diurnal that successive high tides are always separated by ~12 h, and never by ~24 h (e.g. Figure 4.7c).

In summary, the parametric description of the *Th*-signal seems to correlate more closely with the tidal potential than with the ocean tide. This is rather surprising, as there is no obvious mechanism by which the local tidal potential (and hence the solid tide) could influence ambient seafloor temperatures. However, the theory of Little at al. (1988, 1989) provides a plausible link between ambient temperature and tidal streams. If the tidal streams were rectilinear, and not superimposed on a strong background current, this mechanism would lead to frequency-doubling of the temperature signal relative to the ocean tide. The ocean tide at RM24 is strongly semi-diurnal (Table 4.4), and so the associated variations in the *Th*-signal would be quarter-diurnal. However, the *Th*-signal displays virtually no evidence of quarter-diurnal oscillation (Figures 4.7e, 4.8b, 4.10). Thus, if the *Th*-signal is modulated by tidal streams, the streams must be rotating and/or be superimposed on a background current of comparable magnitude.

4.6 Western Pacific

Sato *et al.* (1995) report the results of measurements made using an Ocean Bottom Seismometer with Hydrophone (OBSH) in the South Mariana Trough (13.38°N, 143.92°E). These data were collected at a depth of 1470 m below sea level over a period of 8 days beginning at 1993/10/21. For the first four days of the deployment, the instrument was within 1 m of a hydrothermal vent. It was then moved and spent the remaining four days at a distance of 10 m from the original vent, in an area free from hydrothermal activity. The first four days were marked by a large number of pressure pulses recorded by the hydrophone. These pressure pulses typically lasted between 20 and 60 seconds, and had a negative first break. They were not accompanied by any signal on the seismometers. The frequency with which these pressure events occurred exhibited a periodicity of ~12 h, and appeared to be highest when the local ocean tide was high. During the second 4-day period of the time-series, when the OBSH was placed 10 m from the vent, the pressure events became less frequent and their frequency of occurrence did not exhibit a semi-diurnal periodicity. Sato *et al.* (1995) conclude that the pressure events were caused by the sudden upwelling of hot hydrothermal fluid in the vent. They note that these upwelling events seem more frequent when the local ocean tide is high (i.e. when the hydrostatic pressure on the seafloor is greatest). Therefore these data suggest that episodic hydrothermal activity is most frequent at high tide.

4.7 Mid-Atlantic Ridge

4.7.1 The TAG mound

The TAG hydrothermal mound (26.13°N, 44.82°W) is an active hydrothermal area on the Mid-Atlantic Ridge at a depth of 3700 m below sea level. The mound itself is roughly circular with a diameter of 200 m, and it rises 70 m above the seafloor. At the centre of the mound is an area of vigorous hydrothermal venting known as the Central Black Smoker Complex (CBC) which contains black smokers venting at 360°C - 366°C. In addition to the CBC, there are other areas of the TAG mound where hydrothermal effluent has been observed. This non-CBC effluent ranges from warm, diffuse flow (~20°C), to further high-temperature black smokers.

In 1994, several researchers visited the site and made time-series measurements on the TAG mound, at a time when it was being drilled as part of the Ocean Drilling Program (ODP). As

well as revealing the effect of ocean drilling on hydrothermal effluent, many of these time-series display evidence of tidal modulation. The aim of this section is to collate all of the time-series measurements made at TAG to see if a consistent picture emerges (Kinoshita *et al.,* 1996; Schultz *et al.,* 1996; Fujioka *et al.,* 1997; Kinoshita *et al.,* 1998; Copley *et al.,* 1999).

4.7.1.1 Water column measurements

Kinoshita *et al.* (1996, 1998) report time-series temperature measurements made at TAG using two types of instrument – the Giant Kelp (which measures temperature above the seafloor) and the Daibutsu (which measures temperature on and below the seafloor).

The Giant Kelp records the temperature in the bottom 50 m water column and consists of a vertical string of eight thermistors tethered to the seafloor. Three Giant Kelps were deployed on the periphery of the CBC at TAG, and the resulting time-series display periodic behaviour with a dominant period of ~12 h. After comparing these temperature data with current meter readings (Fujioka *et al.,* 1997), Kinoshita *et al.* (1998) conclude that the hydrothermal plume from the CBC is deflected by tidal currents.

4.7.1.2 Geothermal probe measurements

The Daibutsu instrumented is designed to measure temporal changes in the conductive heat flow from sediments, and consists of eight geothermal probes, each of which is 80 cm long and contains five thermistors mounted at intervals of 17.5 cm. At TAG, an attempt was made to insert the probes at several locations to the south and west of the CBC (Kinoshita *et al.* 1996; Kinoshita *et al.,* 1998). Some of the probes failed to penetrate the sediment and were left on the seafloor to record bottom water temperature. The remaining probes penetrated the sediment partially, so that some of their thermistors were above the seafloor and some below. All of the thermistors which were above the seafloor produced similar time-series showing that bottom water temperature is typically 2.66°C, but with periodic high temperature 'spikes', in which the temperature is raised by between 0.02°C and 0.8°C. These spikes recur at intervals of ~12 h and ~ 24 h. Kinoshita *et al.* (1996, 1998) attribute these variations to the advection of non-buoyant effluent by tidal currents. One interesting feature of the data, which they do not discuss, is the fact that successive spikes are sometimes separated by ~12 h and sometimes separated by ~24 h. A possible explanation for this behaviour lies in the springs/neaps cycle of lunar phases. Kinoshita *et al.* (1998) note that the currents on the seafloor at TAG are predominantly westward. They conclude that there is a background (i.e.

non-tidal) westward current of ~10 cm.s^{-1} upon which tidal streams of the same order of magnitude are superimposed. Thus, the magnitude and direction of the overall current is highly sensitive to the magnitude of the tidal streams. It may be that when tidal streams are large (at springs), they are just sufficient to produce a reversal in the direction of overall current twice per day. However, when tidal currents are small (at neaps), such current reversals may only occur for the larger of that day's tides, or not at all. This tentative explanation for bottom water temperatures is consistent with the published data.

The temperature time-series produced by the subseafloor Daibutsu thermistors appear qualitatively different to those obtained on the seafloor. An example is provided by the subbottom time-series shown in figure 4 of Kinoshita *et al.* (1996), which was obtained at a depth of 44 cm below the seafloor. It is relatively smooth and has the appearance of a pure tidal signal in the sense defined in Chapter 2. In other words, its power spectrum is dominated by diurnal and semi-diurnal oscillations. In contrast, the spiky time-series obtained above the seafloor would have power spectra containing significant power at higher frequency harmonics.

Kinoshita *et al.* (1998) suggest that the subseafloor temperature variations are caused by thermal diffusion of the variations in bottom water temperature down through the sediment. This assertion can be examined more closely with the aid of a simple one-dimensional model of thermal diffusion in seafloor sediment. Let $T(z,t)$ be the temperature perturbation at time t and depth z below the seafloor. Assuming that the seafloor sediment has a constant thermal diffusivity (κ) it then follows that $T(z,t)$ obeys the heat conduction equation:

$$\frac{\partial T}{\partial t} = \kappa \frac{\partial^2 T}{\partial z^2} \quad for \quad z > 0 \tag{4.5}$$

This can be solved subject to a prescribed tidally modulated temperature at the seafloor. The seafloor temperature can be written as a (complex) Fourier series as follows:

$$T(0,t) = \sum_{j=1}^{N} T_j \exp(i\omega_j t) \tag{4.6}$$

It then follows that the temperature in the sediment at depth z is given by:

$$T(z,t) = \sum_{j=1}^{N} T_j \exp\left(-\sqrt{\frac{\omega_j}{2\kappa}}z\right)\exp\left(i\omega_j t - i\sqrt{\frac{\omega_j}{2\kappa}}z\right) \tag{4.7}$$

Considering each harmonic component separately, it is possible to compare the temperature at depth z with the temperature at the seafloor. Equation 4.7 shows that, at depth z, the component at angular frequency ω_j is attenuated in magnitude by a factor:

$$\varepsilon_j(z) = \exp\left(-\sqrt{\frac{\omega_j}{2\kappa}}z\right) \tag{4.8}$$

and delayed in phase by a (radian) angle:

$$\phi_j(z) = \sqrt{\frac{\omega_j}{2\kappa}}z \tag{4.9}$$

It is possible to test whether the measured temperatures fit this simple model. If the data are compatible with the model, empirical values of attenuation and phase-lag (at a given frequency) should obey equations (4.8) and (4.9) so that:

$$\phi_j(z) = -\ln(\varepsilon_j(z)) \tag{4.10}$$

Kinoshita *et al.* (1998) report that amplitudes decrease and phase lags increase with distance below the seafloor, which is in qualitative agreement with the model. Unfortunately, a quantitative test of the model can only be made using the data from a single subseafloor thermistor, as only one suitable time-series is plotted in sufficient detail by Kinoshita *et al.* (1996).

This subseafloor time-series was obtained at a depth z=0.44 m, and is dominated by semi-diurnal oscillations (ω_1=1.45 · 10^{-4} s^{-1}). This semi-diurnal component has an attenuation factor, ε_1, which lies in the range 0.4 to 0.5 (Kinoshita *et al.,* 1996). According to the theory above, this should correspond to a phase-lag, φ_1, of between 0.693 and 0.916 radians (i.e. between 40° and 52°). However, the observed semi-diurnal phase-lag is much larger - its value of 1.57 radians (90°) would be compatible with an attenuation factor of 0.2. Hence, the simple model of equations (4.5) – (4.10) is insufficient to explain the data.

There are many possible explanations for the failure of the model, of which the two simplest are considered here. Firstly, it may be that the subseafloor oscillations are, indeed, caused by the variation in bottom water temperature, but that the thermal diffusivity is not constant with depth. This possibility cannot be ruled out, but there is no obvious reason why the thermal properties of sediment should vary significantly over such a small distance (0.4 m). Secondly, it may be that the tidal variations in subseafloor temperature are not caused by the concurrent tidal variations in bottom water temperature, but by some process which occurs at a deeper level *below* the seafloor. This possibility is discussed in greater detail in Chapter 6.

Here, it is sufficient to note the phase relationship of the subseafloor oscillations to the ocean tide. Kinoshita *et al.* (1996) record that subseafloor temperatures lag the local ocean tide by ~90°. In other words, the highest subseafloor temperatures coincide with the falling half-tide. It should be noted that this phase lag is incompatible with the prediction that tidal variations in temperature at the seafloor lag the ocean tide by a phase angle in the range [135°, 225°] (Section 6.3).

4.7.1.3 Medusa measurements – time-domain

Schultz *et al.* (1996) report time-series measurements made at TAG using a Medusa hydrothermal monitoring system (Section 4.5.1). The Medusa was deployed on an area of vigorous diffuse flow, 50 m East of the CBC and within one metre of a small black smoker chimney. Time-series of ambient bottom water temperature (*Th*) and effluent velocity (*v*) were obtained, along with time-series for the two thermocouples (*Tk* and *Tt*). Following calibration of the temperature data (Dickson, 1997), two time-series for effluent temperature were constructed: *Teffk* = *Th* + *Tk*, and *Tefft* = *Th* + *Tt*. The data shown in figure 4.11 span a period of 100 days from 1994/9/21. The original time-series (sampling interval 15 s) have been low-pass filtered with a moving median filter of length 60 to produce time-series with a sampling interval of 15 min (Schultz *et al.,* 1992).

The overview of the *Th*-signal (Figure 4.11a) shows that the ambient temperatures oscillated about a baseline value throughout the observation period. This baseline temperature displays an upward trend from ~3.5°C at the beginning of the record to ~5°C at the end. Over this period, there is a corresponding increase in the magnitude of the oscillations from 0.5°C to 1.5°C. The close-up view of the *Th*-signal (Figure 4.11e) shows that the oscillations are semi-diurnal and in-phase with the ocean tide. In other words, the highest ambient temperatures coincide with high tide.

The effluent velocity channel (*v*) functioned successfully for only 4 days, after which it operated sporadically (Figure 4.11b). The close-up view of the *v*-signal (Figure 4.11f) covers approximately the same time period as Figure 3 of Schultz *et al.* (1996), and displays essentially the same data. However, the *v*-signal plotted in Schultz *et al.* (1996) appears much smoother because it has been low-pass filtered with a longer moving-average filter. Schultz *et al.* (1996) discern diurnal periodicity in their (more heavily smoothed) *v*-signal. In contrast, the *v*-signal in Figure 4.11f does not display any obvious periodicity at tidal frequencies.

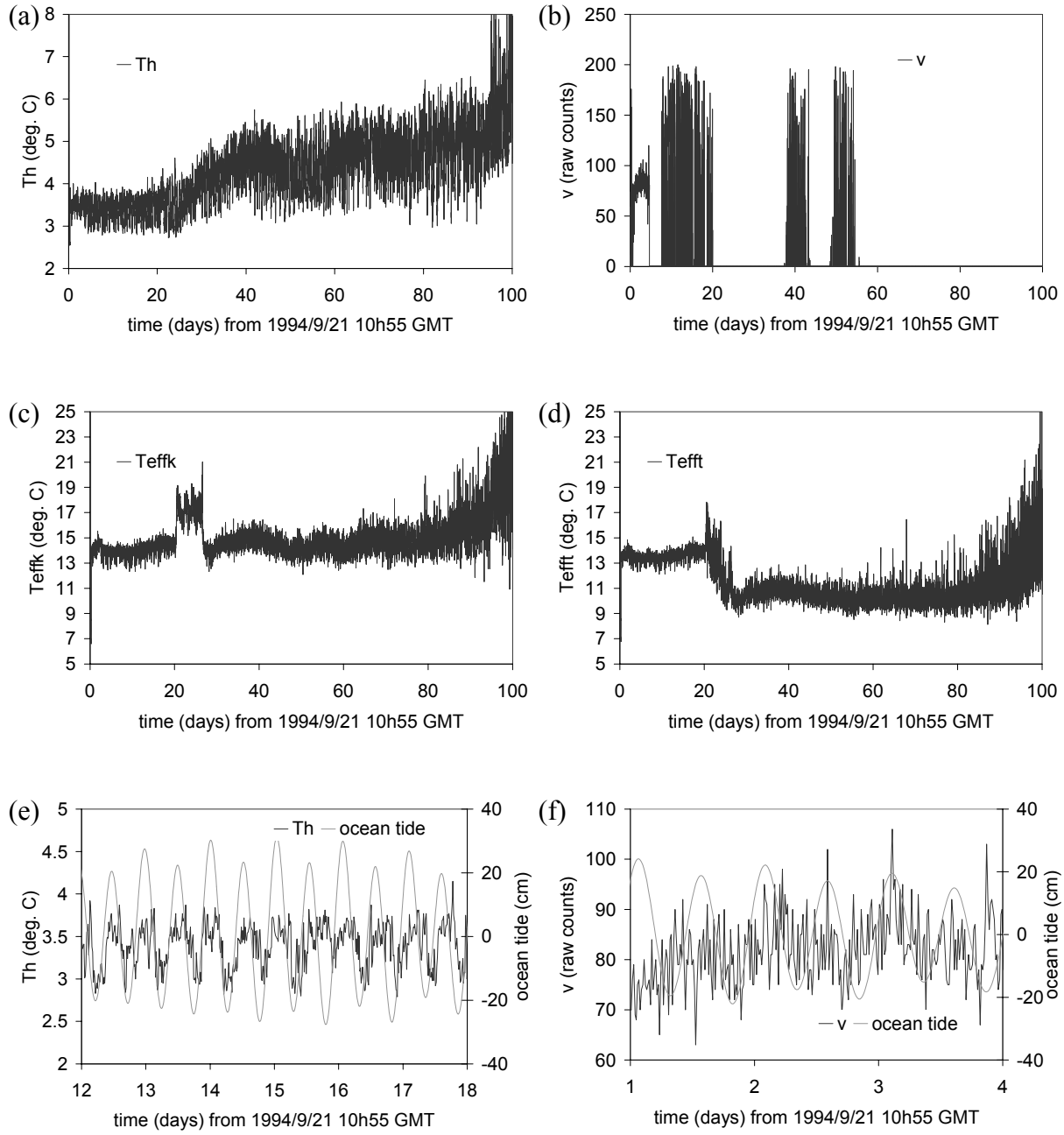

Figure 4.11: Data collected by Medusa at the TAG site (26.13ºN, 44.82ºW) on the Mid-Atlantic Ridge. *Th* – ambient (thermistor) temperature, *Tefffk*, *Tefft* – effluent temperature, *v* – effluent velocity.

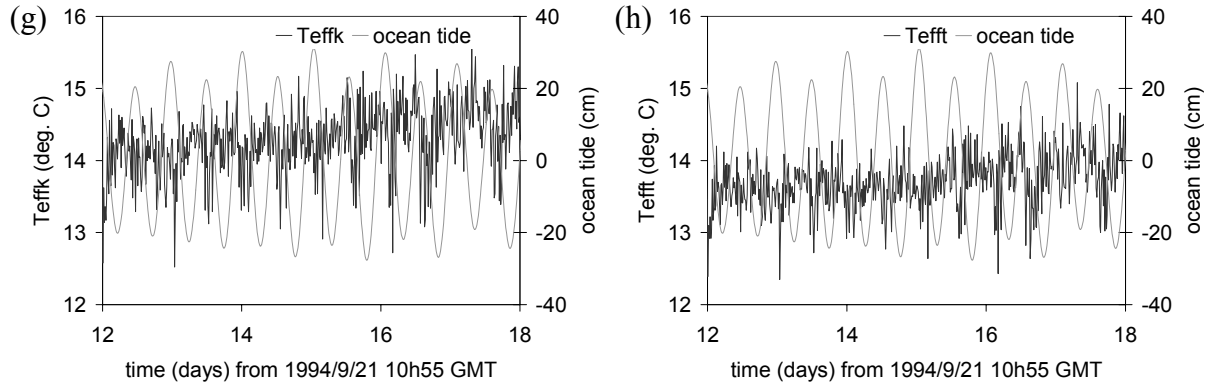

Figure 4.11: (continued) Data collected by Medusa at the TAG site (26.13ºN, 44.82ºW) on the Mid-Atlantic Ridge. *Th* – ambient (thermistor) temperature. *Teffk*, *Tefft* – effluent temperature. *v* – effluent velocity.

Overviews of the two estimates of effluent temperature (*Teffk* and *Tefft*) are shown in Figure 4.11c,d. There is general agreement between the two signals until day 20. In this initial period, the effluent temperature displays semi-diurnal oscillations of ~1°C about a baseline value of ~14°C. On day 20, however, the baseline value of the *Teffk*-signal suddenly jumps to ~17°C while the baseline value of the *Tefft*-signal begins to drift downwards. On day 27, the baseline value of the *Teffk*-signal suddenly returns to ~14°C, while that of the *Tefft*-signal stabilises at ~10°C. Of course, the *Teffk*- and *Tefft*-signals are estimates of the same physical quantity and the fact that they disagree after day 20 suggests that at least one of them is wrong. Examination of the instrument after recovery suggested that the accuracy of the type-T thermocouple had become compromised by leakage (A. Schultz, *pers. comm.*, 2000), and accordingly the *Teffk*-signal is regarded as representing the 'truth'. Schultz *et al.* (1996) note that the 7-day excursion in the *Teffk*-signal correlates with local drilling activity by the Ocean Drilling Program. The close-up views of the *Teffk*- and *Tefft*-signals (Figures 4.11g,h) reveal the semi-diurnal periodicity of the effluent temperature.

4.7.1.4 Medusa measurements – non-parametric analysis

Power spectra for the *Th*-, *Teffk*- and *v*-signals are shown in Figure 4.12. All power spectra were obtained from the low-pass filtered (15 min sampling interval) time-series using the MWPS code. The *Th*- and *Teffk*-signals each consisted of N=10,000 datapoints (104 days), and the shorter *v*-signal had N=384 datapoints (4 days), taken from the beginning of the time-period (Figure 4.11f). The power spectra for the *Th*- and *Teffk*-signals were calculated using

a time-bandwidth product of 5, with 10 eigenspectra and a 96-point (= 24 h) autoregressive prewhitening filter. The power spectrum for the *v*-signal was calculated using a time-bandwidth product of 1, with 2 eigenspectra and a 96-point (=24 h) autoregressive prewhitening filter. The small time-bandwidth product was required in order to get reasonable frequency resolution, but means that the variance of the power spectrum for the *v*-signal is relatively large, and the spectrum should therefore be interpreted with caution.

Figures 4.12a and 4.12b show the estimated power spectrum of the *Th*-signal. The general trend of the spectrum, shown in Figure 4.8a seems to be of the form $\hat{S}(f) \sim f^{-1}$, which is inconsistent with the $f^{-5/3}$ spectrum predicted by the Kolmogorov hypothesis (Section 4.2.5). A close-up view of the spectrum (Figure 4.12b) shows that a single significant line component was found at 3.867 ± 0.004 cpd. This line component can be identified with the 2nd harmonic of the *M2* tidal component (3.864 cpd). At the chosen significance level, no line components were identified in the diurnal or semi-diurnal bands. However there is a spectral peak between 1.9 and 2.0 cpd which can be identified with the *M2* (1.932 cpd) and *S2* (2.000 cpd) components. In the diurnal band, there is a broad concentration of spectral power with two peaks. The first peak lies between 0.80 cpd and 0.95 cpd. It can be identified with the *O1* tidal component (0.930 cpd). The second peak lies between 1.0 and 1.1 cpd, and can be identified with the *K1* tidal component (1.00 cpd). Taken together, these spectral peaks represent very strong evidence of the presence of a tidal signal in the *Th*-signal.

The power spectrum of the *Tefffk*-signal reveals no evidence of any line components, and has a general trend $\hat{S}(f) \sim f^{-0.53}$ (Figures 4.12c,d). The close-up view (Figure 4.12d) shows a large number of spectral peaks, none of which is particularly pronounced. Nonetheless, there is a reasonably strong peak in the semi-diurnal band between 1.9 cpd and 2.0 cpd, and another peak in the diurnal band between 0.94 cpd and 1.13 cpd. Together, these peaks represent fairly strong evidence of tidal modulation of effluent temperature.

The power spectrum of the *v*-signal (Figures 4.12e,f) is of limited use because of the short length of the original time-series. Nonetheless, it is interesting that there appear to be vague spectral peaks at around 1 cpd and 2 cpd, which constitute weak evidence of tidal modulation. There appears to be more spectral power in the diurnal band than the semi-diurnal band. This is consistent with the assertion of Schultz *et al.* (1996) that the *v*-signal is predominantly diurnal.

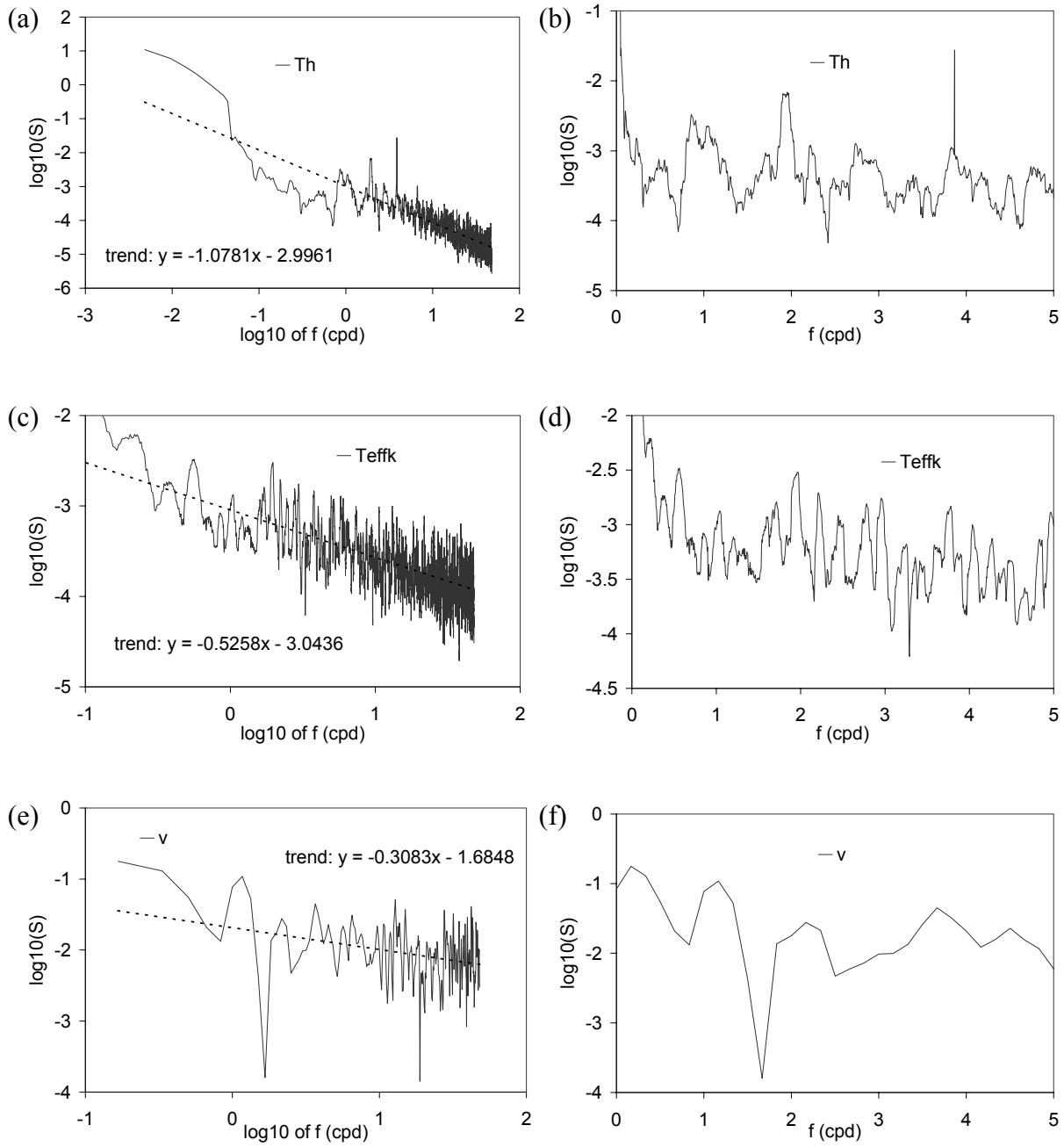

Figure 4.12: Spectral estimates for Medusa collected at the TAG site (26.13ºN, 44.82ºW) calculated using the MWPS code. *Th* – ambient (thermistor) temperature, *Teffk* – effluent temperature, *v* – effluent velocity.

4.7.1.5 Medusa measurements – parametric analysis

The spectral estimates of the previous section provide evidence of tidal modulation in the *Th*-, *Teffk*-, *Tefft*- and *v*-signals. Accordingly, estimates of the Admiralty Method harmonic

constants have been made for each of these signals. These estimates are compared with the harmonic constants for the local tidal potential and ocean tide in Table 4.5 and Figure 4.13.

TAG	H_1 (*M2A*)	g_1 (*M2A*)	H_2 (*S2A*)	g_2 (*S2A*)	H_3 (*K1A*)	g_3 (*K1A*)	H_4 (*O1A*)	g_4 (*O1A*)
potential ($m^2.s^{-2}$)	2.28	88°	1.06	89°	1.23	45°	0.90	45°
ocean (m)	0.15	326°	0.07	1°	0.01	190°	0.03	228°
Th (°C)	0.139	233°	0.094	273°	0.087	71°	0.042	101°
Teffk (°C)	0.156	192°	0.074	256°	0.059	67°	0.005	75°
Tefft (°C)	0.159	191°	0.102	245°	0.035	135°	0.018	237°
v (raw counts)	2.238	175°	2.018	70°	7.244	140°	4.25	18°
shrimp (pixels)	747	245°	2166	335°	2320	182°	1097	357°

TAG	$(H_1+H_2)/(H_3+H_4)$	H_1/H_2	g_2-g_1	H_3/H_4	g_4-g_3
tidal potential	1.57	2.15	< 1°	1.37	< 1°
ocean tide	5.5	2.14	35°	0.33	38°
Th	1.81	1.49	39°	2.11	30°
Teffk	3.65	2.10	64°	12.9	8°
Tefft	4.98	1.56	54°	1.98	102°
v	0.37	1.11	-104°	1.70	-122°
shrimp density	0.85	0.34	90°	2.11	175°

Table 4.5: The Admiralty Method harmonic constants of the tidal potential, ocean tide, Medusa data and shrimp density data at the TAG site estimated using the HYBRID code.

The temperature time-series (*Th*, *Tefffk*, and *Tefft*) each consisted of N=10,000 data points at a sampling interval Δt=15 min. Attempts to extract harmonic constants from the entire time-series using the Bayesian drift technique proved unsuccessful, presumably because the time-series do not conform sufficiently closely to the functional form assumed in Section 3.3.3. Consequently, the harmonic constants reported here were estimated by section averaging, using the HYBRID code, in the manner described in Section 4.5.1. In this case, the temperature time-series were split into 47 overlapping sections of 672 points (= 7 days), giving a 30% offset between sections. The estimated harmonic constants for the *Th*-signal can be compared with those for the tidal potential and the ocean tide (Table 4.5). At TAG, the ocean tide is strongly semi-diurnal, with $(H_1+H_2)/(H_3+H_4)$=5.5, while the tidal potential is more mixed, with $(H_1+H_2)/(H_3+H_4)$=1.57. Thus, the value obtained for the *Th*-signal ($(H_1+H_2)/(H_3+H_4)$=1.81) is more compatible with the tidal potential than with the ocean tide. However, this value should be treated with caution as there is considerable uncertainty in the diurnal harmonic constants (Figure 4.13f).

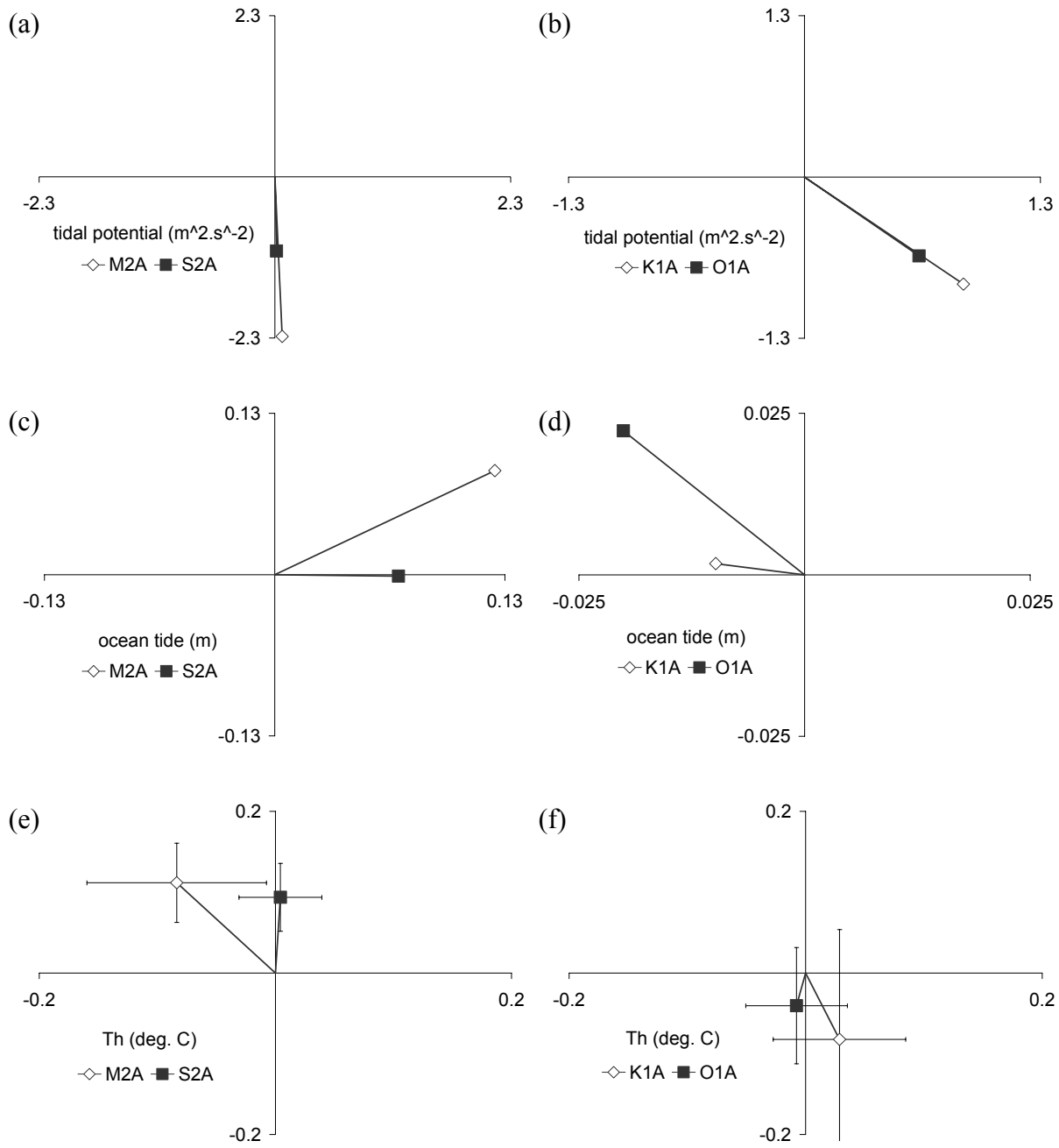

Figure 4.13: Admiralty Method harmonic constants for the TAG site (26.13ºN, 44.82ºW) estimated using the HYBRID code. Tidal potential predicted by ETGTAB code, ocean tide predicted by CSR code. *Th* – ambient (thermistor) temperature.

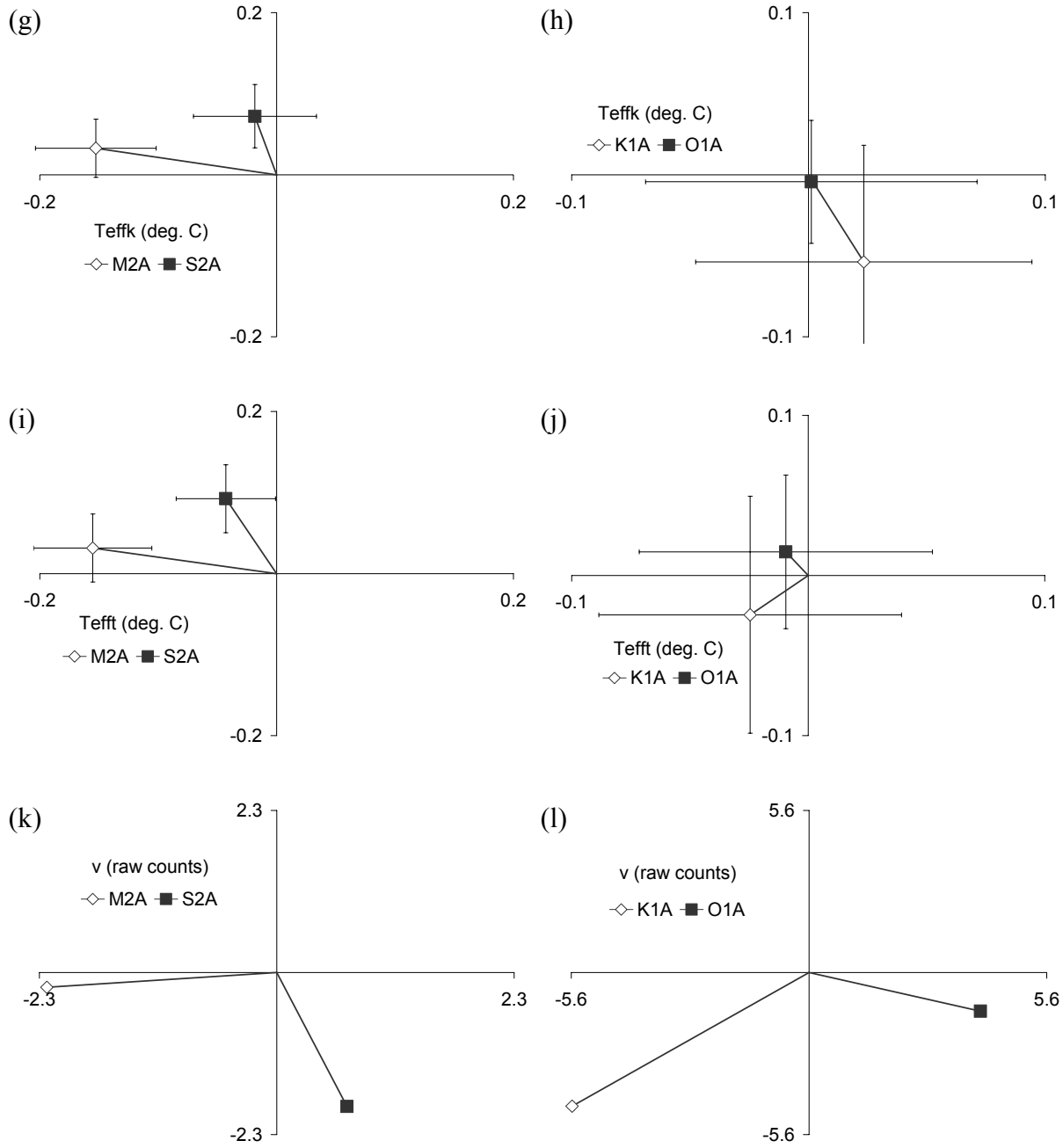

Figure 4.13: (continued) Admiralty Method harmonic constants for the Medusa data at the TAG site (26.13ºN, 44.82ºW) estimated using the HYBRID code. *Teffk*, *Tefft* – effluent temperature. *v* – effluent velocity.

The relative magnitude of the semi-diurnal components is (H_1/H_2)=1.49 for the *Th*-signal, while (H_1/H_2)=2.15 for the tidal potential, and (H_1/H_2)=2.14 for the ocean tide. Therefore the value for the *Th*-signal is equally compatible with both tidal inputs. However, the difference in phase lag of the semi-diurnal components is more diagnostic. The phase difference $(g_2–g_1)$ is negligible for the tidal potential, but $(g_2–g_1)$=35° for the ocean tide and $(g_2–g_1)$=39° for the *Th*-signal. This provides evidence of a correlation between the ocean tide and the *Th*-signal

in the semi-diurnal band, with the *Th*-signal lagging the ocean tide by approximately 270°. In general, therefore, high ambient temperatures occur on the rising half tide. It should be noted, however, that this phase lag does not apply for the entire observation period. For example in the early part of the record (Figure 4.11e), the phase lag between the ocean tide and the *Th*-signal is close to 0°. No inferences are drawn from the diurnal harmonic constants because of the large uncertainties in the estimates (Figure 4.13f).

The estimated harmonic constants for the *Teffk*-signal (Figure 4.13g,h) and the *Tefft*-signal (Figure 4.13i,j) are broadly similar. Since the harmonic constants were derived from section averaging of the entire data record, this is evidence that the tidal parts of the two signals remained similar even after the offset which occurred at day 20 (Figure 4.11c,d). Both signals are dominated by semi-diurnal components, in common with the ocean tide. Table 4.5 shows that the *M2A* components of the effluent temperature signals lag the *M2A* component of the ocean tide by 225° and 226°. In other words high effluent temperatures occur between low tide and rising half-tide. It should be noted that this phase lag is compatible with the theoretical prediction of Section 6.3.1.3. No inferences are drawn from the diurnal harmonic constants because of the large uncertainties in the estimates (Figure 4.13h,j).

The estimation of harmonic constants for the *v*-signal is complicated by the fact that only a very short (384 points, or 4 days) section of data is suitable for analysis (Figure 4.11b). Section-averaging methods are inappropriate for such a short time-series, so this data section was analysed using the HYBRID code with Bayesian drift removal. The results of the analysis are given in Table 4.5 and Figure 4.13k,l. As there is no section averaging, no error bars can be included in the figures. It must be stressed that there is, nonetheless, considerable uncertainty in the estimates. The lack of error bars simply indicates that there is no numerical estimate of this uncertainty. The results suggest that the *v*-signal is dominated by diurnal components. This finding is compatible with the analysis of Schultz *et al.* (1996), which was based on a Harmonic Method decomposition.

The results of the Bayesian drift removal for the *v*-signal are shown in the time-domain in Figure 4.14. Figure 4.14a shows that the algorithm extracts a plausibly smooth drift component. However, it is less clear that the extracted tidal signal (labelled *tide*) constitutes a good representation of the original data. Figure 4.14b shows that this '*tide*' signal has less

than half the amplitude of the residual '*error*' signal. The local ocean tide for the same time period is also shown, for comparison. The ocean tide is strongly semi-diurnal, while the inferred tidal part of the *v*-signal is dominantly diurnal.

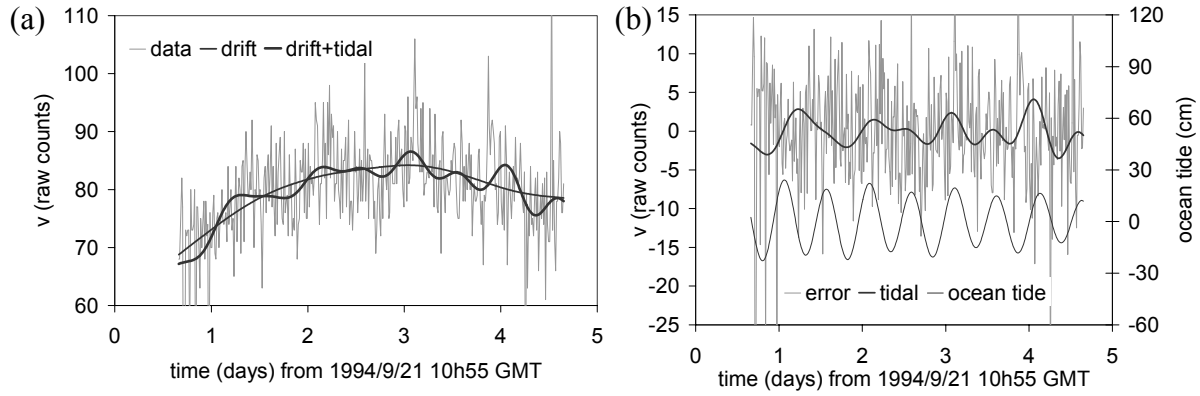

Figure 4.14: The extraction of a tidal signal from the *v*-channel of Medusa at TAG (Schultz *et al.*, 1996), using the HYBRID code with Bayesian drift removal. The data signal is decomposed into *drift*, *tidal* and residual *error*. (a) The original data series (*data*), compared with the *drift* signal and the best-fitting *drift* + *tidal* signal. (b) The tidal part of the *v*-signal (*tidal* – generated by the extracted harmonic constants) compared with the *error*. For comparison, the ocean tide at TAG for the same period is shown on a separate scale.

4.7.1.6 Manatee and OBSH measurements

Fujioka *et al.* (1997) report several time-series obtained at TAG between 1994/8/5 and 1994/8/21. Firstly, several time-series were recorded using a 'Manatee' instrument which was moored 45 m east of the CBC at a height of 2 m above the seafloor. The Manatee is equipped with a current meter, a temperature sensor and a light transmission meter. Secondly, a hydrophone time-series was recorded using an OBSH instrument (Sato *et al.,* 1995) located 30 m east of the CBC.

Fujioka *et al.* (1997) report that the near-bottom current at TAG typically has a magnitude of 0.1 $m.s^{-1}$, which varies only slightly with a semi-diurnal period. Their data show that the direction of this current oscillated with a clear semi-diurnal period between 1994/8/5 and 1994/8/14, but that this oscillation became less regular after 1994/8/14. They note that 'the

former period is co-incident with the flood tide and the latter with the ebb tide'. This cannot be true, since a 'flood' tide is a period of rising sea level and an 'ebb' tide is a period of falling sea level (Manual of Tidal Prediction, 1958). However, it is true that there was a quarter moon on 1994/8/14, which gave rise to neap tides (Yallop & Hohenkerk, 1990). In the presence of a strong background flow, it is possible that tidal streams would be sufficient to reverse the current direction during spring tides, but not during neap tides. It is therefore suggested that Fujioka *et al.* (1997) refer erroneously to 'flood' and 'ebb' tides, instead of 'spring' and 'neap' tides.

The temperature time-series recorded by Manatee shows an ambient temperature of ~2.7°C, interrupted by brief 'spikes' where the temperature rises by ~1°C. These 'spikes' occur with semi-diurnal frequency in the early part of the record (during spring tides), and with erratic frequency in the latter part (during neap tides). Fujioka *et al.* (1997) note that the high temperature spikes do not show a clear pattern of correlation with current direction, and conclude that the temperature variations are due to a combination of changes in currents and hydrothermal venting activity.

The time-series of turbidity displays a similar pattern to the temperature. 'Spikes' of high turbidity (caused by effluent particles suspended in the water) occur with semi-diurnal periodicity in the early part of the record during spring tides. Fujioka *et al.* (1997) note that high turbidity does not always correlate with elevated temperatures. However, on most of the occasions where turbidity and temperature maxima were simultaneous, the current was from south-southeast. The authors note that an active vent was located south-southeast of their Manatee instrument, and suggest that many of the temperature and turbidity anomalies can be attributed to the advection of effluent from this vent.

In summary, the Manatee data suggest that hydrothermal effluent is advected along the ocean floor by the prevailing currents. These currents are strongly influenced by tidal streams, and so contain significant power at the tidal frequencies. However, it appears that these currents are far from being pure tidal streams and contain significant contributions from non-tidal processes. Consequently, any process which depends on the seafloor currents at TAG is likely to exhibit similar behaviour, and have the appearance of a noisy tidal signal.

The pressure pulses recorded by the OBSH hydrophone at TAG (Fujioka *et al.,* 1997), show a similar pattern to those recorded in the Mariana Trough (Sato *et al.,* 1995; Section 4.6), in that their frequency of occurrence varies with a semi-diurnal period. These pressure pulses are interpreted as being due to the periodic upwelling of hot vent fluid. The difference lies in the phase relationship between the local ocean tide and pressure-pulse activity. At the Mariana Trough, pressure-pulse activity was highest at high tide. At TAG, pressure pulse activity seems to peak between falling half-tide and low tide. In other words the TAG OBSH data suggest that the frequency of hydrothermal upwelling events lags the ocean tide by a phase angle in the range [90°, 180°].

4.7.1.7 'Shrimp density' measurements

Copley *et al.* (1999) used a time-lapse video technique to measure the density of shrimp on a section of the TAG hydrothermal mound. The field of view of the camera was static, encompassing ~1.5 m^2 of the mound's surface. At six-hourly intervals, the camera recorded a 15-second segment of video. A single frame was then chosen for image analysis from each of these video segments. The number of pixels in the frame occupied by shrimp was used as a measure of the density of shrimp on the mound. In this way a time-series of 'shrimp density' was constructed with a sampling interval of 6 h. The measurements cover a period of 26 days from 1994/9/21 23h00 GMT. Copley *et al.* (1999) performed a spectral analysis of this time-series using the unwindowed periodogram estimator. The resulting spectrum contains strong peaks covering the diurnal and semi-diurnal frequency bands, and suggests that 'shrimp density' is tidally modulated.

The section of the 'shrimp density' time-series showing the clearest semi-diurnal periodicity is reproduced in Figure 4.15. An attempt was made to find the best-fitting set of Admiralty Method harmonic constants for this section of data using the HYBRID code. Initially, the 15 datapoints of Figure 4.15 were input to the HYBRID code with no modification except subtraction of the mean. The resulting harmonic constants were clearly unrealistic because of their extremely large magnitudes. Strictly, however, they were correct because they generated a time-series which was the best-fit for the data, in a least-squares sense. The problem arose because an attempt was made to fit a parametric function whose fundamental period is 12 h onto a dataset with a 6-h sampling interval. A partial solution is to introduce a fictitious data point before attempting to extract the harmonic constants. Accordingly, 14 separate estimates of each harmonic constant were made. Each of the 14 estimates was made after inserting a fictitious data point, by linear interpolation, halfway between an adjacent

pair of the original data points. A final estimate for each (complex) harmonic constant was then made by taking the mean value of the 14 separate estimates. The harmonic constants estimated in this way are listed in Table 4.5, and were used to create the tidal time-series shown in Figure 4.15.

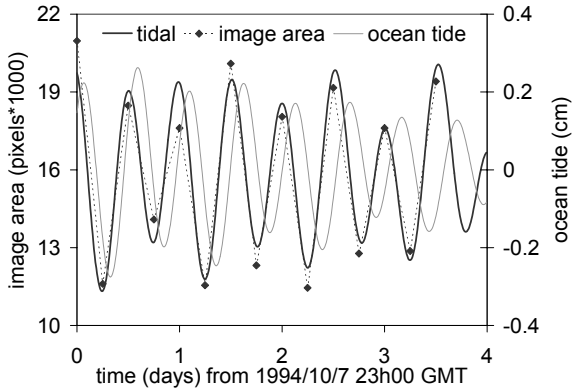

Figure 4.15: A section of the 'shrimp density' time-series collected by Copley *et al.* (1999) at the TAG site. The data points ('image area') record the number of pixels of video frame occupied by shrimp. The data have been fitted with a tidal signal ('tidal') generated by the Admiralty Method harmonic constants given in Table 4.5. The local ocean tide is also reproduced, for comparison.

The original sampling interval of exactly 6 h, coupled with the insertion of fictitious data points based on linear interpolation, probably caused too much power to be attributed to the *S2A* component. (The related *S2* component has a period of exactly 12 h.) Consequently, the harmonic constants extracted here should be regarded as very poorly constrained. Nonetheless, the low quality of the estimate is a useful reminder of the problems inherent in fitting a parametric model to a scant dataset.

Figure 4.15 and Table 4.5 allow the 'shrimp density' to be compared with the local ocean tide. For the *M2A* component, the shrimp density lags the ocean tide by 279°, while for the *S2A* component the phase lag is 334°. It follows that shrimp density is highest at rising half-tide. Since the ambient temperature is also generally greatest on the rising half-tide it can be speculated that the shrimp density is greatest when the ambient temperature is greatest.

4.7.1.8 Summary of tidal modulation observed at TAG

The results of the preceding sections can now be summarised to give an overview of tidal modulation at the TAG hydrothermal mound. The data of Kinoshita *et al.* (1996, 1998) suggest that tidal oscillations in sub-bottom temperatures lag the ocean tide by 90°, while the data of Fujioka *et al.* (1997) suggest that the frequency of episodic venting events lags the ocean tide by an angle between 90° and 180°.

Non-parametric analysis of Medusa data reveals strong evidence of tidal modulation of the ambient (*Th*) and effluent (*Teffk*, *Tefft*) temperatures and weaker evidence of tidal modulation of the effluent velocity (*v*). Parametric analysis using the Admiralty Method suggests that the velocity signal is dominantly diurnal, while the temperature signals are predominantly semi-diurnal. This is consistent with results of Schultz *et al.* (1996) which are based on a Harmonic Method decomposition. The phase lags for the dominant semi-diurnal components in Table 4.5 shows that the *Th*-signal generally lags the ocean tide by 267°. However, there are times during the observation period when the phase lag is close to 0° (Figure 4.11e). This drift in phase lag is probably caused by a change in the properties of the TAG mound and may be due to the ODP drilling which occurred during the observation period. The *M2A* components of the effluent temperature (*Teffk*, *Tefft*) lag the *M2A* component of the ocean tide by 225° and 226°. These phase lags are consistent with the model presented in Section 6.3.1.3.

The density of shrimp observed on a section of the seafloor exhibits tidal modulation (Copley *et al.,* 1999) and is shown to lag the ocean tide by a phase angle of 279° for the *M2A* component and 334° for the *S2A* component. Consequently, high shrimp density occurs at the same phase of the ocean tide as high ambient temperatures.

4.7.2 The Menez Gwen Site

In 1997, time-series data were collected using a Medusa system at the Menez Gwen site (37.83°N, 31.50°W) on the Mid-Atlantic Ridge (A. Schultz, *pers. comm.*, 1997). Time-series of ambient temperature (*Th*), effluent temperature (*Tefft*) and effluent velocity (*v*) were obtained over a period of 11 days from 1997/7/26. In addition, the Medusa sample bottles were used to collect six samples of hydrothermal effluent at a sampling interval of 6 h for later chemical analysis (Cooper, 1999; Cooper *et al.,* 2000).

4.7.2.1 Medusa measurements – time-domain

The data collected by Medusa at the Menez Gwen site are shown in the time-domain in Figure 4.16. The original time-series measurements of velocity and temperature (sampling interval 15 s) have been low-pass filtered with a moving median filter of length 60 to produce time-series with a sampling interval of 15 min (Schultz *et al.,* 1992).

There is some evidence of semi-diurnal periodicity in the overview of the *Th*-signal (Figure 4.16a). This semi-diurnal signal seems strongest in the 2-day period shown in Figure 4.16d, where it appears that the *Th*-signal lags the ocean tide by ~90°, giving the highest ambient temperatures during the falling half-tide. It must be stressed, however, that the time-series is too noisy for any strong inference to be made.

The time-domain view of the *Tefft*-signal provides weak evidence of tidal modulation (Figure 4.16b,e), and the velocity sensor seems to have operated sporadically during the first 3 days of deployment, before failing to record any more data (Figure 4.16c). There is a noticeable downward trend in the *v*-signal which is consistent with a gradual increase in friction slowing down the propeller of the velocity sensor. There is very little evidence of tidal modulation in the time-domain view of the *v*-signal.

Chemical analysis of the six effluent samples shows that they are consistent with a 'mixing' model for diffuse flow (Cooper, 1998: Cooper *et al.,* 2000). According to this model, the diffuse flow passing through Medusa is a mixture of high temperature (~280°C) hydrothermal fluid and cool seawater. The chemical composition of each sample can then be used to calculate the relative proportions of high-temperature fluid and seawater which it contains. The percentage of high temperature (*HT*) fluid in the effluent is graphed against time of sample collection in Figures 4.16f,g.

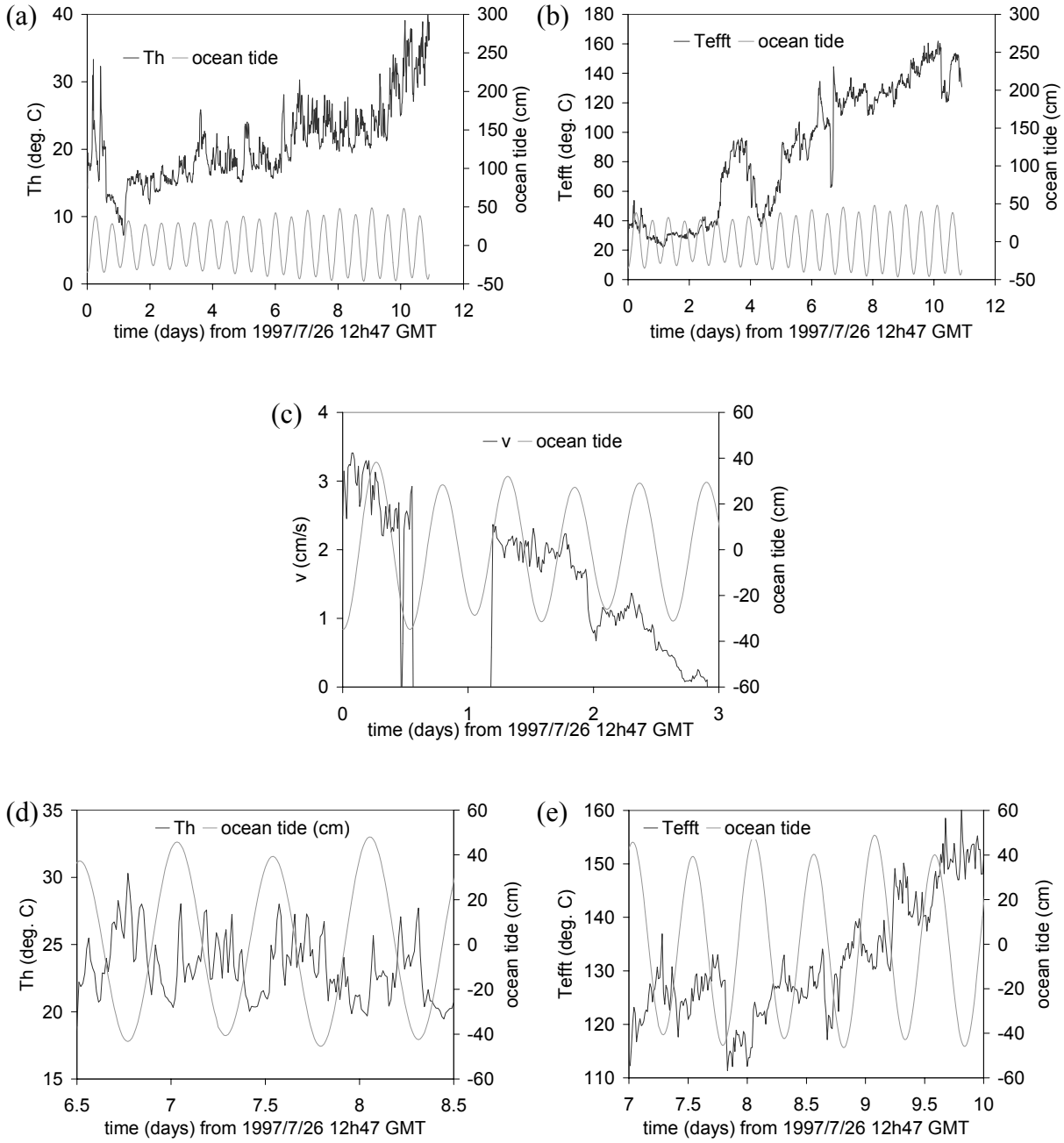

Figure 4.16: Data collected by Medusa at the Menez Gwen site (37.83°N, 31.50°W) on the Mid-Atlantic Ridge. *Th* – ambient (thermistor) temperature, *Tefft* – effluent temperature, *v* – effluent velocity.

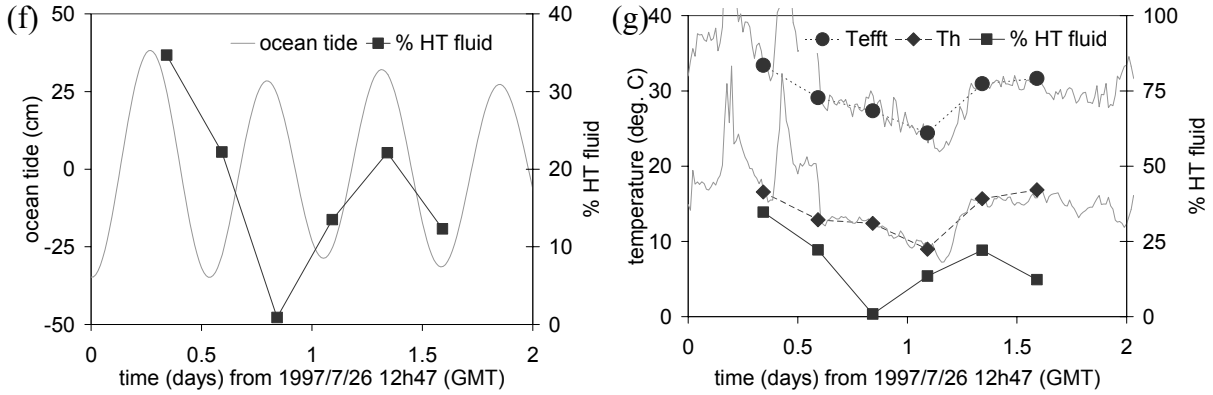

Figure 4.16: (continued) Data collected by Medusa at the Menez Gwen site (37.83°N, 31.50°W) on the Mid-Atlantic Ridge. *Th* – ambient (thermistor) temperature, *Tefft* – effluent temperature, *v* – effluent velocity.

Figure 4.16f shows that the chemical composition of the effluent displays a diurnal periodicity, with no obvious relationship to the semi-diurnal ocean tide. Figure 4.16g compares the inferred effluent composition with the ambient (*Th*) and effluent (*Tefft*) temperatures. The values of the temperatures at the times when the chemical samples were taken are highlighted in the figure. The *Th*- and *Tefft*-signals display similar changes over this period, despite the offset of ~10°C between them. This suggests that the same physical mechanism modulates ambient and effluent temperatures. It is possible to argue from Figure 4.16g that the effluent composition and the temperature channels display roughly similar changes over time, but the sparse data mean that this assertion cannot be made with confidence. However, it is equally true that there is no strong evidence for a *lack* of correlation between effluent temperature and composition in these data.

4.7.2.2 Medusa measurements – non-parametric analysis

The short time-series mean that it would be unjustified to attempt spectral analyses of the *v*-signal or the chemical data obtained by Medusa at Menez Gwen (Figure 4.16c,f). However, power spectra for the *Th*- and *Tefft*-signals, obtained using the MWPS code, are shown in Figure 4.17. The *Th*- and *Tefft*-signals each consist of N=1,047 datapoints (11 days) at a sampling interval of Δt=15 minutes. The power spectra were calculated using a time-bandwidth product of 2, 4 eigenspectra, and with a 96-point (= 24 h) autoregressive prewhitening filter.

Figures 4.17a and 4.17b show the estimated power spectrum of the *Th*-signal. The general trend of the spectrum takes the form $\hat{S}(f) \sim f^{-1.6}$. This is roughly consistent with the Kolmogorov hypothesis of Section 4.2.5, and hence with a model in which ambient temperature is modulated by a turbulent process. No significant spectral lines were detected for the *Th*-signal but there is evidence of broad peaks of spectral power around the semi-diurnal and quarter-diurnal frequency bands.

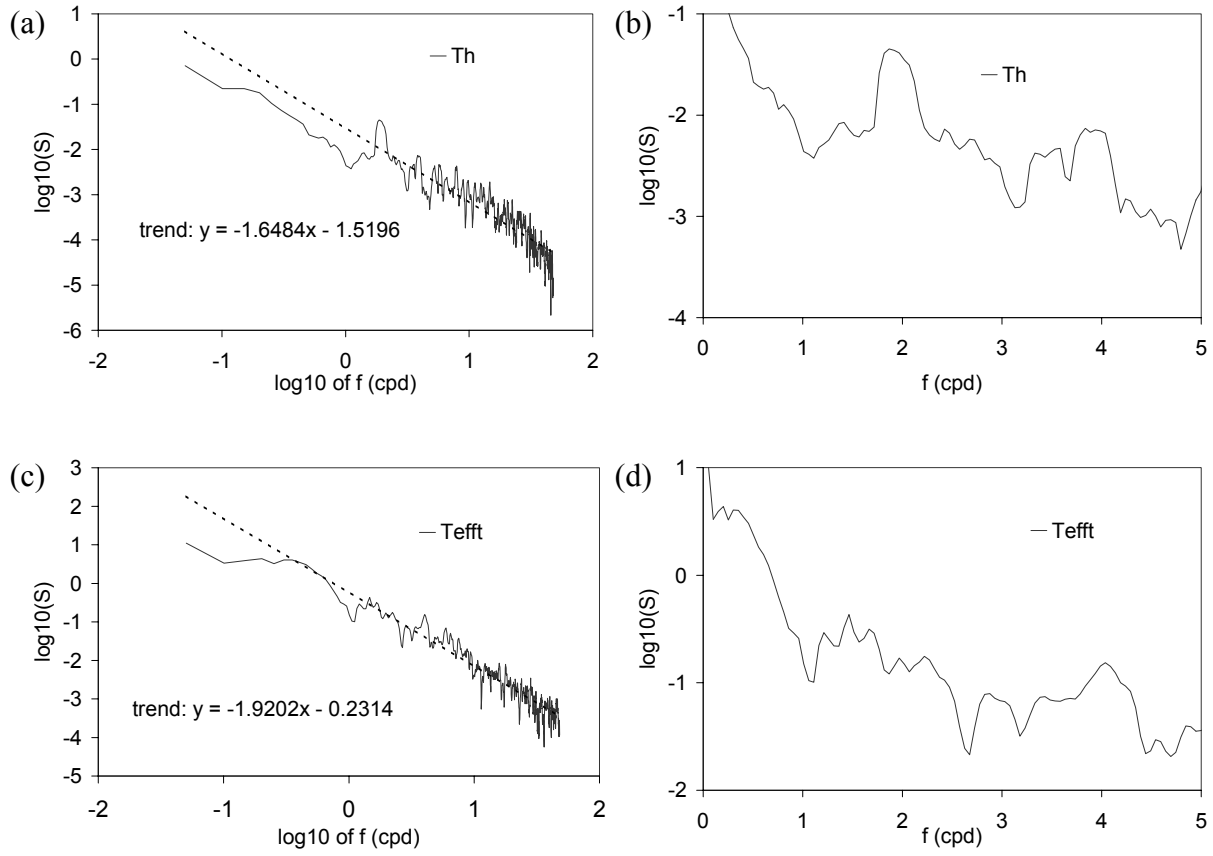

Figure 4.17: Spectral estimates for Medusa data collected at the Menez Gwen site (37.83°N, 31.50°W), calculated using the MWPS code. *Th* – ambient (thermistor) temperature, *Tefft* – effluent temperature.

In contrast, there is no evidence of power at tidal frequencies in the power spectrum of the *Tefft*-signal (Figures 4.17c,d), which has a general trend of the form $\hat{S}(f) \sim f^{-1.9}$.

Neither of these spectral estimates shows strong evidence of tidal modulation. Consequently, no attempt has been made to estimate Admiralty Method harmonic constants for these time-series.

4.7.3 The Lucky Strike site

Between 1997 and 1998, time-series data were collected using a Medusa system at the Lucky Strike site (37.28°N, 32.33°W) on the Mid-Atlantic Ridge (A. Schultz, *pers. comm.*, 1998). Time-series of ambient and effluent temperature were obtained over a period of 240 days from 1997/8/29. It had also been intended to obtain time-series of effluent velocity and composition, but these were not recovered successfully.

The Lucky Strike site is unique amongst the Medusa locations considered in this dissertation because horizontal current measurements for the site are available. A current meter and a temperature sensor were installed on a long-term mooring 20 m above the seafloor. Temperature and current measurements were made at hourly intervals over a period of 408 days from 1994/6/2 (A. Vangriesheim, *pers. comm.*, 1998).

4.7.3.1 Medusa measurements – time-domain

The data collected by Medusa at the Lucky Strike site are shown in the time-domain in Figure 4.18. The original time-series measurements of effluent velocity, effluent temperature and ambient temperature (sampling interval 15 s) have been low-pass filtered with a moving median filter of length 60 to produce time-series with a sampling interval of 15 min (Schultz *et al.,* 1992).

There is clear evidence of tidal modulation in the *Th*-signal (Figure 4.18a,c). A striking feature of the overview (Figure 4.18a) is the presence of an apparent springs/neaps cycle in the *Th*-signal which corresponds with the springs/neaps cycle of the ocean tide. There is clear evidence of semi-diurnal periodicity in the close-up view of Figure 4.18c, where it appears that the *Th*-signal is out of phase with the ocean tide. However, there is less evidence of semi-diurnal periodicity during the period shown in Figure 4.18e. Thus, while the *Th*-signal shows clear evidence of tidal modulation overall, there are times when non-tidal processes dominate the record. The *Tefft*-signal also exhibits semi-diurnal periodicity (Figure 4.18f), but it displays less evidence of a springs/neaps cycle than the *Th*-signal, and has a distinctly non-stationary appearance (Figure 4.18b). This non-stationarity is apparent in the sudden offsets in the record (e.g. at around day 200), and the changing amplitude of the semi-diurnal variations.

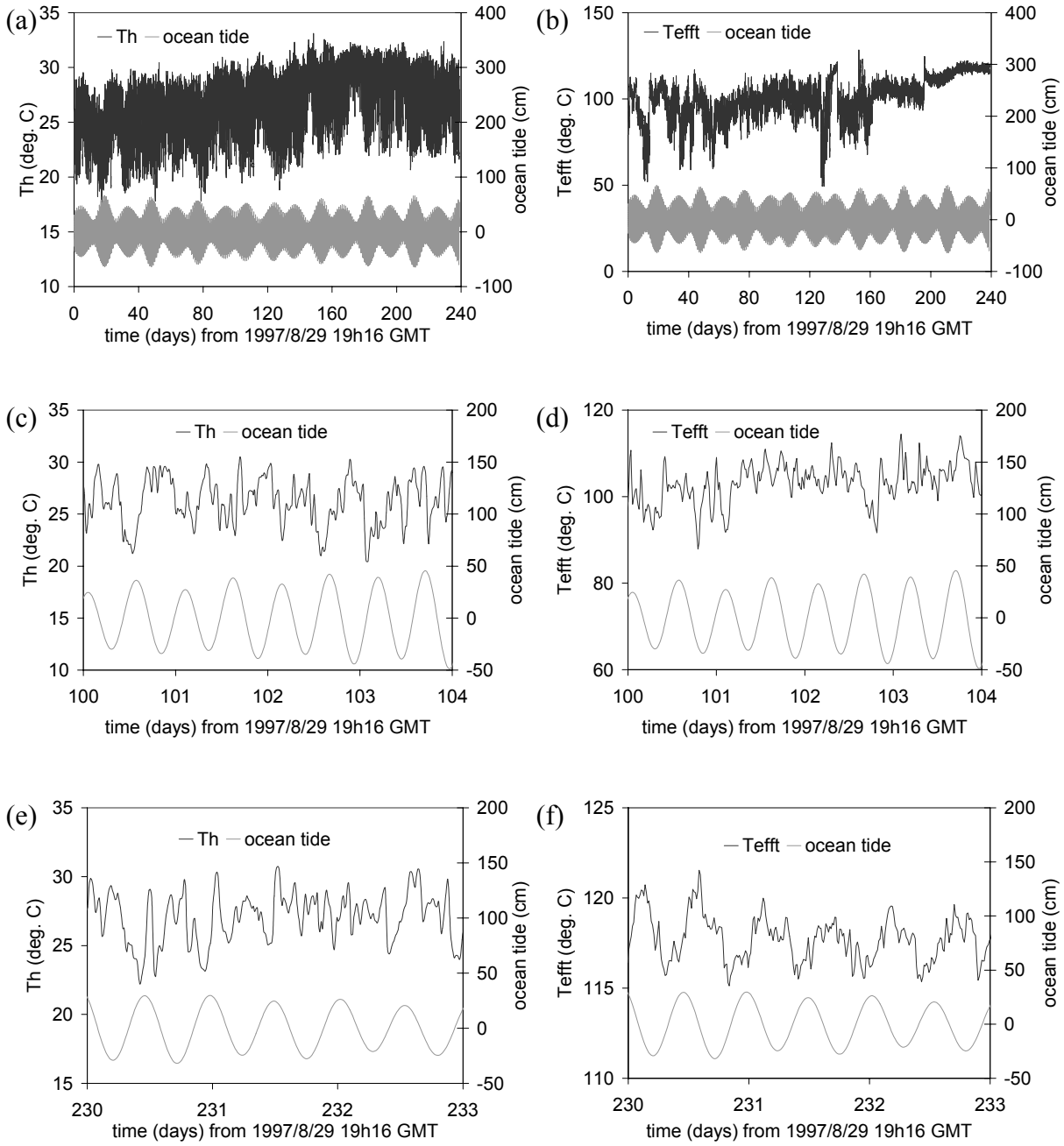

Figure 4.18: Temperature data collected by Medusa at the Lucky Strike site (37.28°N, 32.33°W) on the Mid-Atlantic Ridge. *Th* – ambient (thermistor) temperature. *Tefft* – effluent temperature.

In common with the *Th*-signal, there are times when the semi-diurnal periodicity of the *Tefft*-signal is very clear (Figure 4.18f), and times when it appears to have been swamped by other processes (Figure 4.18d). However, the *Th*- and *Tefft*-signals do not necessarily display strong tidal modulation at the same time. For example, the period between day 230 and day 233 is a time of strong tidal modulation of the *Tefft*-signal, but weak tidal modulation of the

Th-signal (Figure 4.18e,f). From the time-domain graph (Figure 4.18f), the *Tefft*-signal appears to be approximately out of phase with the ocean tide.

4.7.3.2 Medusa measurements – non-parametric analysis

Estimated power spectra for the *Th*- and *Tefft*-signals, obtained using the MWPS code, are shown in Figure 4.19. The power spectra were calculated from the low-pass filtered (15 min sampling interval) time-series which consist of N=22,931 datapoints (239 days). Accordingly, the power spectra were calculated using a time-bandwidth product of 10, using 20 eigenspectra and a 96-point (= 24 h) autoregressive prewhitening filter.

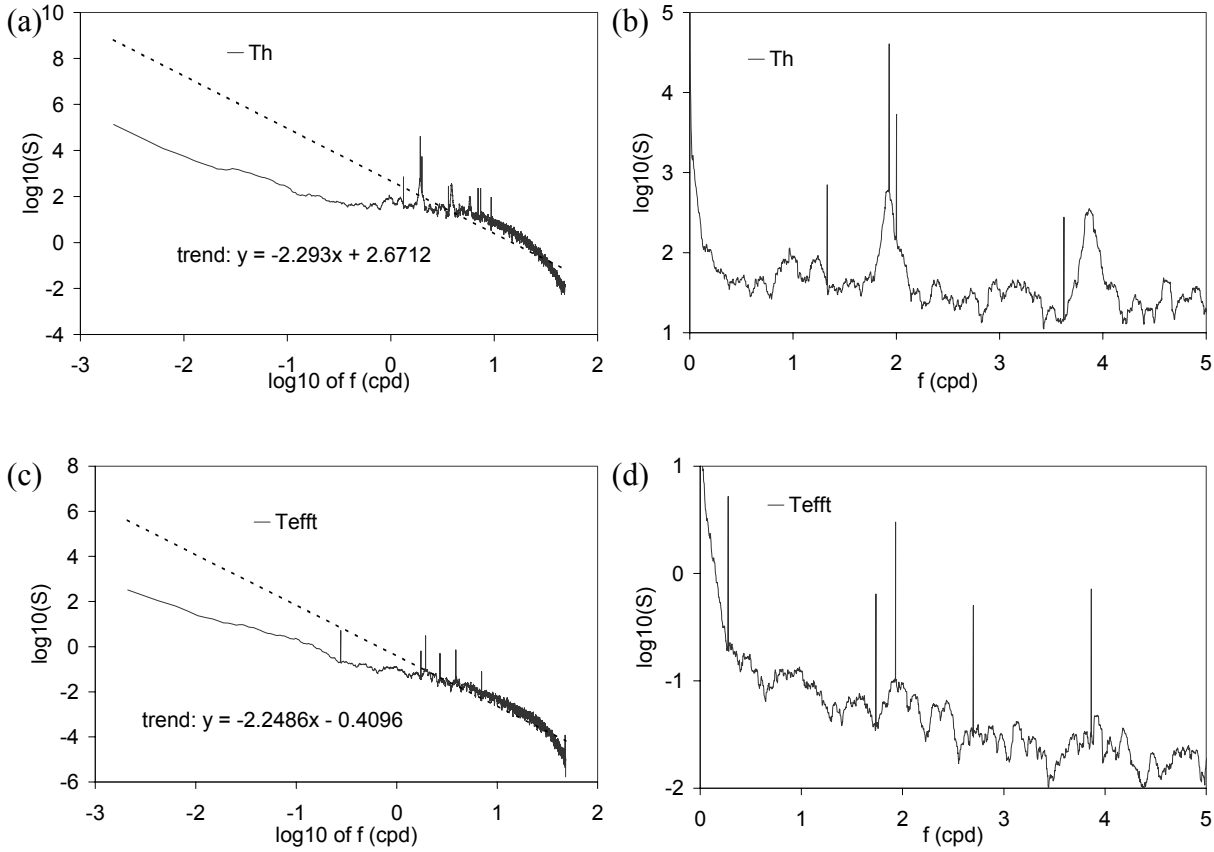

Figure 4.19: Spectral estimates for Medusa data collected at the Lucky Strike site (37.28°N, 32.33°W), calculated using the MWPS code. *Th* – ambient (thermistor) temperature, *Tefft* – effluent temperature.

The estimated power spectrum of the *Th*-signal has a general trend of the form $\hat{S}(f) \sim f^{-2.3}$, although the decay becomes steeper at the highest frequencies (Figure 4.19a). The close-up

view of the spectrum (Figure 4.19b) reveals that several significant line components were detected (Table 4.6).

Low frequency line components – *Th*-signal at Lucky Strike		
frequency of observed line (cpd)	frequency of associated tidal component (cpd)	name of associated tidal component
1.331 ± 0.002		
1.932 ± 0.002	1.932	*M2*
2.001 ± 0.002	2.000	*S2*
3.622 ± 0.002		

Table 4.6: Significant line components identified in the *Th*-signal at Lucky Strike.

The lowest frequency line appears at 1.331 ± 0.002 cpd, and is not tidal in origin. However the lines at 1.932 ± 0.002 cpd and 2.001 ± 0.002 cpd can confidently be identified with the *M2* (1.932 cpd) and *S2* (2.000 cpd) tidal components. The line at 3.622 ± 0.002 cpd lies outside the range of quarter-diurnal frequencies associated with tidal processes, and is unlikely to be tidal in origin. However, there is a broad quarter-diurnal peak centered on 3.87 cpd which corresponds to the 2nd harmonic of the semi-diurnal tidal frequencies, and there is a small peak in the diurnal frequency band (Figure 4.19b). In summary the non-parametric analysis presents very strong evidence of tidal modulation of the *Th*-signal.

The estimated power spectrum of the *Tefft*-signal has a general trend of the form $\hat{S}(f) \sim f^{-2.2}$ (Figure 4.19c), and is broadly similar to the power spectrum of the *Th*-signal. The close-up view of the spectrum (Figure 4.19d) reveals that several significant line components were detected (Table 4.7).

Low frequency line components – *Tefft*-signal at Lucky Strike		
frequency of observed line (cpd)	frequency of associated tidal component (cpd)	name of associated tidal component
0.277 ± 0.002		
1.736 ± 0.002		
1.932 ± 0.002	1.932	*M2*
2.699 ± 0.002		
3.866 ± 0.002	3.865	2nd harmonic of *M2*

Table 4.7: Significant line components detected in the *Tefft*-signal at Lucky Strike.

Three of these lines cannot be tidal in origin because they do not occur at frequencies associated with the tidal potential. These lines occur at 0.277 ± 0.002 cpd, 1.736 ± 0.002 cpd

and 2.699 ± 0.002 cpd. However, the line at 1.932 ± 0.002 cpd corresponds to the *M2* component and the line at 3.866 ± 0.002 cpd corresponds to its 2nd harmonic.

In summary, the estimated power spectra (Figure 4.19) provide strong evidence that both the *Th*- and *Tefft*-signals are tidally modulated. The spectra are dominated by power in the semi-diurnal band and contain significant power in the quarter-diurnal band.

4.7.3.3 Medusa data – parametric description

The Admiralty Method harmonic constants for the *Th*- and *Tefft*-signals are estimated using the HYBRID code. These harmonic constants are compared with the harmonic constants of the local tidal potential and ocean tide in Table 4.8 and Figure 4.20.

An initial attempt was made to decompose the whole of the *Th*- and *Tefft*-signals using the Bayesian drift technique but better results were obtained using section averaging with mean removal. The original time-series (of N=22,931 points) were split into 112 overlapping sections of 672 points (= 7 days), giving a 30% offset between sections.

Using Table 4.8 and Figure 4.20, the harmonic constants of the *Th*-signal can be compared with those of the two postulated input signals (the tidal potential and the ocean tide). The relative magnitude of semi-diurnal to diurnal components $(H_1+H_2)/(H_3+H_4)$ is diagnostic as it differs greatly between the tidal potential and the ocean tide at this location. This ratio takes the value $(H_1+H_2)/(H_3+H_4)=0.998$ for the tidal potential, which indicates a mixed tide. The ocean tide, on the other hand, is strongly a semi-diurnal tide, with $(H_1+H_2)/(H_3+H_4)=9.4$. For the *Th*-signal, $(H_1+H_2)/(H_3+H_4)=3.99$ (Table 4.8). This is sufficiently large for the associated signal to appear semi-diurnal in the domain. Consequently, on the basis of the relative power in the diurnal and semi-diurnal band, it is concluded that the *Th*-signal is more similar to the ocean tide than the tidal potential (Figure 4.20a,c,e).

For example, the difference in phase lag, (g_2-g_1), is 21° for both the *Th*-signal and ocean tide, but it is less than 1° for the tidal potential. Thus, the semi-diurnal components of the *Th*-signal both lag the semi-diurnal components of the ocean tide by 172° (Table 4.8). This is consistent with the observation made in the time-domain that the *Th*-signal and the ocean tide are out of phase.

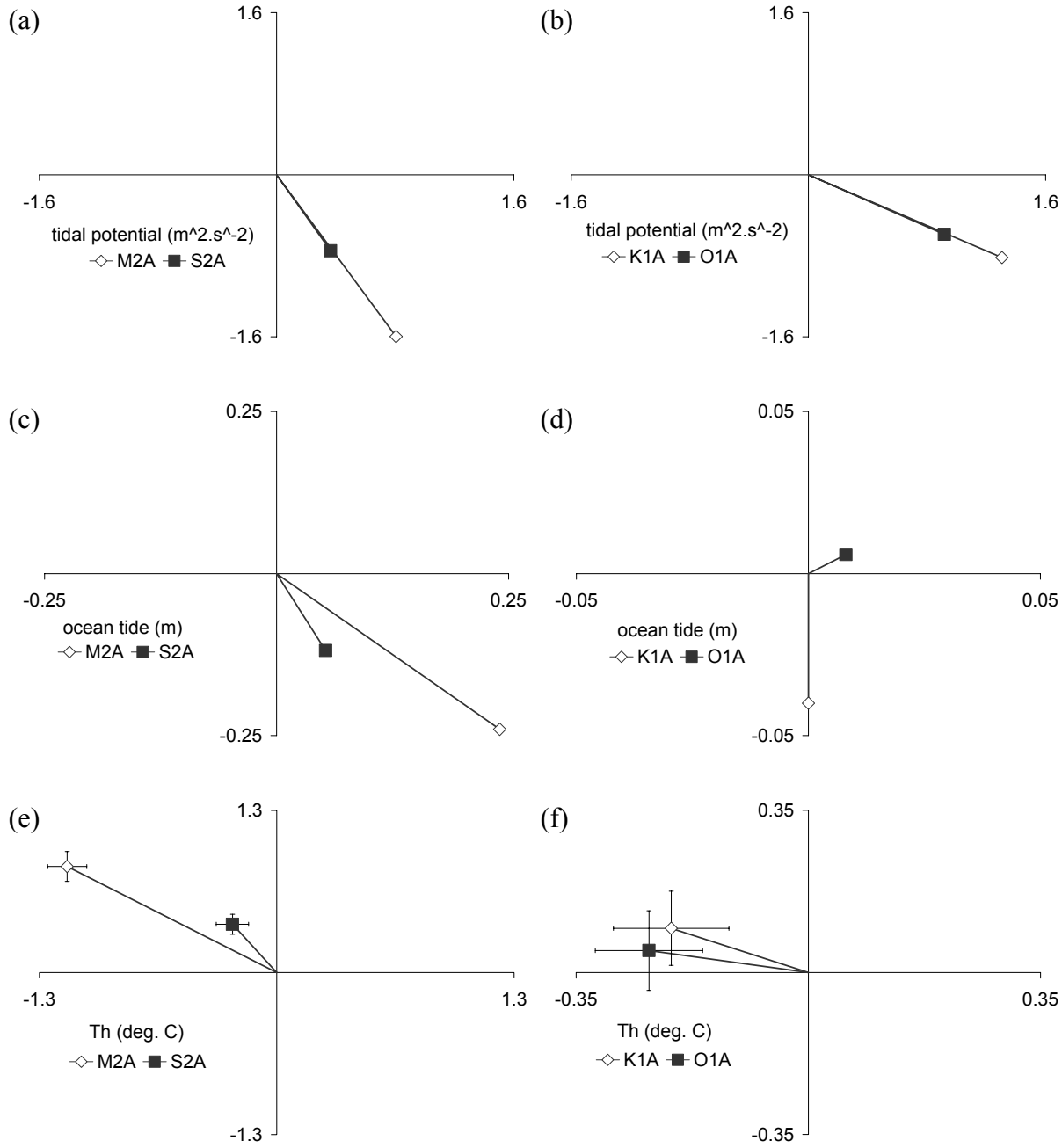

Figure 4.20: Admiralty Method harmonic constants for the Lucky Strike site (37.28°N, 32.33°W) calculated using the HYBRID code. Tidal potential from ETGTAB code, Ocean tide from CSR code, *Th* – ambient (thermistor) temperature measured by Medusa.

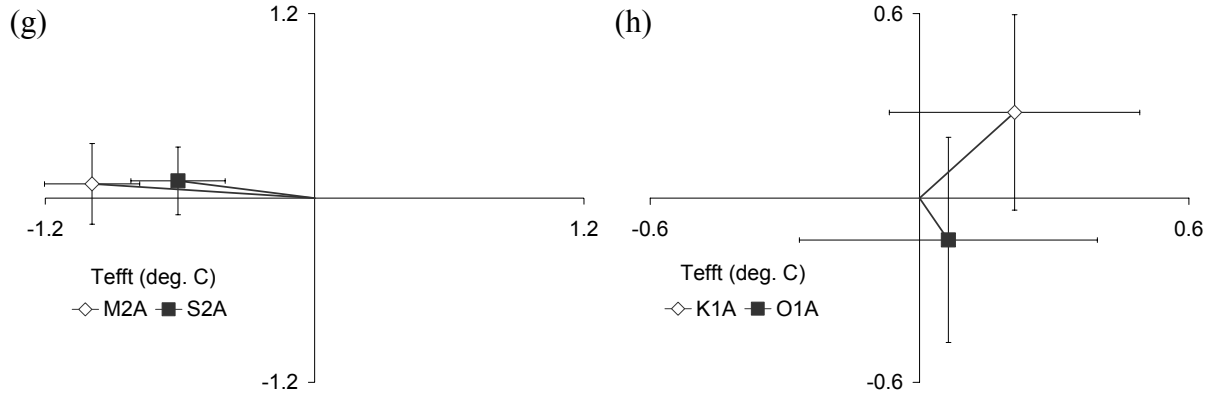

Figure 4.20: (continued) Admiralty Method harmonic constants for the Lucky Strike site (37.28°N, 32.33°W) estimated using the HYBRID code. *Tefft* – Medusa effluent temperature.

The ratio of magnitudes of the semi-diurnal components (H_1/H_2) is 3.13 for the *Th*-signal. This is roughly consistent with both the ocean tide (H_1/H_2=2.62) and the tidal potential (H_1/H_2=2.14).

Lucky Strike	H_1 (*M2A*)	g_1 (*M2A*)	H_2 (*S2A*)	g_2 (*S2A*)	H_3 (*K1A*)	g_3 (*K1A*)	H_4 (*O1A*)	g_4 (*O1A*)
potential ($m^2.s^{-2}$)	1.79	63°	0.835	64°	1.54	32°	1.09	33°
ocean (m)	0.34	45°	0.13	66°	0.04	90°	0.01	324°
Th (°C)	1.43	217°	0.46	238°	0.23	205°	0.24	191°
Tefft (°C)	1.00	185°	0.62	190°	0.35	307°	0.15	65°
ve ($mm.s^{-1}$)	60.6	329°	13.6	3°	3.2	261°	3.9	253°
vn ($mm.s^{-1}$)	74.5	279°	16.2	329°	3.2	213°	3.7	244°
T (°C)	0.096	230°	0.022	226°	0.0042	115°	0.0036	45°

Lucky Strike	$(H_1+H_2)/(H_3+H_4)$	H_1/H_2	g_2-g_1	H_3/H_4	g_4-g_3
potential ($m^2.s^{-2}$)	0.998	2.14	< 1°	1.41	< 1°
ocean (m)	9.4	2.62	21°	4.0	-126°
Th (°C)	3.99	3.13	21°	0.93	-13°
Tefft (°C)	3.23	1.61	5°	2.32	117°
ve ($mm.s^{-1}$)	10.6	4.47	34°	0.82	-8°
vn ($mm.s^{-1}$)	13.17	4.59	50°	0.86	31°
T (°C)	15.12	4.30	-4°	1.17	-71°

Table 4.8: Admiralty Method harmonic constants for the Lucky Strike site, calculated for the tidal potential, ocean tide, Medusa data and water column data.

In the diurnal band, the difference in phase lag of the harmonic constants, (g_4–g_3), is only 13° for the *Th*-signal, and the magnitudes of the diurnal components are approximately equal

($H_3/H_4 \approx 1$). Consequently, the diurnal harmonic constants of the *Th*-signal display more similarity with the tidal potential than with the ocean tide. However, the error bars associated with these estimates are considerable and the spectral estimate (Figure 4.19b) displays significantly more power in the semi-diurnal band than the diurnal. For this reason, it seems reasonable to give more weight to the evidence of the semi-diurnal harmonic constants. Following this line of reasoning, it is concluded that the *Th*-signal has a tidal part which is very similar to the ocean tide, but with the semi-diurnal components delayed by 172°.

A similar interpretation can be made of the harmonic constants of the *Tefft*-signal (Figure 4.20g,h). The diurnal components are poorly resolved (see the error bars in Figure 4.20h) and are not considered further. Within the semi-diurnal band, the difference in phase lag between *M2A* and *S2A*, (g_2-g_1), is 5°, which is closer to the value for the tidal potential (<1°) than to that for the ocean tide (21°). At first glance, this might seem to be evidence linking the effluent temperature more closely to the tidal potential than to the ocean tide. However, the size of the error bars in Figure 4.20g means that such an inference would be unwise. In common with the *Th*-signal, the semi-diurnal components of the *Tefft*-signal are approximately out of phase with the ocean tide. For the *M2A* component, the *Tefft*-signal lags the ocean tide by 140°. For the *S2A* component, the lag is 124°.

4.7.3.4 Water column measurements – time-domain

Current and temperature data collected in the water column at Lucky Strike are shown in the time-domain in Figure 4.21 (A. Vangriesheim, *pers. comm.*, 1998). These data were collected from sensors moored 20 m above the seafloor. Time-series for the eastwards (*ve*) and northwards (*vn*) velocity are shown, along with a time-series of the current speed (*spd*), defined by $spd^2 = ve^2 + vn^2$. The temperature time-series (*T*) was obtained at the same location. All of these series show clear evidence of tidal modulation in the time-domain (Figure 4.21).

The time-series are predominantly semi-diurnal (Figures 4.21b,d), and exhibit a springs/neaps cycle (Figures 4.21a,c). The *spd*-signal displays quarter-diurnal periodicity (Figure 4.21f; Section 2.6.3). Consequently, any physical process which depends on the magnitude of the tidal stream, but not on its direction, is expected to exhibit the same frequency-doubling effect.

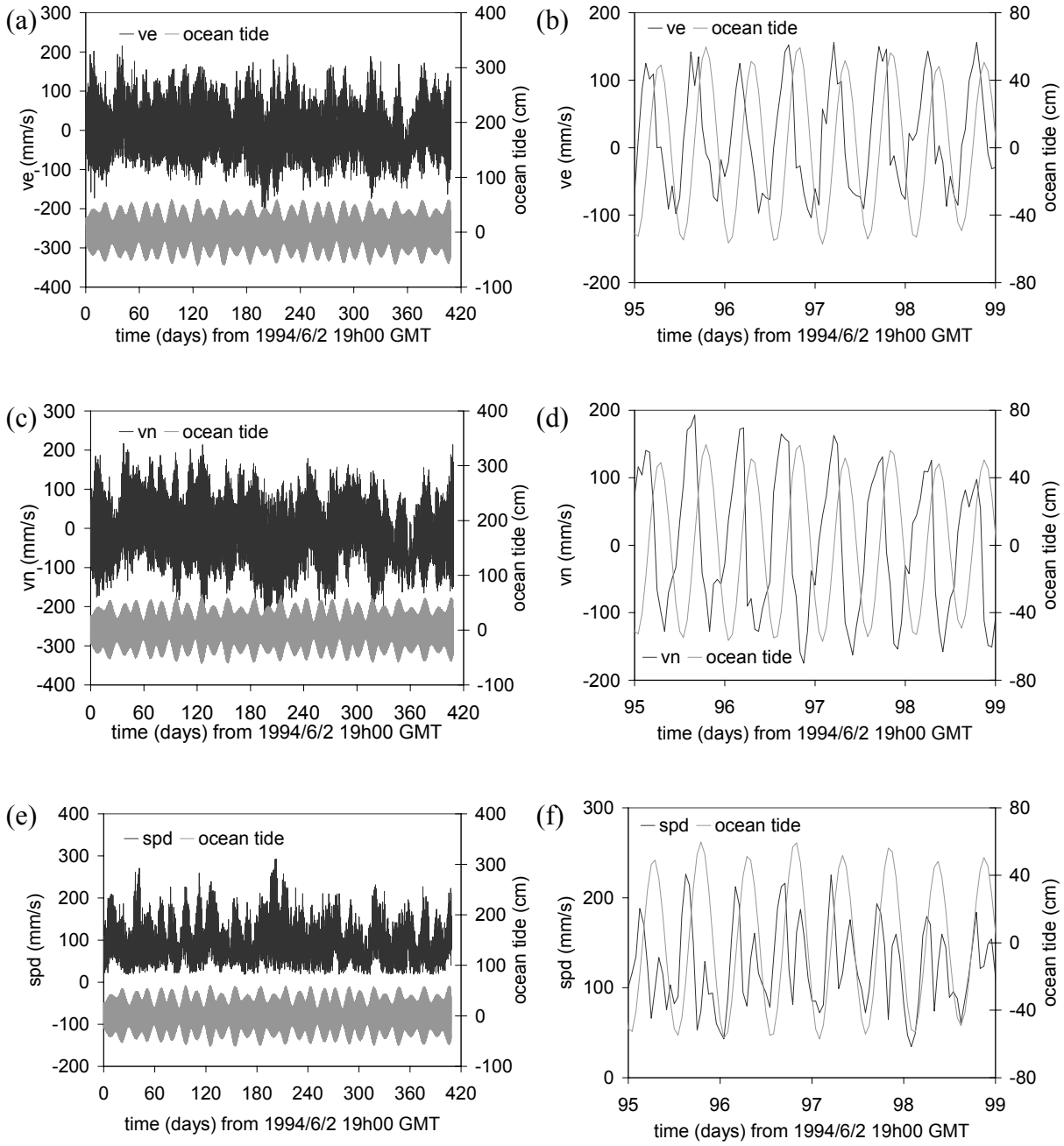

Figure 4.21: Current meter data collected at Lucky Strike (37.28°N, 32.33°W), from a sensor moored 20 m above the seafloor. *ve* – eastward velocity, *vn* – northward velocity, *spd* – speed. Data collected by A. Vangriesheim (*pers. comm.*, 1998).

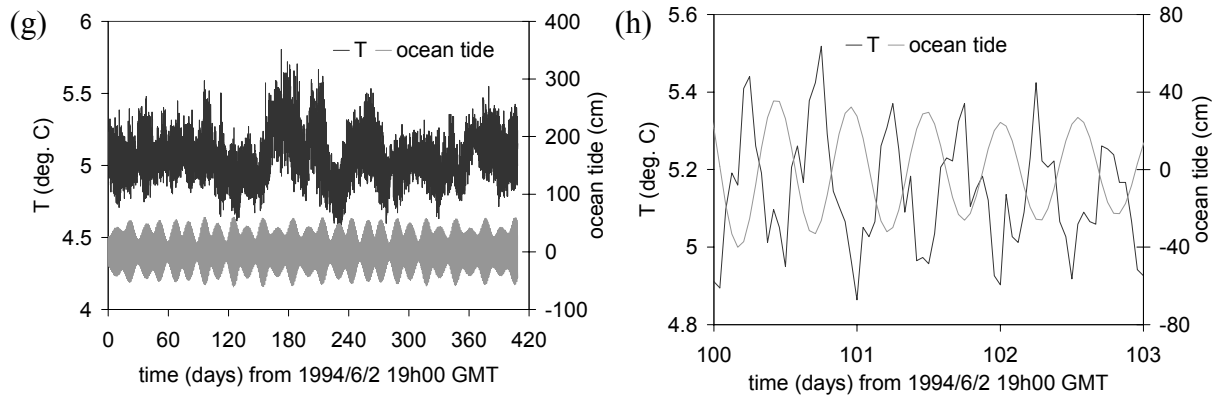

Figure 4.21: (continued) Temperature data (*T*) collected at Lucky Strike (37.28°N, 32.33°W), from a sensor moored 20 m above the seafloor. Data collected by A. Vangriesheim (*pers. comm.*, 1998).

The *T*-signal also displays semi-diurnal periodicity and a clear springs/neaps cycle (Figure 4.21g,h). From Figure 4.21g,h, the *T*-signal lags the ocean tide by ~180°.

4.7.3.5 Water column measurements – non-parametric analysis

Power spectra for the *ve*-, *vn*-, *spd*- and *T*- time-series were calculated using the MWPS code and are shown in Figure 4.22. The time-series cover 408 days and consist of N=9,808 datapoints at a sampling interval of Δt = 1 h. The power spectra were calculated using a time-bandwidth product of 10, using 20 eigenspectra and with a 24-point (=24 h) autoregressive prewhitening filter.

The estimated power spectra of the *ve*- and *vn*-signals both have a general trend of the form $\hat{S}(f) \sim f^{-1.3}$ (Figures 4.22a,c), and contain several significant line components at the low frequency end of the spectrum (Figure 4.22b,d; Tables 4.9, 4.10).

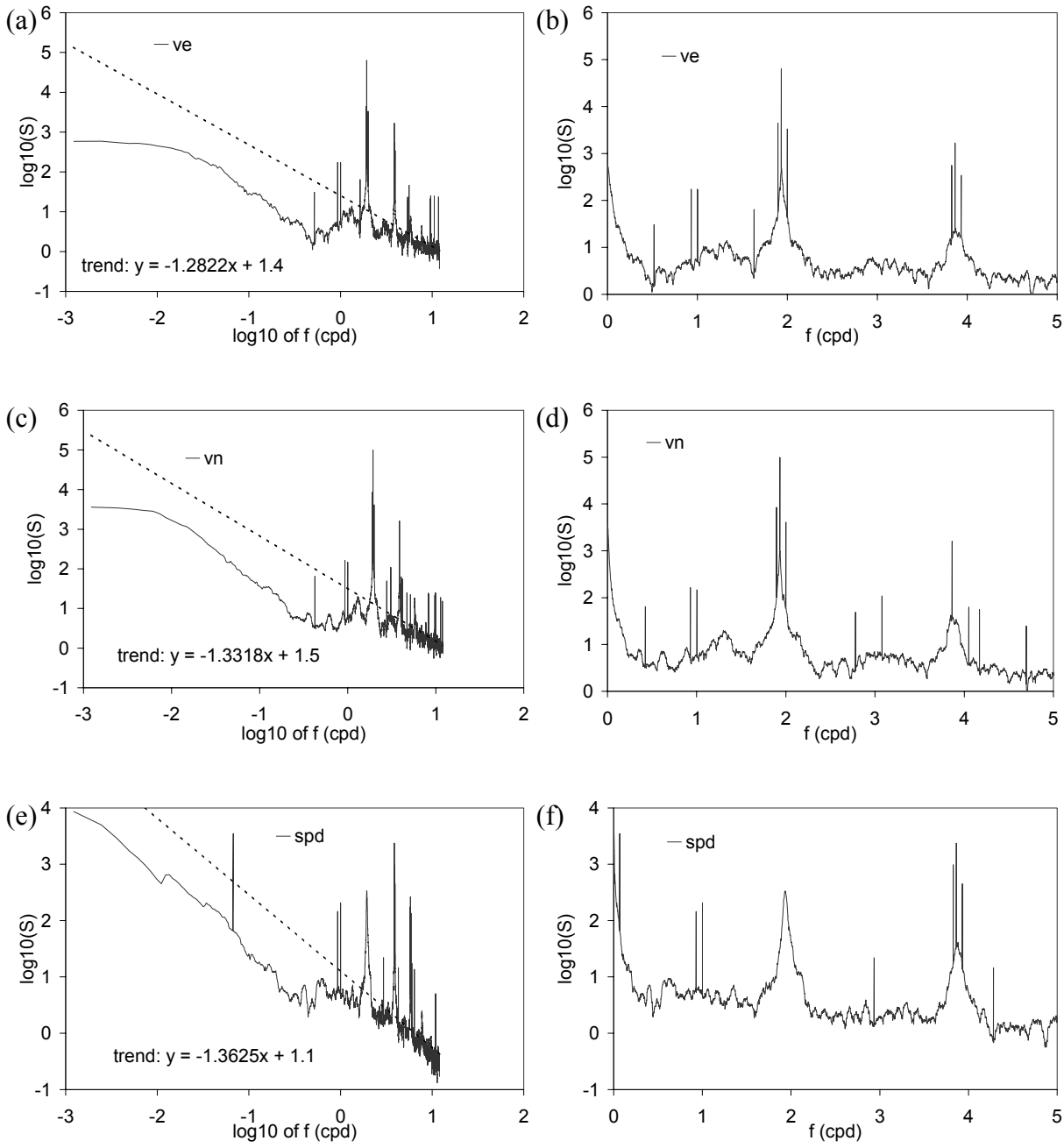

Figure 4.22: Spectral estimates for the water column data collected 20 m above the seafloor at Lucky Strike (37.28°N, 32.33°W) calculated using the MWPS code. *ve* – eastward velocity, *vn* – northward velocity, *spd* – speed. Data collected by A. Vangriesheim (*pers. comm.*, 1998).

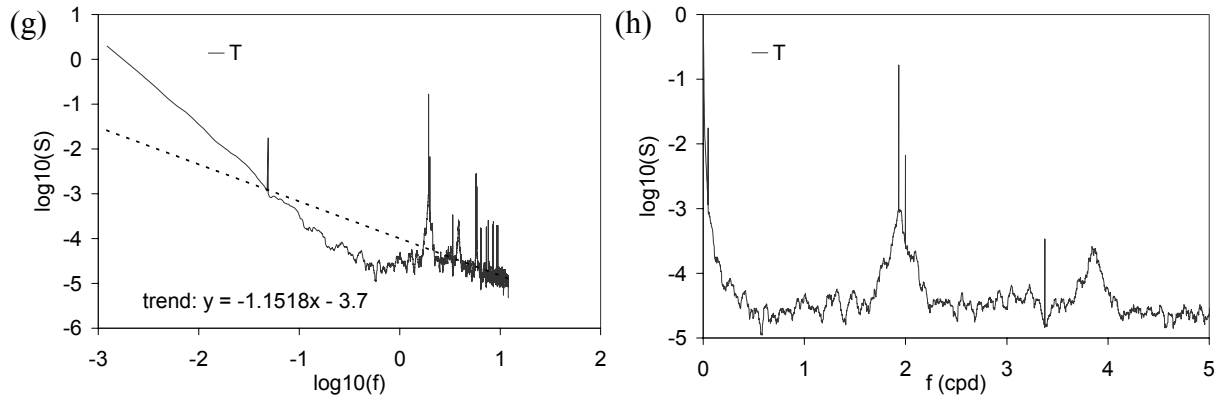

Figure 4.22: (continued) Spectral estimates for the water column data collected 20 m above the seafloor at Lucky Strike (37.28°N, 32.33°W) calculated using the MWPS code. *T* – temperature. Data collected by A. Vangriesheim (*pers. comm.*, 1998).

Most of the observed line components in the two velocity channels coincide with known tidal components. Therefore the estimated spectra constitute very strong evidence of tidal modulation of the velocity signals.

Low frequency line components – *ve* signal at Lucky Strike		
frequency of observed line (cpd)	frequency of associated tidal component (cpd)	name of associated tidal component
0.518 ± 0.001		
0.930 ± 0.001	0.930	*O1*
1.002 ± 0.001	1.003	*K1*
1.630 ± 0.001		
1.896 ± 0.001	1.896	*N2*
1.932 ± 0.001	1.932	*M2*
1.999 ± 0.001	2.000	*S2*
3.828 ± 0.001		
3.865 ± 0.001	3.865	2nd harmonic of *M2*
3.932 ± 0.001		

Table 4.9: Significant line components detected in the *ve*-signal (Figure 4.22b).

The estimated spectrum of the *spd*-signal is shown in Figures 4.22e,f, with the significant line components listed in Table 4.11. Of course, the *spd*-signal is derived from the *ve*- and *vn*-signals, so it is no surprise to find that its spectrum has power concentrated in the same frequency bands and their harmonics. The larger concentration of power in the quarter-diurnal band is caused by the frequency-doubling observed in the time-domain. It is

interesting to note that, despite this effect, the spectrum for the *spd*-signal retains two harmonic lines in the diurnal band (Table 4.11).

Low frequency line components – *vn* signal at Lucky Strike		
frequency of observed line (cpd)	frequency of associated tidal component (cpd)	name of associated tidal component
0.424 ± 0.001		
0.930 ± 0.001	0.930	*O1*
1.002 ± 0.001	1.003	*K1*
1.896 ± 0.001	1.896	*N2*
1.932 ± 0.001	1.932	*M2*
2.001 ± 0.001	2.000	*S2*
2.780 ± 0.001		
3.079 ± 0.001		
3.865 ± 0.001	3.865	2nd harmonic of *M2*
4.052 ± 0.001		
4.172 ± 0.001		
4.697 ± 0.001		

Table 4.10: Significant line components detected in the *vn*-signal (Figure 4.22d).

The estimated spectrum of the *T*-signal is shown in Figures 4.22g,h. It has a general trend of the form $\hat{S}(f) \sim f^{-1.2}$, which is broadly similar to the general trend of the velocity spectra. This is consistent with the hypothesis that temperature changes at this height (20 m above the seafloor) are caused by the lateral movement of hydrothermal plumes. The close-up view of the spectrum (Figure 4.22h) shows no evidence of significant power in the diurnal band, but there is a broad semi-diurnal peak and significant lines were found at the principal semi-diurnal frequencies (Table 4.12).

Low frequency line components – *spd* signal at Lucky Strike		
frequency of observed line (cpd)	frequency of associated tidal component (cpd)	name of associated tidal component
0.067 ± 0.001	0.068	*MSf*
0.930 ± 0.001	0.930	*O1*
1.002 ± 0.001	1.003	*K1*
2.935 ± 0.001		
3.828 ± 0.001		
3.864 ± 0.001	3.865	2nd harmonic of *M2*
3.931 ± 0.001		
4.282 ± 0.001		

Table 4.11: Significant line components detected in the *spd*-signal at Lucky Strike (Figure 4.22f).

Low frequency line components – *T*-signal		
frequency of observed line (cpd)	frequency of associated tidal component (cpd)	name of associated tidal component
0.049 ± 0.001		
1.932 ± 0.001	1.932	*M2*
1.999 ± 0.001	2.000	*S2*
3.377 ± 0.001		

Table 4.12: Significant line components detected in the *T*-signal (Figure 4.22h).

In conclusion, the estimated power spectra for the velocity and temperature data collected in the water column all present strong evidence of tidal modulation. The identification of so many statistically significant harmonic lines by the MWPS code is particularly compelling. The presence of strong quarter-diurnal periodicity in the *spd*-signal (Figure 4.21f) renders it unsuitable for an Admiralty Method analysis. However, the *ve*- *vn*- and *T*-signals appear to be relatively clean tidal signals in the time-domain, and are therefore subjected to an Admiralty Method analysis below.

4.7.3.6 Water column measurements – parametric analysis

Admiralty Method harmonic constants for the *ve*-, *vn*- and *T*-signals are estimated using the HYBRID code. They are listed in Table 4.8 and shown graphically in Figure 4.23, where they are compared with the equivalent harmonic constants for the local ocean tide.

The harmonic constants for the *ve*- and *vn*-signals were estimated using Huber-weighted section averaging with mean removal (Section 3.3.4) because Bayesian drift removal proved unsuccessful in these cases, for the reasons outlined in Section 4.5.1. The original time-series of N=9,808 points was split into 192 overlapping sections of 168 points (= 7 days), giving a 30% offset between sections.

The harmonic constants for the *ve*- and *vn*-signals show a marked similarity with those for the local ocean tide. The relative magnitude of semi-diurnal and diurnal components is similar for all three signals, with $(H_1+H_2)/(H_3+H_4)$=9.4 for the ocean tide, $(H_1+H_2)/(H_3+H_4)$=10.6 for the *ve*-signal and $(H_1+H_2)/(H_3+H_4)$=13.17 for the *vn*-signal (Table 4.8).

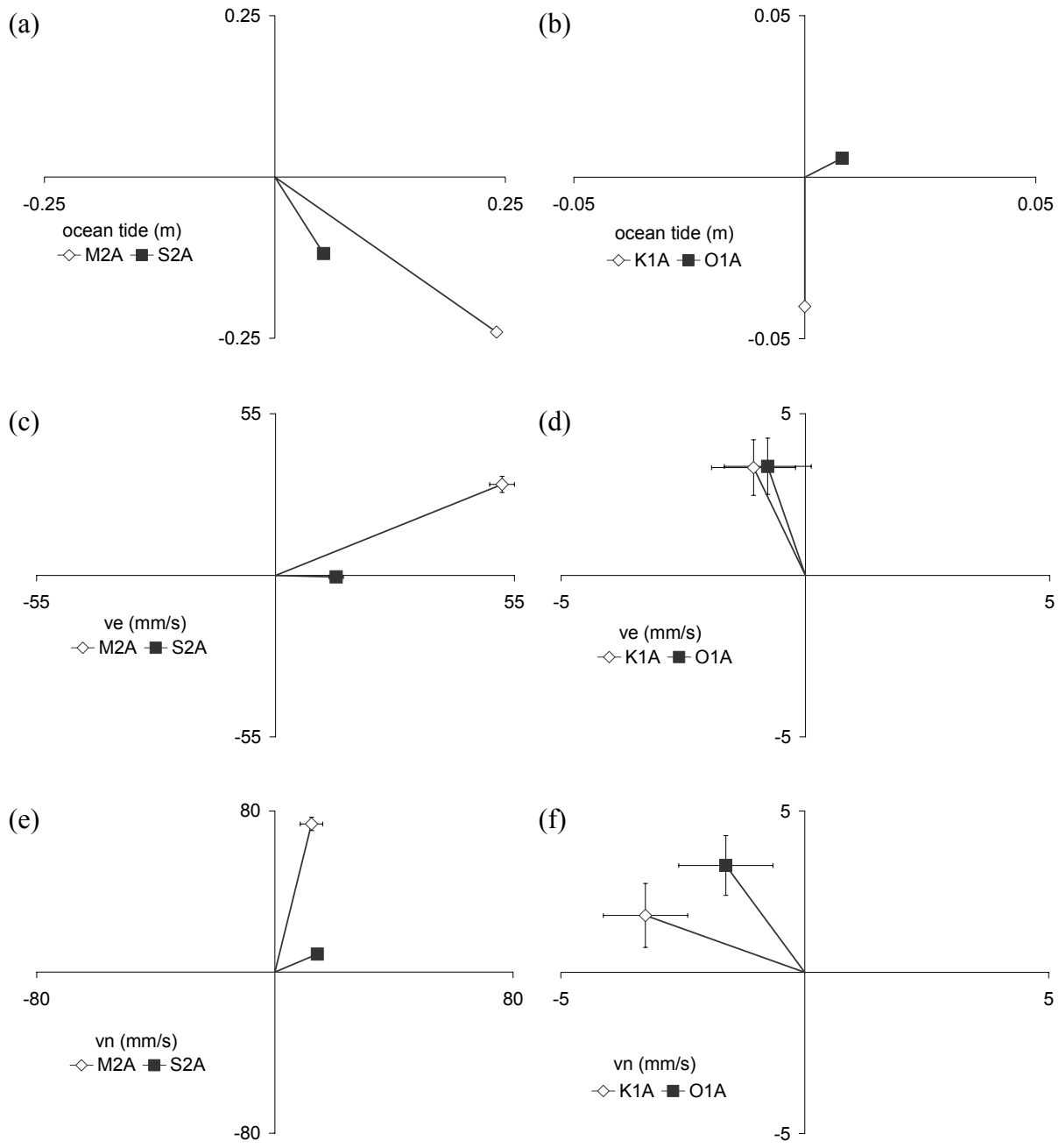

Figure 4.23: The Admiralty Method harmonic constants for the water column data collected at Lucky Strike (37.28°N, 32.33°W) calculated using the HYBRID code, compared with the harmonic constants for the local ocean tide. *ve* – eastward velocity. *vn* – northward velocity.

Furthermore, the relative magnitudes and phases of the semi-diurnal components (H_1/H_2 and (g_2–g_1)) are broadly similar for the three signals, so that the semi-diurnal harmonic constants of the *ve*- and *vn*-signals appear to be rotated versions of their ocean tide equivalents in the complex plane (Figures. 4.23a,c,e).

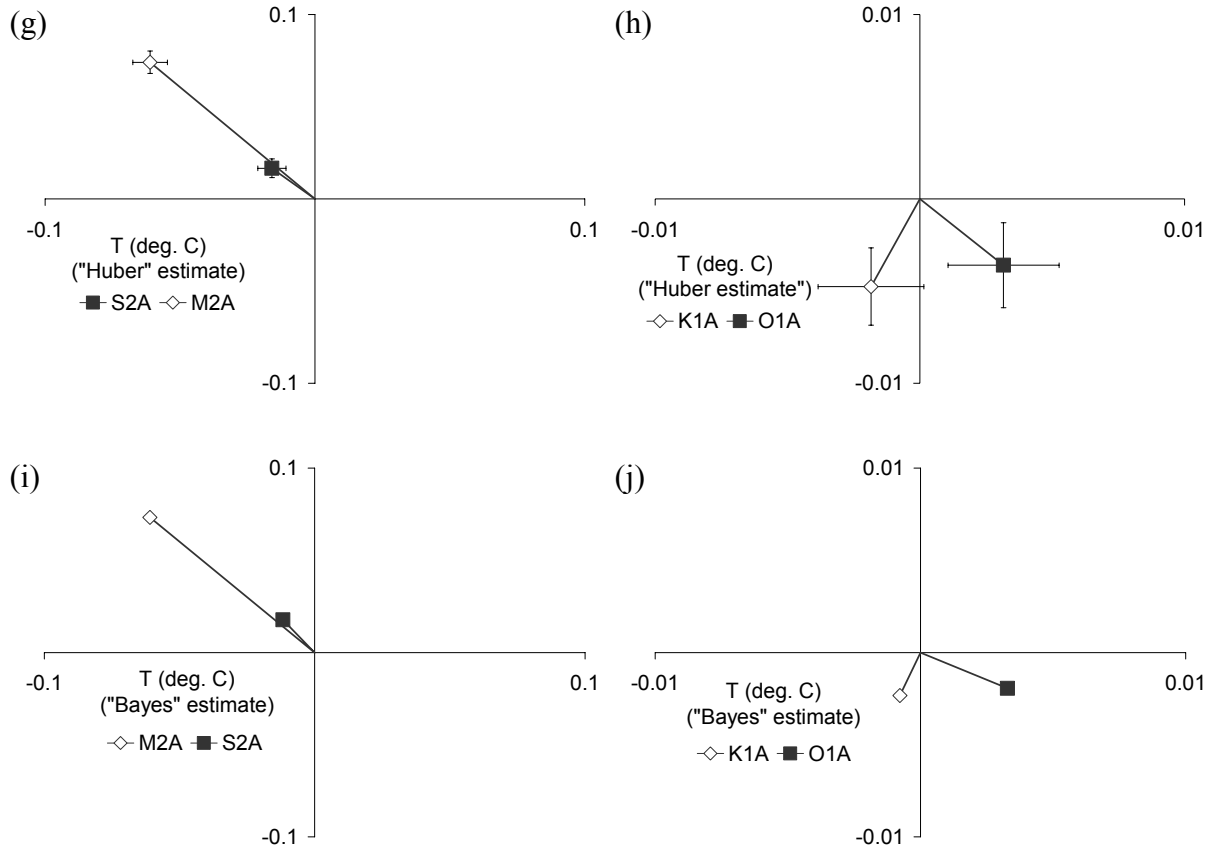

Figure 4.23: (continued) The Admiralty Method harmonic constants estimated for the *T*-signal collected at Lucky Strike (37.28°N, 32.33°W) using the HYBRID code. The "Huber" estimate was made using section averaging with mean removal. The "Bayes" estimate was made using Bayesian drift removal (Section 3.3.4).

This similarity of harmonic constants is not surprising – indeed, it is to be expected from the simple theory of tidal streams presented in Chapter 2 – but it is, nonetheless, worth noting. It increases confidence that the semi-diurnal harmonic constants provide an accurate parametric description of the velocity time-series.

The diurnal harmonic constants of the velocity signals, on the other hand, do not display a similar phase relationship to those of the ocean tide (Figures 4.23b,d,f). They are also much smaller in magnitude than the semi-diurnal harmonic constants. For these reasons, the diurnal harmonic constants are poorly constrained, and no attempt is made to draw inferences from them.

Two sets of harmonic constants for the *T*-signal were estimated using the HYBRID code. The first set (Figures 4.23g,h) was calculated using the same Huber-weighted section averaging technique which is applied to the *ve*- and *vn*-signals above. The second set (Figures 4.23i,j) was calculated using Bayesian drift removal. There is a striking similarity between the two sets of harmonic constants. The *T*-signal is therefore unique, among the datasets considered here, in yielding a credible set of harmonic constants under analysis by the HYBRID code using the Bayesian drift removal procedure. The results of this analysis are shown in the time-domain in Figure 4.24.

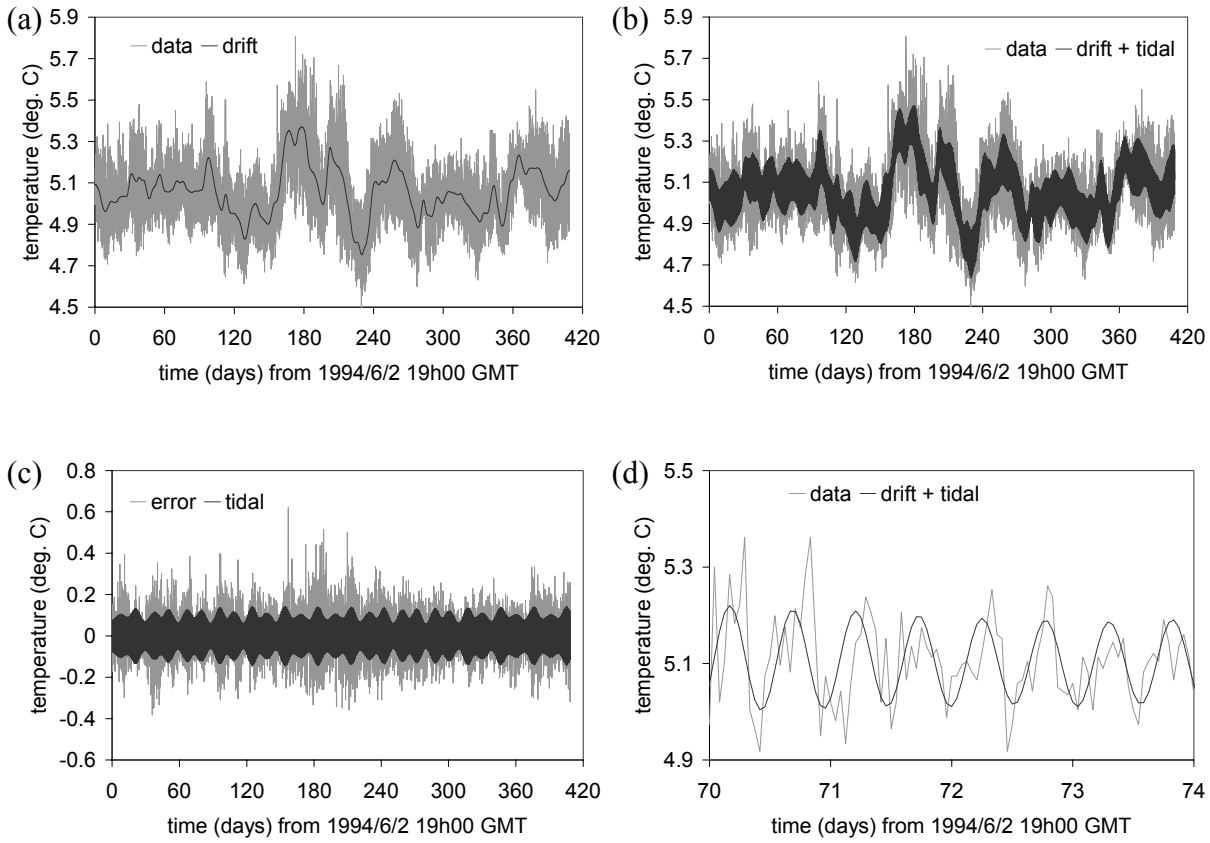

Figure 4.24: The results of the extraction of Admiralty Method harmonic constants from the water column *T*-signal at Lucky Strike (37.28°N, 32.33°W), using the HYBRID code with the Bayesian drift removal technique of Section 3.3.3.

The Bayesian drift removal algorithm of the HYBRID code is designed to decompose the original time-series (*data*) into a sum of three separate time-series (*drift*, *tidal* and *error*). The set of Admiralty Method harmonic constants which generate the *tidal* signal constitute a parametric estimate of the tidal information in the original data (Section 3.3.3). There is a

considerable amount of drift in the *T*-signal, but it has been successfully identified by the algorithm (Figure 4.24a). Figures 4.24b and 4.24d show that the sum of the *drift* and *tidal* signals corresponds well with the original data. For example, the springs/neaps cycle has been reproduced quite well. Since the springs/neaps cycle is caused by the beating of the *M2* and *S2* components, this constitutes evidence that the estimated phases for the *M2A* and *S2A* components are reliable.

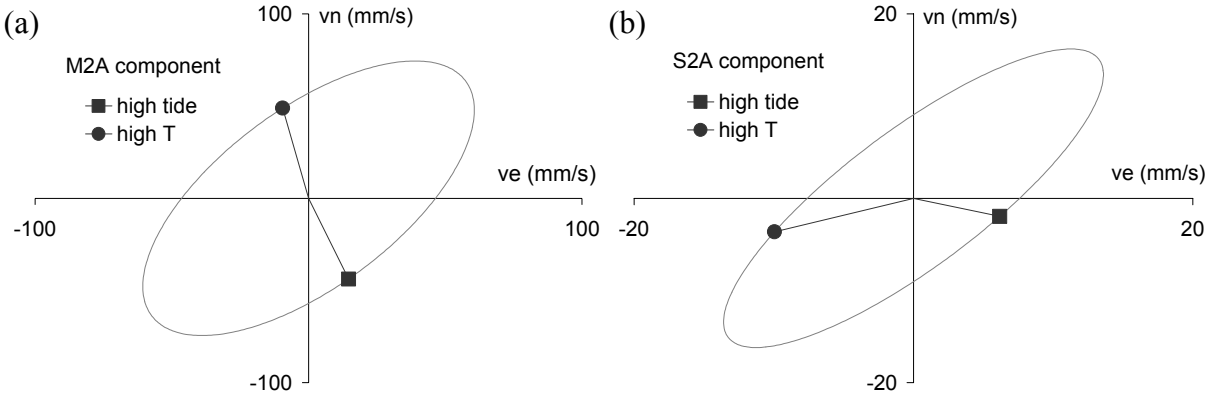

Figure 4.25: Tidal current ellipses extracted from the water column data collected at Lucky Strike (37.28°N, 32.33°W). The Admiralty Method harmonic constants of Table 4.8 were used to generate the ellipses. Also shown on each diagram are the current vector at the time of highest ocean tide ('high tide'), and the current vector at the time of highest measured temperature ('high T').

The phase relationship between velocity (*ve*, *vn*), ocean tide (ζ) and temperature (*T*) can now be examined, making use of the harmonic constants estimated for each series. Firstly, consider the *M2A* component of each time-series. Let *t* be the time (in hours) since the Greenwich passage of the *M2A* component of the tidal potential. Let ω be the angular speed of the *M2A* component (in degrees per hour). The *M2A* components of the four time-series can now be expressed as functions of time, using the harmonic constants of Table 4.6:

$$\left\{\begin{array}{l} ve_{M2A}(t) = 60.6\cos(\omega t - 329) \\ vn_{M2A}(t) = 74.5\cos(\omega t - 279) \\ T_{M2A}(t) = 0.096\cos(\omega t - 230) \\ \zeta_{M2A}(t) = 0.34\cos(\omega t - 45) \end{array}\right\} \tag{4.11}$$

In a horizontal plane where *x* points east and *y* points north, the velocity vector is ($ve(t)$,$vn(t)$), at time *t*. As *t* varies over the course of a tidal cycle, this vector traces a curve in

the *x-y* plane known as the current ellipse. The *M2A* current ellipse for the Lucky Strike velocity data is shown in Figure 4.25a. Hence T_{M2A} is maximised when $\omega t = 230°$, and ζ_{M2A} is maximised when $\omega t = 45°$. The current vectors corresponding to these times are shown in Figure 4.25a. This figure shows that, for the *M2A* component, the current flows slightly west of due north at the time of maximum temperature, and slightly east of due south at the time of high tide. The sensor was moored 400 m due north of the Statue of Liberty hydrothermal vent (A. Vangriesheim, *pers. comm.*, 1998), so it is possible that the tidal temperature variations are due to advection of a plume northwards from the vent site. Figure 4.25b shows the tidal ellipse for the *S2A* component. For this component, the time of highest temperature corresponds to an approximately westward current, which seems inconsistent with the *M2A* result. However, the *S2A* component is much smaller in magnitude and is probably less well constrained.

In summary, the water column data discussed above demonstrate the utility of the Bayesian drift removal technique for sufficiently 'clean' tidal signals. Well constrained Admiralty Method harmonic constants for the tidal streams are extracted for the tidal streams by the HYBRID code. Consequently, the tidal streams at Lucky Strike can be estimated in the time-domain for any date. The harmonic constants are consistent with a model in which the modulation of water column temperature is caused by advection of a plume from the Statue of Liberty hydrothermal vent.

4.8 Other hydrothermal sites

Kadko (1994) reports that a gamma-ray detector placed in diffuse (25°C) flow at the Monolith Vent of the Juan de Fuca Ridge (44.9800°N, 130.2217°W) recorded tidal variations in total radioactivity over a 4 day observation period. It is suggested that these variations are caused by tidally modulated changes in the radon content of the water. No phase relationship with the local ocean tide is given, but it is reported that the oscillations in total radioactivity lag the effluent temperature by ~270° (Kadko, 1994). The simple poroelastic model of Chapter 6 suggests that the effluent temperature at the seafloor lags the ocean tide by a phase angle in the range [135°, 225°]. Under this model, therefore, Kadko's (1994) data imply that the total radioactivity of the effluent lags the ocean tide by a phase angle in the range [45°, 135°]. In comparison, the theory of Chapter 6 predicts that the effluent velocity lags the ocean tide by a phase angle in the range [90°, 135°]. Therefore a new mechanism for the tidal modulation of total radioactivity is proposed here. It may be

that the variations in total radioactivity are not caused by a change in the concentration of radon, but by tidal modulation of the effluent velocity.

Chevaldonné *et al.,* (1991) report time-series measurements made with THYDRO temperature probes. These probes can be inserted a few centimetres into hydrothermal edifices or placed inside clusters of living animals at vent sites. Temperature time-series collected at three separate sites all showed evidence of tidal modulation. The measurements were made at the Totem hydrothermal vent field on the East Pacific Rise (12°49'N, 103°57'W), the Hine Hina vent field in the Lau back-arc basin (22°32'S, 176°43'W), and the White Lady vent field in the North Fiji Basin (16°59'S, 173°55'W). Unfortunately it is not possible to compare the published temperature time-series with predictions of the local ocean tide because the exact start times for the datasets are not published. It is therefore requested that all future reported time-series measurements include the exact location and start time of the dataset to facilitate comparison with the ocean tide.

McDuff & Delaney (1995) and Delaney *et al.* (1997a) report tidal modulation of the temperature of a high temperature vent in the Main Endeavour Field of the Juan de Fuca Ridge. This vent is named "Puffer" because of its periodic step-wise jumps in temperature. These temperature excursions are separated by ~12.5 hours and Delaney *et al.* (1997a) suggest that the phenomenon is due to tidal modulation of subseafloor phase separation.

Most recently, Johnson *et al.* (2000) report tidal modulations in temperature measurements made using thermistors inserted into beds of vestimentiferan tube-worms around diffuse hydrothermal vents. These measurements were made in the Main Endeavour Field of the Juan de Fuca Ridge.

4.9 Conclusions

Evidence of tidal modulation at seafloor hydrothermal systems is provided by a wide variety of time-series collected above, below and on the seafloor. Tidal modulation has been observed in time-series of (1) subseafloor pressure, (2) subseafloor temperature, (3) water column temperature, (4) effluent temperature, (5) effluent velocity (6) effluent composition and (7) the frequency of occurrence of hydrothermal upwelling events. Where possible, the procedure developed in Chapters 2 and 3 is used to re-examine previously published data.

This theory is also used to analyse time-series acquired by the Medusa hydrothermal effluent monitoring system - some of which are presented here for the first time.

The suggested procedure for the analysis of hydrothermal time-series is reiterated below, along with general remarks motivated by the data reported in this chapter.

Firstly, the 'output' data time-series should be viewed in the time-domain alongside the 'input' time-series which is expected to cause tidal modulation which in most cases is the local ocean tide or tidal streams. Ideally the 'input' ocean tide signal would be measured on the seafloor concurrently with the 'output' data time-series. If this is not possible, the ocean tide can be estimated using public domain computer codes such as CSR. It is requested that researchers publish the *exact* time at which their time-series begin to facilitate estimation of the ocean tide. Seafloor hydrothermal systems occur over a wide range of longitudes (i.e. time-zones) and so it is suggested that all future time-series be plotted with Greenwich Mean Time (GMT) as the time ordinate. Furthermore, if a tidally modulated time-series is plotted on an arbitrary timescale which does not record the date, a great deal of valuable information is denied to the analyst. This lost information consists of the positions of the sun and moon during the time-series. These positions are easily predicted from well known astronomical formulae, *provided the date is known*, and are expected to produce a similar non-stationarity in *all* tidal signals. Therefore, knowledge of the date allows any amplitude-modulation or frequency-modulation observed in the data to be compared with astronomical theory.

Secondly, a non-parametric estimate of the power spectrum of the data time-series should be made using the multiple window method (Thomson, 1982). This algorithm identifies statistically significant line components in the spectrum which can be compared with the well known discrete set of tidal frequencies (Table 2.1). If significant line components are identified at several tidal frequencies, it can be concluded with confidence that the time-series is tidally modulated. The multiple window algorithm can produce very different spectral estimates to the simple periodogram estimates which have often been used (e.g. Figure 4.3). The time-bandwidth product ($NW\Delta t$) chosen for a multiple window analysis can be chosen according to the components of the tide which it is hoped to identify. For example, to identify separate line components at frequencies f_1 and f_2 requires that $W < |f_1 - f_2|$. Following Wetzler *et al.* (1998) it is suggested that the overall slope of an estimated spectrum be examined on a log-log plot. An estimated spectrum which takes the form $\hat{S}(f) \sim f^{-5/3}$ at high frequencies is consistent with the turbulence model of the Kolmogorov hypothesis (Section 4.2.5).

Thirdly, a parametric estimate of the tidal part of the time-series should be made using the Admiralty Method. The estimated harmonic constants can be compared with those of the ocean tide and the tidal potential in the complex plane to establish if there is a correlation between the output data signal and either of these two postulated input signals. The results presented here suggest that the tidal modulations observed at seafloor hydrothermal systems are more closely correlated to the local ocean tide than to the local tidal potential. This provides evidence that the tidal modulation of hydrothermal systems due to the load tide is more significant than the tidal modulation due to the solid tide. This observation is consistent with calculations showing that crustal strains due to the load tide are probably about 2 orders of magnitude greater than those due to the solid tide (Section 2.5.4). Consequently, it is concluded that the solid tide has negligible influence on seafloor hydrothermal systems relative to the ocean tide. Consequently, it is only the effect of ocean tide loading which is considered in Chapter 6.

It is demonstrated in Sections 4.2.2 and 4.3.1 that the ocean tide at a seafloor hydrothermal site can differ significantly from the ocean tide at the nearest coastal port. Consequently coastal values of the ocean tide should *not* be considered representative of the tide in the open oceans. It is strongly recommended that global ocean tide models (such as the CSR code) be used whenever it is necessary to infer the ocean tide at a hydrothermal system. Furthermore, it is an oversimplification to assume that the tidal streams on the seafloor are given by the time derivative of the ocean tide. It is shown in Section 4.2.2 that use of the theory of tidal streams (Section 2.6) leads to predicted tidal streams which differ in both magnitude and phase from those obtained by taking the time-derivative of the ocean tide. Ideally, current meter data should be collected concurrently with time-series measurements of hydrothermal systems. In the absence of such direct data, however, great care should be exercised when estimating tidal streams from the ocean tide.

It is postulated that tidal signals in effluent velocity and temperature at seafloor hydrothermal systems are caused by tidal loading of the oceanic crust. Consequently, the phase lag of observed tidal modulations relative to the local ocean tide should be noted. This phase lag can be estimated approximately from examination of the data in the time-domain. In cases where reliable estimates of the Admiralty Method harmonic constants can be found, the phase lags should be estimated from comparison of the harmonic constants. For the data

discussed here, it is generally only possible to make a reliable estimate for the phase of the principal *M2A* component.

Phase lags of data time-series behind local ocean tide (*M2A* component)			
Location	Instrument	Data time-series	Phase lag behind ocean tide (*M2A* component)
ODP Hole 858G	thermistor string	borehole temperature	~180°
RM24	Medusa	ambient bottom water temperature	325°
Mariana Trough	OBSH	episodic venting activity	~0°
TAG	OBSH	episodic venting activity	90° to 180°
TAG	video camera	'shrimp density'	279°
TAG	Medusa	ambient bottom water temperature	267°
TAG	Medusa	effluent temperature	225°
TAG	geothermal probe	sub-bottom temperature	~90°
Menez Gwen	Medusa	ambient bottom water temperature	~90°
Lucky Strike	Medusa	ambient bottom water temperature	172°
Lucky Strike	Medusa	effluent temperature	140°

Table 4.13: The phase lags of observed time-series behind the local ocean for the *M2A* component.

Table 4.13 shows the phase lags of the *M2A* components of seafloor hydrothermal time-series behind the *M2A* component of the local ocean tide. It is predicted in Chapter 6 that effluent temperatures at the seafloor lag the ocean tide by a phase angle in the range [135°, 225°] depending on the assumed thickness and permeability of the seafloor. Table 4.13 shows that this prediction is consistent with the effluent temperatures measured by Medusa at TAG and Lucky Strike. Furthermore, it is diagnostic that the phase lag of effluent temperature behind the ocean tide at TAG lies at the lower end of the predicted range while the corresponding phase lag for Lucky Strike is at the upper end of the predicted range. It is shown in Chapter 6 that the TAG data are consistent with a model of a thin highly permeable

layer just below the seafloor. In contrast, the Lucky Strike data are consistent with a thick, low permeability layer.